

APPROVAL SHEET

Title of Dissertation: Material Optimization of Multi-Layer Enhanced Nanostructures

Name of Candidate: Pietro Strobbia
Doctor of Philosophy, 2016

Dissertation and Abstract Approved:



Dr. Brian M. Cullum
Associate Professor
Department of Chemistry and Biochemistry

Date Approved: 08/22/2016

ABSTRACT

Title of Document: MATERIAL OPTIMIZATION OF MULTI-LAYER ENHANCED NANOSTRUCTURES

Pietro Strobbia, PhD, 2016

Directed By: Dr. Brian M. Cullum, Associate Professor,
Department of Chemistry and Biochemistry

The employment of surface enhanced Raman scattering (SERS)-based sensing in real-world scenarios will offer numerous advantages over current optical sensors. Examples of these advantages are the intrinsic and simultaneous detection of multiple analytes, among many others. To achieve such a goal, SERS substrates with throughput and reproducibility comparable to commonly used fluorescence sensors have to be developed.

To this end, our lab has discovered a multi-layer geometry, based on alternating films of a metal and a dielectric, that amplifies the SERS signal (multi-layer enhancement). The advantage of these multi-layered structures is to amplify the SERS signal exploiting layer-to-layer interactions in the volume of the structures, rather than on its surface. This strategy permits an amplification of the signal without modifying the surface characteristics of a substrate, and therefore conserving its reproducibility. Multi-layered structures can therefore be used to amplify the sensitivity and throughput of potentially any previously developed SERS sensor.

In this thesis, these multi-layered structures were optimized and applied to different SERS substrates. The role of the dielectric spacer layer in the multi-layer enhancement was elucidated by fabricating spacers with different characteristics and studying their effect on the overall enhancement. Thickness, surface coverage and physical properties of the spacer were studied. Additionally, the multi-layered structures were applied to commercial SERS substrates and to isolated SERS probes.

Studies on the dependence of the multi-layer enhancement on the thickness of the spacer demonstrated that the enhancement increases as a function of surface coverage at sub-monolayer thicknesses, due to the increasing multi-layer nature of the substrates. For fully coalescent spacers the enhancement decreases as a function of thickness, due to the loss of interaction between proximal metallic films. The influence of the physical properties of the spacer on the multi-layer enhancement were also studied. The trends in Schottky barrier height, interfacial potential and dielectric constant were isolated by using different materials as spacers (i.e., TiO_2 , HfO_2 , Ag_2O and Al_2O_3). The results show that the bulk dielectric constant of the material can be used to predict the relative magnitude of the multi-layer enhancement, with low dielectric constant materials performing more efficiently as spacers. Optimal spacer layers were found to be ultrathin coalescent films (ideally a monolayer) of low dielectric constant materials.

Finally, multi-layered structures were observed to be employable to amplify SERS in drastically different substrate geometries. The multi-layered structures were applied to disposable commercial SERS substrates (i.e., Klarite). This project involved the

regeneration of the used substrates, by stripping and redepositing the gold coating layer, and their amplification, by using the multi-layer geometry. The latter was observed to amplify the sensitivity of the substrates. Additionally, the multi-layered structures were applied to probes dispersed in solution. Such probes were observed to yield stronger SERS signal when optically trapped and to reduce the background signal. The application of the multi-layered structures on trapped probes, not only further amplified the SERS signal, but also increased the maximum number of applicable layers for the structures.

MATERIAL OPTIMIZATION OF MULTI-LAYER ENHANCED
NANOSTRUCTURES

By

Pietro Strobbia

Dissertation submitted to the Faculty of the Graduate School of the
University of Maryland, Baltimore County, in partial fulfillment
of the requirements for the degree of
Doctor of Philosophy in Chemistry
2016

© Copyright by
Pietro Strobbia
2016

Acknowledgements

I am incredibly grateful for all the support I have received to accomplish this important step of my life from colleagues and family. First, I would like to thank Dr. Brian M. Cullum, my PhD adviser, for teaching me how to be a researcher and inspiring me to become a scientist. I will always remember our long discussion starting from lab contingencies and ending philosophizing about the true meaning of Science.

My time spent doing research in Cullum's lab was enriched by the presence of exceptional lab mates and friends. Sudhir, thank you for teaching me from your experience and how to deal with my initial cultural shock. Eric, thank you for sharing with me almost every moment of the growth throughout this PhD program. I would also like to thank Adam, Curtis, Joanna and Charles. If I was able to accomplish anything in the lab, I owe it to you all.

I would also like to thank my committee members, Dr. Arnold, Dr. Daniel, Dr. Gougousi and Dr. White for helping me define my project and for the positive discussions that help me define myself. In particular, Dr Gougousi and her students, Alex and Jaron, had a big contribution in my research. Dr. Gougousi thought me surface science my second year at UMBC, a class that was very useful for my project. In Gougousi's lab I was able to use the profilometer to calibrate metallic thicknesses and Alex and Jaron performed the atomic layer depositions for my substrates.

To the chemistry graduate students and the chemistry department staff, thanks for always being supportive and my friends. A special thanks goes to Florika for pushing and helping me to publish and accomplish my goals.

Obtaining a PhD is an achievement that apparently takes place between the laboratory walls. However, it was only possible for me thanks to the support that I have received from outside the department. I have to thank my wife, Kristine, for dealing with a perpetual student, for supporting my choices and for helping me achieving my goal. Also, I would not be at this point without the stimuli that meeting her has given me. A thank also goes to my family for sending me to study on the other side of the ocean and supporting me in my choices even if they were hard to understand at times.

Thank you all.

Table of Contents

ACKNOWLEDGEMENTS.....	II
TABLE OF CONTENTS.....	IV
LIST OF TABLES.....	VI
LIST OF FIGURES	VII
CHAPTER 1:	1
FROM UNDERSTANDING PLASMONICS TO DESIGNING STRUCTURES FOR SURFACE ENHANCED RAMAN SPECTROSCOPY	
1.1 <i>Background and Significance</i>	1
1.2 <i>Raman Spectroscopy</i>	4
1.3 <i>SERS</i>	11
1.5 <i>Multi-layered Structures</i>	32
CHAPTER 2:	40
LAYERED GOLD AND TITANIUM DIOXIDE SUBSTRATES FOR IMPROVED SURFACE ENHANCED RAMAN SPECTROSCOPIC SENSING	
2.1 <i>Introduction</i>	40
2.2 <i>Experimental</i>	43
2.3 <i>Results and Discussion</i>	48
2.4 <i>Conclusions</i>	64
CHAPTER 3:	67
DIELECTRIC SPACER DEPENDENCE OF MULTI-LAYERED STRUCTURES FOR ENHANCED SERS SENSING	
3.1 <i>Introduction</i>	67
3.2 <i>Experimental</i>	70
3.3 <i>Results and Discussion</i>	74
3.4 <i>Conclusions</i>	85
CHAPTER 4:	89
REGENERATION AND MULTI-LAYER AMPLIFICATION OF SENSING CHARACTERISTICS IN COMMERCIAL SUBSTRATES FOR SERS	
4.1 <i>Introduction</i>	89
4.2 <i>Experimental</i>	91
4.3 <i>Results and Discussion</i>	94
4.4 <i>Conclusions</i>	104
CHAPTER 5:	107
IMPROVING SENSITIVITY AND REPRODUCIBILITY OF SERS SENSING IN MICRO- ENVIRONMENTS USING INDIVIDUAL, OPTICALLY TRAPPED SERS PROBES	
5.1 <i>Introduction</i>	107
5.2 <i>Experimental</i>	110
5.3 <i>Results and Discussion</i>	114
5.4 <i>Conclusions</i>	126

CHAPTER 6:	130
CONCLUSIONS AND FUTURE PERSPECTIVES	
6.1 <i>Conclusions</i>	130
6.2 <i>Future Perspectives</i>	133
APPENDIX A:	136
IGOR PRO MACROS	
<i>Macro A1</i>	136
<i>Macro A2</i>	138
<i>Macro A3</i>	140
BIBLIOGRAPHY:	142

List of Tables

Table 4.1 Figures of merit of regenerated Klarite substrates.....	103
--	-----

List of Figures

Figure 1.1	Jablonski diagram of Raman scattering.....	8
Figure 1.2	Scheme backscattered Raman optical setup.....	9
Figure 1.3	Tuning ranges for different plasmonic materials.....	12
Figure 1.4a	Shape dependent tuning of surface plasmon resonance.....	14
Figure 1.4b	Thickness dependent tuning of surface plasmon resonance.....	14
Figure 1.5	Representation of SERS enhancement mechanism.....	16
Figure 1.6	SERS enhancements of different plasmonic materials.....	18
Figure 1.7	Representation of various recent nanostructures for SERS.....	25
Figure 1.8	Spectra of benzoic acid on a single layer and multi-layered substrate.....	33
Figure 2.1	Micrographs of metallic film over nanospheres.....	45
Figure 2.2	Scheme of the optical setup used for the Raman measurements.....	47
Figure 2.3	Scheme of the setup used for the reflectance measurements.....	47
Figure 2.4	SERS spectrum of mercaptobenzoic acid.....	48
Figure 2.5a	Spectra and schematic representation of single and dual-layered substrate.....	51
Figure 2.5b	SERS intensity vs nominal thickness of the spacer.....	51
Figure 2.6a	Representation of surface coverage evaluation experiment.....	54
Figure 2.6b	Spectra for surface coverage evaluation.....	54
Figure 2.6c	SERS intensity and surface coverage vs nominal thickness of the spacer.....	54
Figure 2.7a	Relative SERS intensities vs shelf life.....	57
Figure 2.7b	Normalized SERS intensities vs shelf life.....	57
Figure 2.8	Spectra and bar graph of substrates through a regeneration cycle.....	60
Figure 2.9	SERS intensity vs TiO ₂ coating layer thickness.....	62
Figure 2.10	Reflectance spectra of substrates coated with TiO ₂	63
Figure 3.1a	SERS intensity vs nominal thickness of the TiO ₂ spacer.....	75
Figure 3.1b	SERS intensity vs nominal thickness of the HfO ₂ spacer.....	75
Figure 3.1c	SERS intensity vs nominal thickness of the Al ₂ O ₃ spacer.....	75
Figure 3.2	Reflectance spectra of different dual-layered substrates.....	77
Figure 3.3a	SERS spectra from single and different dual-layered substrates.....	79
Figure 3.3b	Close up of SERS spectra from single and different dual-layers.....	79
Figure 3.4a	Mechanism of influence of Schottky barrier height.....	81
Figure 3.4b	Multi-layer enhancement vs Schottky barrier height.....	81
Figure 3.5a	Mechanism of influence of interface potential.....	83
Figure 3.5b	Multi-layer enhancement vs interface potential.....	83
Figure 3.6a	Mechanism of influence of dielectric constant.....	85
Figure 3.6b	Multi-layer enhancement vs dielectric constant.....	85
Figure 4.1	Scheme of the optical setup used for the Raman measurements.....	93
Figure 4.2	Scheme of the setup used for the reflectance measurements.....	94
Figure 4.3	SERS spectra of substrates through a regeneration cycle.....	95
Figure 4.4a	Reflectance spectra of new and regenerated Klarite (#302).....	97
Figure 4.4b	Reflectance spectra of new and regenerated Klarite (#312).....	97
Figure 4.4c	Reflectance spectra of new and regenerated Klarite (#313).....	97
Figure 4.5	Standard curves of new and regenerated Klarite.....	99
Figure 4.6a	Sensitivities vs regeneration cycle of Klarite.....	101
Figure 4.6b	Substrate-to-substrate deviation vs regeneration cycle of Klarite.....	101

Figure 4.7a Close up BA peak single and dual-layered Klarite.....	103
Figure 4.7b Sensitivities of single and dual-layered Klarite.....	103
Figure 5.1 Scheme of the optical setup used for the Raman measurements.....	113
Figure 5.2a Series of spectra from free probes in suspension.....	116
Figure 5.2b Series of spectra from a trapped probe.....	116
Figure 5.2c Series of projections from free probes in suspension.....	116
Figure 5.2d Series of projections from a trapped probe.....	116
Figure 5.3a SERS spectra of a free probes and a trapped probe.....	119
Figure 5.3b Close up of SERS spectra of a free probes and a trapped probe.....	119
Figure 5.4a Trapping enhancement vs concentration of probes.....	122
Figure 5.4b Signal of trapped probe vs concentration of probes.....	122
Figure 5.5 Signal of trapped and free probes vs additiona silver layers.....	124

Chapter 1:

From Understanding Plasmonics to Designing Structures for Surface Enhanced Raman Spectroscopy

1.1 Background and Significance

Analytical chemistry has pushed constantly the limits of sensing, making previously impossible practices a routine. Examples of challenges confronted by analytical chemistry are early detection of diseases (e.g., cancer) and trace detection of energetic materials (i.e., explosives). Both analyses require high sensitivities, due to the extremely low concentrations of the target to detect. Overcoming these challenges will benefit medicine and other key applications of analytical chemistry, but it requires improvements in the capabilities of current detection methods.

Optical sensors are non-invasive alternatives to sensing strategies that require a strong interaction with the sample, such as electrochemical sensors or techniques based on high energy electrons or photons. The majority of the currently used optical sensors, particularly in the bioanalytical field, are based on fluorescence due to the high throughput of this phenomenon. Fluorescence-based sensing has reached sensitivities that allow the detection of single molecules, as well as resolutions superior to their theoretical limits. Additionally, fluorescence sensors have been integrated in single cells.

While fluorescence-based sensors offer many advantages, this technique lacks in intrinsic analyte detection (i.e., measuring signal directly from the target molecule) and multiplexed detection (i.e., simultaneous detection of numerous targets). In fact, fluorescence-based biosensors consist of reporter molecules (fluorophores) that detect either the presence or the position of target species by binding to or reacting with the target molecule, respectively. Furthermore, fluorescence emission is characterized by a broad profile (50 - 100 nm), making it impossible to detect simultaneously a large number of analytes, associated with different reporters, without relying on complicated time-resolved or statistical methods.

Due to rapid advances in nanotechnology, optical sensors based on surface enhanced Raman scattering (SERS) have emerged as an alternative to fluorescence-based sensing. SERS sensors allow the intrinsic monitoring of an analyte, due to the structural information that can be obtained from the Raman scattering of species in close proximity to the sensor surface. Raman scattering is characterized by sharper peaks (< 1 nm) relative to fluorescence, due to its vibrational nature. This characteristic allows multiplexed measurements, which is important in the analysis of complex environments and processes occurring in biological systems.

Although utilizing Raman spectroscopy in optical biosensors offers many advantages, its inherently low signal can make the fabrication of high-throughput sensors challenging. The intensity of Raman scattering is 10 orders of magnitude lower than fluorescence emission. This disparity explains the expansive use of fluorescence in sensing technologies.

However, SERS substrates, or probes, have shown the ability to amplify scattering up to 14 orders of magnitude, proving the possibility to use SERS, and therefore Raman, in real-world sensing scenarios. The challenge for these enhancing structures is their low reproducibility rendering them unusable for intrinsic quantitative sensing, thereby voiding one of the main advantages of SERS-based optical sensors.

The project of this thesis is motivated by the necessity to fabricate SERS substrates with reproducible and significant signal enhancements. Over the years, many different structures have been fabricated by taking advantage of surface modifications on the substrates to improve their SERS enhancement. In our lab, a different strategy to amplify SERS was developed. The approach consisted in including alternating layers of different materials (i.e., a metal and a dielectric) in the volume of a SERS substrate. These novel structures were observed to increase the SERS enhancement by more than an order of magnitude over the initial enhancement of the probe (multi-layer enhancement). While modifying the surface of a substrate can result in changes in reproducibility, the advantage of this approach is to amplify the signal and the sensitivity of the SERS-based optical sensor without disrupting previously achieved reproducibility.

The focus of this thesis is on the material optimization of these multi-layered structures, as well as their applications in different systems. The following topics will be discussed herein, the theory and context that constitute the framework of the research; the effect that the dielectric spacer has in the structures on the overall enhancement; and the multi-layered structures applied to single probe sensors and commercially available SERS substrates.

1.2 Raman Spectroscopy

The research discussed in this thesis is based on SERS, a phenomenon that involves the amplification of Raman scattering. To aid the understanding of SERS and the experimental aspects of this thesis, this section will give a brief overview of the theory of Raman spectroscopy, discussing the classical and quantum theoretical treatment of Raman, as well as its selection rules and instrumentation. A complete treatment of Raman scattering and spectroscopy can be found in various reviews on the subject.¹⁻⁴

Scattering is one of several different ways that electromagnetic radiation (i.e., light) can interact with matter. This phenomenon arises from light passing through a molecule/particle and inducing a force on the charges that compose it. The dipole moment produced in the molecule by charge distortion oscillates, following the inducing electric field. An oscillating dipole is itself a source of electromagnetic radiation and will irradiate photons. These photons are called scattered photons, as their direction of propagation is not necessarily the same as the incoming electromagnetic radiation.

Most of the scattered photons undergo elastic scattering (Rayleigh) and conserve the same energy as the incoming radiation. Some molecules undergo in periodic vibrational motion, which can change the polarizability of the molecule. In this case, the photons scattered by the molecules will have a different energy with respect to the incoming radiation. This type of scattering is inelastic and is called Raman scattering.

Raman scattering was observed by C. V. Raman in 1928.⁵ Since its discovery, Raman spectroscopy has become a powerful analytical tool due to its ability to provide molecular structure information on a variety of samples. The theory and practical use of this spectroscopy are discussed in the following sections.

1.2.1 Classical Theory of Raman

In this section, the classical theory of Raman is treated briefly to provide the theoretical basis needed to understand selection rules of Raman spectroscopy, as well as the SERS enhancement mechanism.

When a molecule is immersed in an electric field, its charges experience a force that results in an induced dipole moment (μ_{in}), whose magnitude depends on the strength of the electric field (E), as well as on the polarizability of the molecule (α) which measures the tendency of the molecule electron cloud to be distorted (Eq 1.1).⁶

$$\mu_{in} = \alpha E \quad (1.1)$$

The same situation is experienced by a molecule when the inducing field is oscillating, such as for molecule irradiated by electromagnetic radiation.

The electric field component of the electromagnetic radiation can be expressed as

$$E = E_0 \cos(2\pi\nu t) \quad (1.2)$$

where E_0 represent the amplitude of the radiation (i.e., the electric field maximum intensity), ν its frequency and t time. Substituting Eq. 1.2 into Eq. 1.1 is obtained

$$\mu_{in} = \alpha E = \alpha E_0 \cos(2\pi\nu t) \quad (1.3)$$

which represent the periodical induction of a dipole due to the transient oscillating field. As mentioned above an oscillating dipole is a source of electromagnetic radiation and will scatter photons.^{6,7}

Raman scattering results from the influence of normal modes on the polarizability of a molecule. If the polarizability of the molecule varies due to a vibrational mode, considering its dependence on the latter for a single vibration its formula can be expressed as

$$\alpha = \alpha_0 + \left(\frac{\partial\alpha}{\partial r}\right) r_m \cos(2\pi\nu_{vib}t) \quad (1.4)$$

where α_0 is the polarizability at the equilibrium distance, $\left(\frac{\partial\alpha}{\partial r}\right)$ is the speed at which the polarizability changes with respect to the vibration coordinates, r_m is the maximum vibrational amplitude and ν_{vib} is the frequency of vibration. Substituting the vibration dependent expression for the polarizability (Eq 1.4) into Eq 1.3 yields

$$\mu_{in} = \alpha_0 E_0 \cos(2\pi\nu t) + E_0 \left(\frac{\partial\alpha}{\partial r}\right) r_m \cos(2\pi\nu t) \cos(2\pi\nu_{vib}t) \quad (1.5)$$

which represent an oscillating electric field inducing a dipole on a molecule with varying polarizability.⁶

Considering the trigonometric identities,

$$\cos(\alpha - \beta) = \cos \alpha \cos \beta - \sin \alpha \sin \beta \quad (1.6)$$

$$\cos(\alpha + \beta) = \cos \alpha \cos \beta + \sin \alpha \sin \beta \quad (1.7)$$

Eq 1.5 can be expanded to Eq 1.8, which explicit the Raman components of scattering.

$$\mu_{in} = \alpha_0 E_0 \cos(2\pi\nu t) + \frac{E_0}{2} \left(\frac{\partial\alpha}{\partial r}\right) r_m \cos(2\pi(\nu + \nu_{vib})t) + \frac{E_0}{2} \left(\frac{\partial\alpha}{\partial r}\right) r_m \cos(2\pi(\nu - \nu_{vib})t) \quad (1.8)$$

Eq 1.8 shows how a molecule irradiated with electromagnetic radiation of frequency ν has a total dipole moment with different frequency components, whose relative magnitudes are governed by the terms α_0 and $\left(\frac{\partial\alpha}{\partial r}\right)$, elastic and inelastic scattering, respectively. Rayleigh scattering is represented by the component of the induced dipole oscillating at a frequency ν and Raman scattering is represented by the components oscillating at the frequencies of $\nu - \nu_{vib}$ and $\nu + \nu_{vib}$, for respectively stokes and anti-stokes.^{6,8}

1.2.1 Raman Selection Rules

The intensity of the Raman scattering is proportional to the component of the induced dipole that oscillates at a frequency different from the inducing frequency (ν). Eq. 1.8 shows that the magnitude of these components is due to the term $\left(\frac{\partial\alpha}{\partial r}\right)$, which describes the speed at which the polarizability varies as a function of the vibration coordinates in the vicinity of the equilibrium coordinates. Thereby, for a vibrational mode to be Raman active there must be a change in the polarizability during its vibrational motion. Furthermore, vibrations that involve larger changes in the polarizability of the molecules will have a stronger Raman scattering.

1.2.2 Quantum Theory of Raman

According to its quantum-mechanical representation, scattering is a two photon process, consisting of an incoming photon and a scattering photon. When the incoming photon interacts with the electron cloud of a molecule it causes a non-stable distortion that is represented as the molecule being excited to a virtual excited state. This virtual state is

unstable, as it does not coincide to any electronic state of the molecule, and a second photon is instantaneously emitted to allow the molecule to relax back to a lower energy state.

The final state of this second transition can be the molecule initial state, for Rayleigh, or a different vibrational level of the fine structure of the electronic ground state, for Raman (Figure 1.1). In the case of a Raman photon, when the molecule is initially in the vibrational ground state and decays from to a higher vibrational level the energy of the scattered photon will be smaller with respect to the incoming photon and is called Stokes. In contrast an anti-Stokes photon arises from the scattering of a molecule initially found in an excited vibrational state that relaxes to the vibrational ground state. The scattered energy in this case will be greater than the energy of the incoming photon.⁹

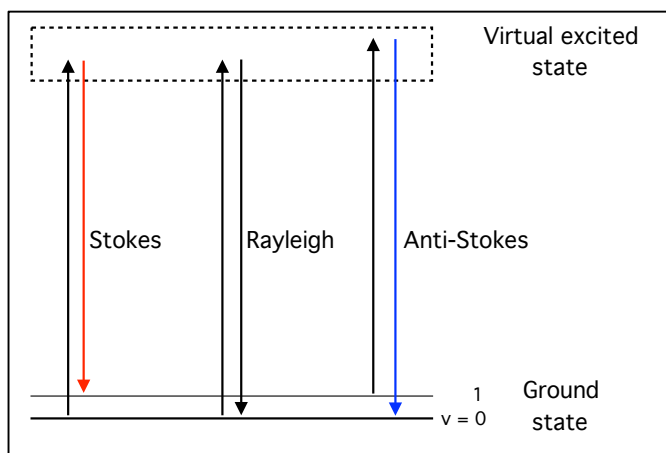


Figure 1.1. Energy-level diagram illustrating Raman scattering (Stokes and Anti-Stokes) and Rayleigh scattering

1.2.3 Raman Spectroscopy Instrumentation

In this section, the practical aspects of Raman spectroscopy are treated. The aim of this section is to provide the reader with the knowledge necessary to understand the experimental aspects of this thesis.

Raman spectroscopy was not often used for chemical analysis prior to the introduction of laser sources in Raman measurements. An excitation source for this type of spectroscopy has to be monochromatic and very intense. The first requirement is necessary to simplify the Raman spectrum as multiple excitation wavelengths would be inelastically scattered to the same Raman shift (i.e., $\nu_{Rayleigh} - \nu_{Raman}$) but at different absolute wavelengths. Additionally, the intensity requirement is due to the very small cross section of Raman scattering, as approximately only one out of 10^{29} photons is inelastically scattered. Laser sources satisfy both these requirements and are by far the most commonly used Raman excitation sources.

The wavelength used in the excitation source is not required be in a specific region of the spectrum but can strongly influence the output of the measurements due to its energy. Scattering decreases with the forth power of the wavelength, therefore sources with shorter wavelength give stronger Raman signal. However, to select an excitation source any

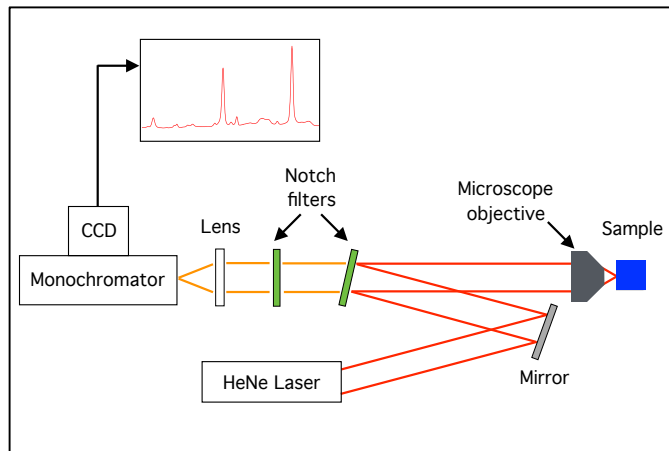


Figure 1.2. Schematic representation of a backscattered optical setup for Raman spectroscopy.

possible interaction that an intense laser radiation can have with the sample has to be considered. Long exposure to UV laser sources can cause the degradation of the sample and background fluorescence can also be a limiting factor for UV and visible sources. The most commonly used Raman sources are in the red and NIR region of the spectrum.¹⁰

A backscattered geometry (Figure 1.2) can be used in Raman spectroscopy to maximize the signal output. The higher efficiency of this geometry is due to the anisotropic angle distribution of the scattering, which is preferentially directed in the forward and backward directions, and due to the stimulated emission, that can be achieved due to the correspondence of the collection and excitation apparatus. To avoid that direct and elastically scattered laser light reach the read out system, the optical Raman setup has to reject the wavelength of the excitation source. Filters used to this end need a very narrow range of rejected wavelengths to be able to observe signal from low energy vibrations.²

The readout system for Raman spectroscopy requires a wavelength dispersion/selection device and a transducer. The monochromator utilized to separate the wavelengths must achieve the desired resolution to discern the Raman and Rayleigh scattering and, for complex samples, to resolve peaks from vibrations with similar energies. A resolution of 5 cm^{-1} is achieved in Raman spectra.¹⁰ The spacing between peaks in a Raman spectrum will vary with the excitation wavelength when measuring the absolute wavelength, as Raman shift and wavelength have reciprocal units. The transducer must be able to read very low signals. To this end, low noise charge coupled devices (CCD) are commonly utilized. Due

to the similarity between SERS and Raman spectroscopy, the optical setup for Raman spectroscopy can also be used for measurements.

1.3 SERS

The scope of this section is to provide a description of SERS and its optimization. The section begins with a brief overview of the field of plasmonics with an emphasis on the optimization of plasmonic structures for SERS. The theory and characteristics of SERS are also described followed by a review on the advancements in structures and substrates for SERS.

1.3.1 Plasmonics

The SERS phenomenon is based on exploiting the scattering characteristics of surface plasmons, which cause the observed enhancement. This section will briefly describe the field of plasmonics (i.e., the science that studies surface plasmons) to provide a background on SERS sensing and its optimization. For a more detailed treatment numerous articles and books have been written on the subject.^{7,11-13}

Theoretical Background

The field of plasmonics represents the study of the interaction of light with the conduction electrons of a metal.⁷ Such interactions in certain conditions lead to a collective excitation of conduction band electrons, a surface plasmon (SP).⁷ This phenomenon involves photons and electrons coupling to form a hybrid between a light wave and an excited electronic level. This phenomenon produces an enhanced optical near-field at metal/dielectric interfaces,

known as SP, or within metallic nanostructures, known as localized surface plasmons (LSP).^{7,11} The energy of the SP resonance depends on the competing forces involved in the phenomenon, the light-induced excitation and the nucleus-electron interactions. Variation of the shape, material composition and number of structures can each greatly affect the resonance energy of this phenomenon, which can be tailored for different sensing applications.¹⁴⁻¹⁷

Tuning Surface Plasmons in Plasmonic Structures

While coinage metals (i.e., silver, gold, copper) represent the most commonly employed plasmonic materials due to the relationship between conductivity (i.e., electron losses, etc.) and surface plasmon magnitude, many different materials have been investigated over the past couple decades, with more recent studies investigating common and exotic metals.^{16,18,19} The frequency of the SP depends on the conductive electrons density of the material causing analogous structures made with different materials to exhibit SP at different wavelengths.^{16,19}

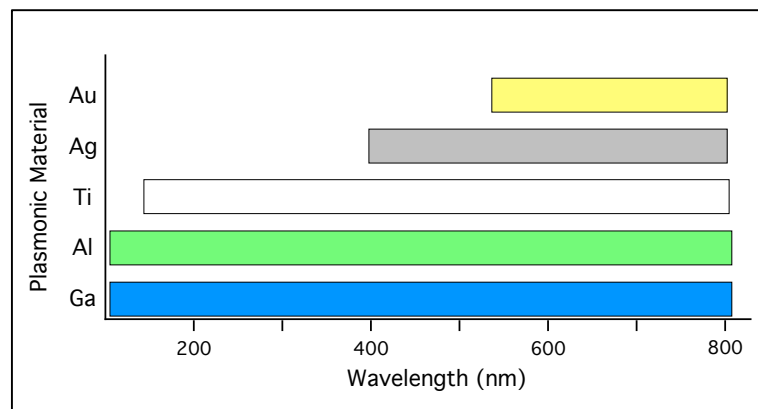


Figure 1.3. Tuning ranges of common plasmonic materials.

Figure 1.3 shows the SP tuning ranges of several of the more common plasmonic materials studied to date. As can be seen gold and silver, while often exhibiting intense plasmons, are limited in the visible and near infrared (NIR) region of the electromagnetic spectrum whereas poor metals, such as aluminum, can sustain SPs in an extended region of the spectrum but often with significantly reduced magnitudes.¹⁸ In the case of gold, one of the longer wavelength material, interband transitions dissipate the SP at wavelengths lower than 550nm, limiting its usefulness primarily to the red and near infrared regions of the electromagnetic spectrum.¹⁸

In addition to material composition, the shape and size of the material also plays a large role in determining the optimal energy for exciting a surface plasmon. A demonstration of this effect has been shown by investigating different size nanospheres as well as non-spherical particles (e.g., nanorods).^{15,20} An example of this shape dependence is displayed in Figure 1.4a which shows the resonance wavelength dependence for longitudinal LSPR of gold nanorods as a function of their relative lengths (as quantified by their aspect ratios at constant width). As can be seen from this plot, the SP wavelength of the longitudinal mode increases for larger lengths. The experimental data (circles) are in good agreement with the theoretical values (solid line) derived from Mie theory modified for spheroids.²⁰⁻²² A similar trend can also be seen in Figure 1.4b where the SP absorption maximum of silver islands is plotted in function of their size.²³ The silver island case is more complicated with respect to a single rod but it reinforces the importance of the nanostructure size. In conclusion, as shown in the Figures 1.3 and 1.4 both shape and material play a key role in

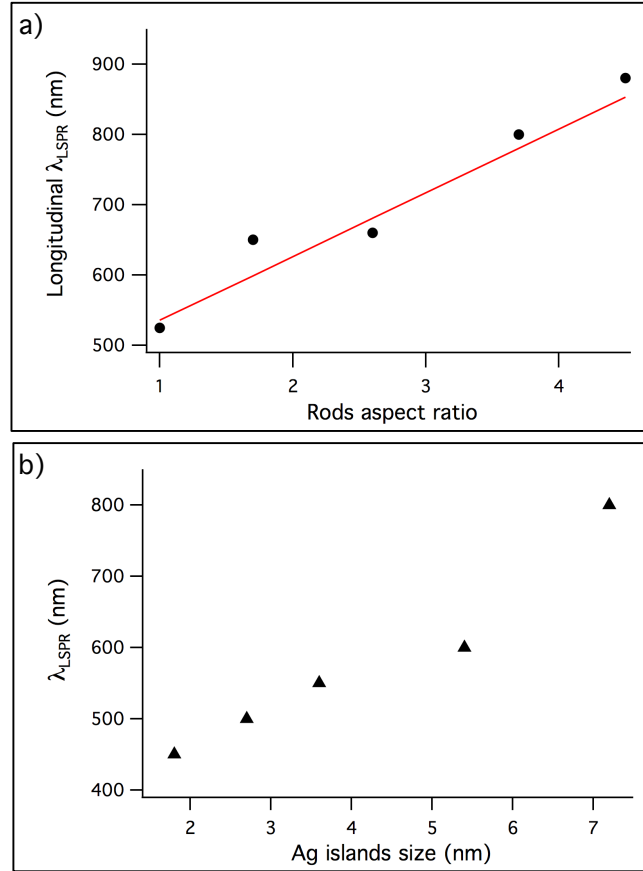


Figure 1.4. **a)** Experimental (circles) and theoretical (line) wavelengths of LSPR maxima of gold nanorods as a function of their aspect ratio (longitudinal/transverse). **b)** Experimental wavelengths of LSPR maxima of silver islands as a function of their size.

the plasmonic characteristics of a nanostructure and can be tuned to obtain optimal SERS enhancements.

1.4.1 Historical Background

SERS was first observed in 1974 but its description as a unique plasmonic phenomenon was made in 1977.²⁴⁻²⁷ In the initial observations, molecules adsorbed on nanoscale roughed silver electrodes exhibited enhanced Raman scattering.²⁴ In the following years, the strong link between SERS and the nanoscopic structure of the substrate, as well as to its plasmonic characteristics were theorized and described in detail.²⁸⁻³¹

1.4.2 Theory of Enhancement Mechanisms

The enhancement mechanism of SERS has been historically divided into two processes, chemical enhancement (CHEM) and electromagnetic enhancement (EM).³²⁻³⁴ The CHEM enhancement is sample-dependent and is commonly ascribed to the differences in the state of a molecule when in contact or in close proximity to a metallic surface.³⁵ These locations can generate variations in the Raman cross section as well as a shift for resonance Raman phenomena, changing the Raman scattering intensity.³⁵ The CHEM enhancement contributes to the total SERS enhancement for a factor of 100-1000,^{36,37} while the largest portion of SERS is due instead to the EM enhancement, which amplifies Raman signals of 10^6 to 10^{11} -fold.³⁶ In addition, the EM enhancement is connected to the characteristics of the substrate and therefore the principal focus in the optimization of SERS structures.

The current view of the mechanism for the EM enhancement consists in a plasmonic nanostructure working as an antenna and amplifying the incoming and scattered radiation. Figure 1.5 shows a schematic representation depicting this enhancement process. As described in section 1.2.1, Rayleigh and Raman scattering are generated by an oscillating induced dipole, which is proportional to the intensity of the field that the analyte molecule experiences, and is expressed in Equation 1.8. When the incoming radiation excites a SP on a nanostructure it generates an oscillating field of the same frequency but of increased

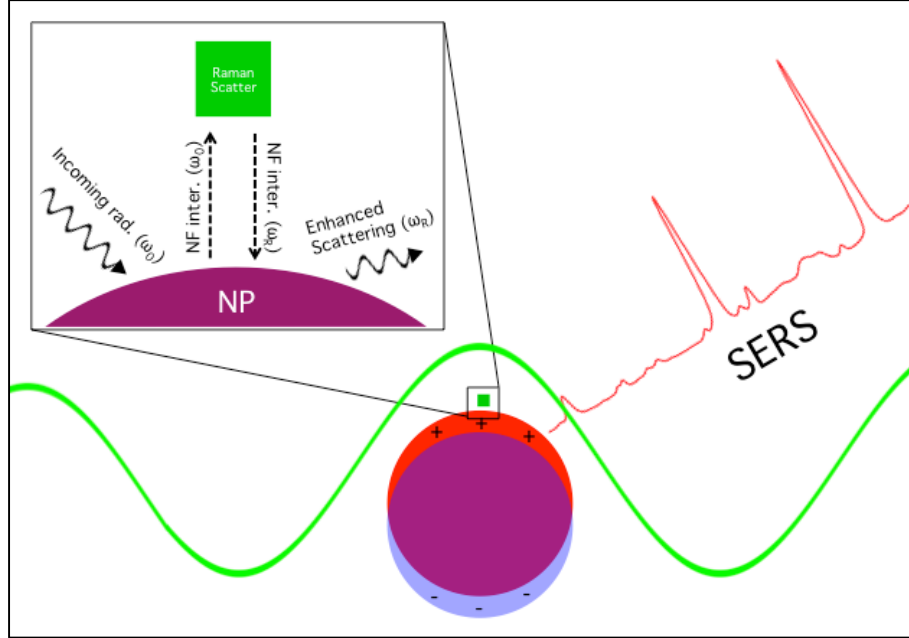


Figure 1.5. Schematic of the EM enhancement of SERS showing the processes involved. An incoming radiation of resonant wavelength (ω_0) interacts with the nanoparticle exciting a LSPR. The near field interaction associated with the position of the Raman scatterer increases the scattering intensity. The scatter radiation at wavelength (ω_R) also interacts with the nanoparticle and is scattered by it with a further enhancement.

intensity.^{7,38} This effect only extends in proximity to the metallic surface and decays exponentially with distance resulting in the need for a close contact between the analyte and the nanoparticle surface to obtain an enhancement.³⁹ The enhanced electric field from the surface plasmon increases the magnitude of the induced dipole, which can be expressed as

$$\mu_{in} = \alpha g E_0 \quad (1.9)$$

where g represents the enhancement of the electric field experienced by the molecule in the presence of the plasmonic nanostructure.³² As for the inducing field, also the Raman scattering field is enhanced by the plasmonic nanostructure of a factor g_I .³² Therefore, the amplitude of the enhanced Raman scattering field (E_{SERS}) generated by the oscillating dipole will be proportional to the product of the field enhancements for the incoming and

scattered radiations (Eq 1.10). To note, the observed scattering in SERS originates from the metallic nanostructure.

$$E_{SERS} \propto \alpha g g_1 E_0 \quad (1.10)$$

This equation can be simplified considering equal the factors g and g_1 , due to the small difference in enhancement between the frequencies of Raman and Rayleigh scattering, making Eq 1.10 equal to

$$E_{SERS} \propto \alpha g^2 E_0 \quad (1.11)$$

The SERS enhancement (i.e., the enhancement in the intensity of the Raman scattering) can be extrapolated by Eq 1.11, as the scattered light intensity is proportional to the squared of the module of the electric field making the SERS intensity representable as

$$I_{SERS} \propto g^4 |E_0|^2 \quad (1.12)$$

Equation 1.12 shows how the EM component of the SERS enhancement is equal to the fourth power of the electric field enhancement. The latter can be extrapolated from numerical calculations which have shown agreement with this theoretical treatment.³⁸

As described above, the mechanism for the EM enhancement is caused by the enhancement of incoming and scattering field suggesting that the optimum SERS substrates would have a SP resonance halfway between the target Raman band and the excitation wavelength.^{40,41} This expedient can in fact maximize the field enhancement for the incoming and scattered frequencies, due to the overlapping with the SP resonance. As an example, for SERS substrates intended to enhance the fingerprint region of a Raman spectrum and employing 633 nm laser source, the SP resonance should be in the 644 - 679 nm range.

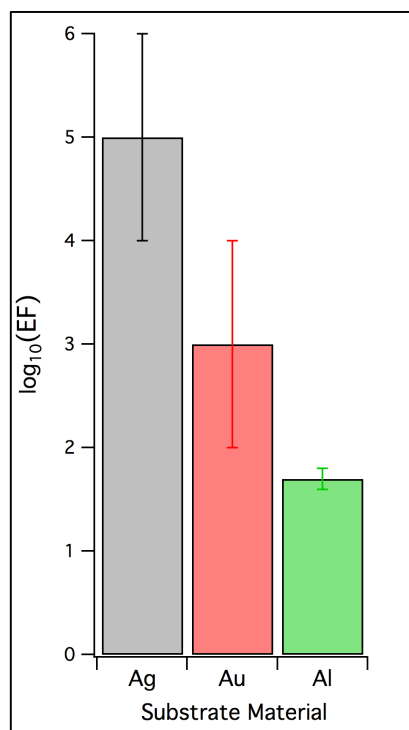


Figure 1.6. Histogram representing the orders of magnitude of SERS enhancement with respect to different materials.

In addition to tuning the SP excitation wavelength, the use of different metals and nanostructures for SERS substrates can also influence many other critical sensing parameters, including: the metal surface accessibility for direct contact with an analyte, the surface area for analyte interaction, as well as the localized focusing of the electric field. All of these interrelated phenomena must be considered for the specific sensing application. For instance, gold is considered a superior material for many applications due to its inertness, whereas silver, copper or aluminum SERS nanostructures can present a challenge due to their rapid oxidation in ambient conditions. Alternatively, the EM enhancement obtainable for each metal is different due to interband transitions and other loss sources.^{19,42} These differences can be seen in Figure 1.6, which shows that comparable SERS substrates (excited with optimal laser wavelengths) composed with either gold, silver or aluminum resulting in over two orders of magnitude greater SERS enhancement for the silver-based

substrates than the next best material (i.e., gold), which is better still when compared to non-coinage metals (i.e., aluminum).^{15,42,43}

1.4.3 SERS enhancement factor

To compare the performances of different substrates, the enhancement obtained with a SERS substrate/structure is usually quantified using the SERS enhancement factor. This factor can be expressed as absolute enhancement factor (EF) or as analytical enhancement factor (αEF).

EF measures the real enhancement relative to a SERS substrate and can be used, for example, to determine the agreement with theoretical calculation on the expected enhancement. EF can be calculated with the following equation^{32,44}:

$$EF = \frac{I_{SERS} \cdot N_{Raman}}{N_{SERS} \cdot I_{Raman}} \quad (1.14)$$

where the I_i is the signal intensity and N_i is the number of molecules responsible for the signal in SERS measurement (SERS subscript) and in spontaneous Raman measurement (Raman subscript). Equation 1.14 requires to calculate the number of molecules that are involved in the SERS signal. The density of the molecule on the surface and the surface area of the irradiated region on the substrate must be known.

αEF is an enhancement calculation specific to an application as it measures the enhancement offered by using SERS in place of Raman to detect a target species. This factor can be calculated with the following equation⁴⁴:

$$\alpha EF = \frac{I_{SERS} \cdot C_{Raman}}{C_{SERS} \cdot I_{Raman}} \quad (1.15)$$

where C_i represents the concentration of the target analyte in the spontaneous Raman and SERS measurements. This method measures the efficacy of a substrate in measuring a target molecule at a specific concentration. The α EF will result in a lower value with respect to the EF as it takes into account all the target molecules present in the sample, whereas the number of molecules responsible for the SERS signal is due to the partition of a molecule between the substrate surface and the sample medium. Recently, the Army Research Lab developed the SERS enhancement evaluation protocol, a procedure that improves over the α EF and consists in observing the behavior of the SERS and Raman signal as a function of concentration and calculate the enhancement in a set range of concentrations.⁴⁵

1.4.4 SERS Applications

An important class of SERS applications is to substitute fluorescence-based techniques in bioanalyses. The main advantage offered by SERS for such applications is the vibrational fingerprint that is obtained from chemical species in close proximity to the sensor surface.^{32,46} This characteristic allows the direct monitoring of the target analyte and for the detection of changes in its chemical structure.⁴⁷ In fluorescence-based sensing the signal is emitted from reporter molecules bound to a target rather than directly from the analyte. The possibility of highly multiplexed detection with SERS-based sensing can be used to monitor complex systems, which can require the simultaneous detection of numerous targets.⁴⁸⁻⁵⁰

The independence of SERS from the excitation wavelength makes it a versatile technique, as the laser source can be tailored for a specific application. NIR excitation is commonly used in the analysis of biological systems to suppress fluorescence background. NIR laser wavelengths have also been used in SERS sensing *in vivo*, through the skin,^{51,52} and through bone with the aid of surface offset Raman.⁵³ Visible laser sources are commonly used to further amplify the signal via resonance Raman to obtain high throughput SERRS sensors.^{54,55} Such sensors have the disadvantage of sacrificing intrinsic sensing to obtain high signal enhancement, because they require a reporter molecule that gives resonance Raman at the desired wavelength. UV-SERS can be used to amplify the Raman signal due to the frequency dependence of scattering intensity and the increasing number of molecules available for resonance Raman. However, UV-SERS has been rarely reported due to issues with the fabrication of its substrates.^{43,56,57}

Additional SERS applications are in probing surface chemistry and in non-destructive trace detection, for forensics or art conservation. While vibrational spectroscopies are generally useful in these fields due to their identification capabilities via vibrational fingerprint, SERS has the advantage of simple and non-invasive sample preparation. SERS has been used to study surface processes as the growth of films with ALD and catalytic oxidation of biomolecules.^{58,59} In conservation science SERS has been used to identify the origins of an artifact, as well as to understand the correct route to its restoration.⁶⁰ Similar principles have also been applied to detect the provenience of fibers and paints for forensic purposes.⁶¹ This widespread of SERS applications observed in recent years is the result of research focused toward structures capable of large and reproducible SERS enhancements.

1.4.4 Nanostructures for SERS sensing

The aim of this section is to highlight significant substrates traditionally used to amplify the SERS signal. Although a large number of different types of nanostructured SERS substrates exist, with their numbers continuing to expand, they can be classified as belonging to (or evolving from) two different categories; (i) individual or randomly oriented aggregates of nanoparticles or (ii) ordered arrays of nanoparticles.

Individual/Randomly Orientated Nanoparticles

Individual nanoparticles and random aggregates of nanoparticles (e.g., colloids) have long been used to perform SERS sensing due to their small size and in their large enhancement potential. Individual spherical metallic nanoparticles (e.g., individual colloidal particles) have been demonstrated, theoretically and experimentally, to be capable of providing EF as great as 10^6 .^{36,42,44} This significant enhancement is due to the localization of the surface plasmon on the nanoparticle, resulting in a increased local electric field. This effect is further enhanced using nanoparticles with edges (e.g., nanorods, etc.) that are capable of focusing the charges (i.e., electric field) to specific locations on the nanoparticle via the “lightening rod” effect.^{29,36,62}

In the 1990’s SERS enhancement factors as great as 10^{14-15} were measured using colloidal aggregates of metallic nanoparticles, allowing for Raman scatter from individual molecules to be measured.⁶³⁻⁶⁵ These extreme SERS signal enhancements arise from the interaction

of the overlapping electric fields of adjacent nanoparticles that were excited parallel to the inter-particle axis, generating enhancing regions between the nanoparticles known as “hot spots”.^{32,66} Unfortunately, the ability to generate reproducible and controllable “hot spots” has proven difficult, resulting in irreproducible SERS enhancements from such aggregates.⁶⁷ Furthermore, the enhancement measured here was for a single location which differ from the enhancements measured as an average over the whole substrate. For these reasons, many of the most recent advances in SERS sensing have revolved around nanoparticle fabrication methods focused on generating sharp intraparticle edges, as well as method of inducing for organized aggregation of nanoparticles.

Ordered Nanostructure Arrays

To avoid the reproducibility issues associated with individual and random aggregates of SERS nanoparticles (e.g., colloidal solutions, etc.), ordered arrays of nanoparticles have also been explored over the past three decades, including electron beam lithography (EBL) arrays⁶⁸, metal island films⁶⁹⁻⁷¹, metallic films over nanospheres/nanostructures (MeFON)^{69,72}, and nanosphere lithography (NSL) arrays^{14,57}. Although these systems typically exhibit lower EF (typically $10^3 - 10^8$)^{70,73} than colloidal nanoparticle aggregates, they can exhibit uniform SERS signals across extended areas ($< 10\%$ RSD)⁷⁴, thereby providing a suitable surface for quantitative SERS analyses. In addition, each of these methods also provides a simple means of controlling the optimal plasmon excitation wavelength for the array. In the case of EBL, the precise control of the size of lithographically produced nanostructures provides plasmon tunability, while the amount of metal evaporated and the size of the underlying nanostructures employed in metal island

films, MeFON and NSL control allow for precise control of the optimal plasmon excitation wavelength. Recent advances in plasmonic arrays for SERS sensing (described in the following section) have focused on improving the EF achievable using novel shapes and materials (i.e., mixed metals, etc.) while retaining the precise control possible with these extended surface substrates.

1.4.5 Recent advances in SERS structures for SERS sensing

This section discusses the state of the art of structures for SERS. Significant recent advances in plasmonic nanostructures for SERS sensing over the past decade have revolved around: (i) optimization of fabrication methods for the synthesis of irregular shaped nanoparticles, (ii) fabrication of organized arrays of nanoparticles, and (iii) the use of mixed materials for increased signal enhancement, sample compatibility and/or recyclability. The following section highlights significant recent advances in plasmonic nanostructures for SERS sensing.

Irregular shapes

To improve the SERS enhancement, fabrication methods for generating structural motifs resulting in sharp predictable edges have been studied over the past decade. Recently, many studies have focused on simple fabrication methods for the realization of high aspect ratio structures that maximize the electric edge effect. Such nanostructures have been fabricated on a planar platforms (i.e., aligned nanorods),^{75,76} on underlying high aspect ratio nanostructures (e.g., nanospheres, nanorods, etched fiber bundles, etc.),^{41,77,78} and as individual nanoparticles in solution (i.e., nanostars).^{79,80}

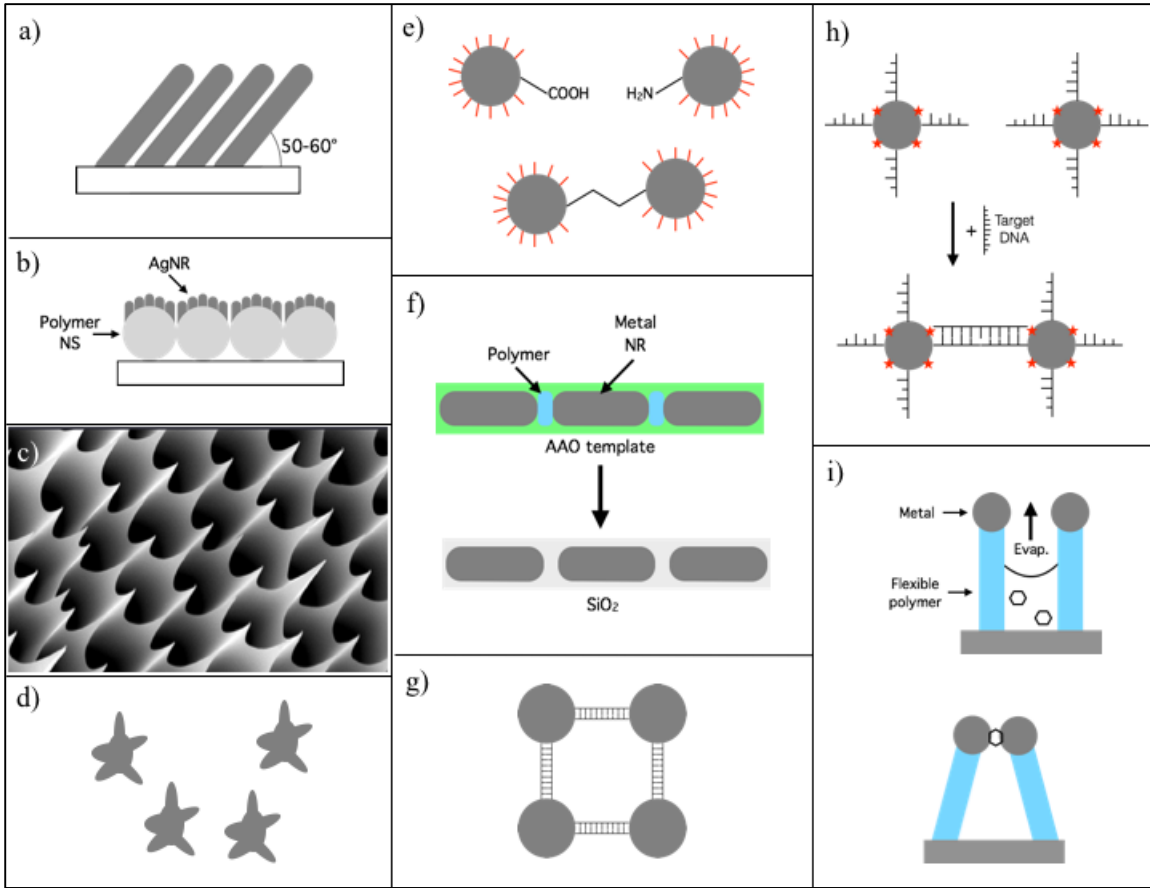


Figure 1.7. Representative images of recent nanostructures for SERS sensing: aligned nanorods fabricated through OAD (a), INRA, nanorods deposited on polymer nanospheres (b), a SEM micrograph of the fiber bundle used as high aspect ratio substrate (c), nanostars, branched nanoparticles with multiple high curvature edges (d), dimers fabricated through asymmetric functionalization (e), nanorods dimers fabricated using OWL (f), controlled aggregate fabricated via DNA-origami functionalized with NP (g), mechanism of action of DNA SERS sensors (h), mechanism of action of nanofingers, polymer rods partially coated with metal (i).

In the case of planar substrates, one of the simplest fabrication methods is the physical vapor deposition of aligned nanorods (see Fig. 1.7a) at extreme angles.^{75,76} These substrates are fabricated by depositing 200-500nm of silver on a glass slide which is rotated at angles greater 75° from the horizontal position.⁷⁵ The resulting substrates end up with a series of high aspect ratio nanorods aligned at a 50-60° angle with respect to the slide.⁷⁵ Taking advantage of the lightning rod effect as well as the semi-ordered, aligned array, these

nanostructures offer EF as high as 5×10^8 ,⁷⁶ with good reproducibility, all using a one-step fabrication process.

The use of sharp edges and high aspect ratio structures have also been applied to MeFON substrates.^{41,78} One method developed for fabrication of such substrates results in the generation of immobilized silver nanorods assemblies (INRA) on polymeric spheres (see Fig. 1.7b).⁷⁸ In this method, silver is deposited via physical vapor deposition on polymer nanospheres while being rapidly spun (~ 550 rpm). Based on the particular deposition conditions employed (i.e., sphere size, rotation rate, etc.) an array of aligned silver nanorods is created. By varying the size of the nanospheres used to make the underlying monolayer, the LSPR can be varied to tune the surface plasmon absorption maximum.⁷⁸ Employing this method, silver substrates generated have been shown to exhibit plasmon absorption maxima that can be tuned from 450 to 1100 nm (with nanospheres ranging in size from 320 and 790 nm) while having EF of $10^7 - 10^8$.⁴¹

Another developed plasmonic nanostructured array with sharp edges that has demonstrated significant EF was fabricated by coating tapered and chemically etched fiber optic imaging bundles with metal via vapor deposition (see Fig. 1.7c).⁷⁷ Employing fiber optic imaging bundles that are tapered with a micropipette puller and etched with hydrofluoric acid, an array of pyramidal shaped spikes is generated, with each metal-coated spike capable of focusing the electric field on its edges. Additionally, by varying the tapering parameters, the spacing between the individual pyramidal spikes can be varied altering the electric field

interaction between spikes. Using such pyramidal nanostructures, silver coated versions of these substrates have been demonstrated to exhibit EF as great as 10^9 .^{77,81}

While fabrication of extended arrays of sharp edged SERS substrates are useful for many applications, analysis of microscopic and nanoscopic environments (e.g., intracellular) with SERS requires much smaller SERS substrates that do not require aggregation but still provide significant enhancement. Sharp edged, branched SERS nanoparticles known as nanostars (see Fig. 1.7d) have been developed for such analyses.⁷⁹ The high anisotropy of these plasmonic nanostructures result in greatly enhanced electric fields in multiple spots on the star's surface due to the lightning rod effect.⁸² Furthermore, the optimal plasmon absorption band of these structures is tunable by varying the core diameter to branch length ratio.⁷⁹ Employing this nanostar configuration, individual gold nanostars have been demonstrated to possess α EF as large as 4×10^5 , which is two-fold larger than comparable non-starred silver nanoparticles, while conserving the stability and biocompatibility inherent to gold.⁸⁰

Organized structures

Since hot spots associated with nano-gaps between two or more SERS active nanoparticles within a few nanometers of each other are known to generate the largest possible electric fields and corresponding SERS enhancements, the desire to fabricate nano-gap arrays with ordered spacings has been a highly active area of research. By generating such ordered arrays, the potential for reproducible and sensitive quantitative SERS analyses exists. In addition to the development the of patterned arrays there has also been a great deal of recent

research into the development of isolated SERS active nanoparticle dimers⁸³⁻⁸⁷ and target triggered, ordered nanoparticle aggregates.^{54,88-91} Such ordered arrays and isolated dimers offer the potential of significantly enhanced SERS signals over individual particles or larger ordered arrays, with good reproducibility.

Several different methods have recently been developed for the fabrication of isolated SERS active dimers or organized aggregates. One such method includes asymmetrically functionalizing of SERS nanoparticles with thiol linkers that are then used to attach to complimentary nanoparticle forming the dimer (see Fig. 1.7e).^{83,84} Alternatively, isolated dimeric structures have also been fabricated, with a high degree of precision, by a process known as on-wire lithography (OWL in Fig. 1.7f). In OWL, alternating layers of gold nanorods and sacrificial polymer are electrochemically grown to specific lengths in anodic aluminum oxide (AAO) templates. After dissolution of the AAO template, the gold polymer rod is coated with silicon dioxide and the polymer layer is dissolved creating a gold dimer of precise dimensions.⁸⁵ Because of the precise control over the size and spacing of the linked gold nanoparticles, the surface plasmon absorption wavelength can be readily tuned to the desired wavelength for a particular application and EF as great as 10^9 have been reported.⁸⁶ Another class of dimer/organized aggregate that has been refined over the past decade has been DNA and RNA origami-based structures (see Fig. 1.7g).⁸⁷ Unlike the previous dimer fabrication methods, the oligonucleotide specific interactions associated with DNA and RNA allow for much more diverse and complicated structures to be formed. However, the complexity of forming such elegant and well defined is limited by the melting and binding conditions required for each different interaction. To provide plasmonic

nanostructures, the oligonucleotides are functionalized with colloidal metal nanoparticles at specific locations, providing a means of coordinating the nanoparticles with precisions based on the flexibility of the oligonucleotide sequence employed.⁸⁷

An alternative approach to controlled aggregation of SERS nanoparticles that has recently seen growth for SERS sensing applications has been analyte-induced or triggered nanoparticle aggregation based systems (see Fig. 1.7h).^{54,88,89,91} This sensing strategy was first developed as a colorimetric detection platform in which the analyte induced aggregation resulted in a measurable color change,^{92,93} but has since been applied to solution based oligonucleotide sensing applications via SERS. In the SERS-based version of this technique, two different batches of ssDNA and Raman reporter molecule bound SERS nanoparticles are fabricated.⁵⁴ One batch of these nanoparticles contains a ssDNA sequence complimentary to one half of the target/analyte oligonucleotide sequence and the other batch contains a ssDNA sequence complementary to the other half of the analyte oligonucleotide. When these two batches of labeled nanoparticles are in the presence of the desired analyte sequence, controlled dimers are formed resulting in a greatly enhanced Raman signal from the reporter molecules on the nanoparticles' surface.⁵⁴ Similarly, aptamers have also been employed as the analyte targeting sequence responsible for nanoparticle dimerization, allowing for this concept of analyte-induced aggregation to be expanded beyond DNA and RNA sensing applications to other target species such as proteins.⁸⁹

The possibility of using hydrodynamic forces to trap analyte molecules in a SERS active nanogap has been demonstrated as a complimentary method to analyte-induced aggregation.⁹⁰ In this work, SERS active nanostructures known as nano-fingers (see Fig. 1.7i) trap the analyte of interest in a highly SERS active environment for detection. These nano-finger traps consist of an array of polymeric flexible nanorods whose extremities are coated with a metal nanoparticles.⁹⁰ These nanofingers are exposed to a solution containing the analyte of interest and are then allowed to dry. As the sample dries the rods bend due to the capillary forces experienced during evaporation and form aggregates around the few molecules left in the nanogap, providing an aggregated SERS substrate with large EF.⁹⁰

Mixed materials

Due to the strong influence the physical properties of the metal within which the plasmon is supported and the immediate surrounding play on the magnitude and shape of the resulting electric field, many recent advances have been made using mixed material nanostructures for enhanced SERS sensing. Structures fabricated with multiple materials have been exploited to tune the plasmonic characteristics of the substrates, to add functionality to the substrate or to increase local electric field strengths.

One of the earliest and most prominent of these mixed material nanostructures for SERS sensing are known as core-shell nanoparticles, which consist of a dielectric core coated with a metallic shell. Often consisting of a silica nanoparticle core and coated by metal via chemical reduction of metal salts, these nanoshell structures provide the ability to tune their LSPR absorbance by modifying the core/shell radii ratio.^{20,94-96} Unlike colloidal metal

particles, these core-shell nanostructures allow for fabrication of nanoparticles for SERS applications that can be tuned for optimal excitation with various wavelengths without a concomitant change in particle size. The presence of the dielectric core helps localize the surface plasmon to the metal surface, resulting in larger electric fields and corresponding EF with respect to comparable all metal nanoparticles.^{97,98}

Dielectric shells have been used in SERS substrates to provide a protective layer for both the local environment being sensed as well as the metal surface itself.^{71,99-102} Shell isolated nanoparticle-enhanced Raman spectroscopy (SHINERS), in which ultrathin layers of metal oxides (e.g., Al₂O₃, SiO₂, MgO) are uniformly coated via atomic layer deposition (ALD) have been demonstrated to provide SERS nanoparticle substrates that are protected from the often oxidizing environment of the sample.^{101,102} With many of the best SERS enhancing metals (i.e., silver, copper, etc.) often suffering from rapid degradation in SERS enhancement due to oxidation of the plasmon supporting metal surface, such metal oxide coated nanoparticles have resulted in significantly increased usage times. By employing ultrathin coating methods with high conformity, the decrease in electric field strength at the sensing surface can be minimized resulting in SERS EF not much lower than comparable uncoated nanoparticles.⁷¹ In addition to protecting the surface from oxidation, such ultrathin surface coatings have also been demonstrated to reduce aggregation of particles by preventing surface interactions, resulting in isolated particles that can be used in applications where aggregates are not suitable.

In addition to employing mixtures of dielectric materials with metals, plasmonic nanostructures consisting of semiconductor materials coated with thin metallic layers have also been developed and demonstrated for SERS sensing. By fabricating plasmonic nanostructures with a TiO₂ or ZnO core and a thin metal coating, “self-cleaning” SERS nanostructures can be generated^{103,104} in the case of these particular semiconductors, exposure to UV light results in the release of oxidizing electrons.¹⁰⁴ These electrons can travel through the thin conductive metallic shell, oxidizing and cleaning materials adsorbed, allowing for regeneration of the SERS active surface. While such SERS nanoparticles address a common problem in SERS sensing (i.e., substrate reusability) and have been demonstrated to be capable of being reused multiple times, the metal surface is susceptible to flaking during the regeneration cycle and is not capable of removing tightly bound species such as thiols, potentially limiting their useful lifetimes.

1.5 Multi-layered Structures

Although multi-layered structures can be considered a particular case of mixed materials, unlike other member of this category the multi-layered nanostructures offer a mean to further increase the SERS enhancement in a substrate.^{74,77,81,105-107} These structures are based on alternating films of a metal and a dielectric, with the latter used as a spacer between metallic films. This geometry has shown to enhance the SERS signal on its outermost metallic surface with respect to an analogous substrates made with a single layer (multi-layer enhancement). Figure 1.8 depicts the structures and representative SERS spectra for a single and a multi-layered structure. The mechanism of enhancement is currently under investigation and has been hypothesized to be dependent on the interaction

of the surface plasmons excited on proximal metallic layers. Similar effects have in fact been observed and demonstrated in comparable geometries.^{108,109}

The advantage offered by these structures is the additive nature of their enhancement. The enhancement obtainable with these structures has been demonstrated to increase as a function of additional deposited metallic layers separated by a dielectric spacer.⁷⁴ Furthermore, the multi-layer enhancement can be applied on a SERS substrate to further amplify its signal enhancement without disrupting the substrate characteristics. This feature is possible due to the enhancement mechanism being exploited in the volume of the probe rather than on its surface, as in most strategies of enhancement. This particular characteristic permits the amplification of the sensitivity of a SERS sensor without modifying either its reproducibility or sensing mechanism.

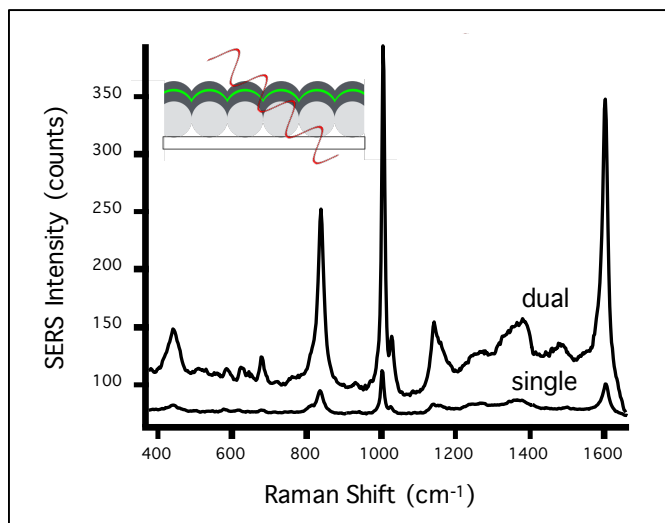


Figure 1.8. Benzoic acid SERS spectra from a single layered (single) and dual-layered (dual) AgFON substrate with the schematic representation of the dual-layered substrate used.

Multi-layered structures were first discovered in our lab on silver substrates and made with alternating films of silver and silver native oxide.⁷⁴ Their fabrication consisted in the deposition of a thin silver film (≈ 100 nm) followed by the air oxidation of its surface prior to the deposition of an additional silver film.⁷⁴ The oxidation time of the silver film was observed to influence the enhancement obtainable in a non-monotonic fashion. The enhancement increased for low oxidation time for then decreasing after reaching a maximum for 50 hr.⁷⁴ This behavior was ascribed to the formation of an monolayer of oxide on the surface of the metal. For optimized oxidation times these structures were shown to enhance the SERS signal on their outermost surface of 2.7-fold for a dual-layered structure. Multi-layered structures based on silver similar to those developed in our lab have been applied to SERS sensing with different substrate geometries,^{81,110,111} as well as to enhance the surface enhanced infrared absorption (SEIRA) in split ring resonators.¹¹²

While gold is considered a better alternative to silver in SERS substrate due to its superior biocompatibility and stability, the inherently lower enhancement of this material makes its use in SERS sensing challenging. The development of highly enhancing multi-layered structures based on gold can be used to counteract the negative effect of switching from silver. Initial development of such structures were fabricated mimicking silver/silver oxide structures by depositing on the gold surface silver islands that were allowed to completely oxidize.^{106,107} Such structures were observed to enhance the SERS signal of 1.4-fold, with this reduced multi-layer enhancement due to the low surface coverage of the silver islands. Additional gold multi-layered structures were fabricated with SAM as dielectric spacers.¹¹³ In particular these structures were used as a model system to elucidate the mechanism of

enhancement, taking advantage of the tunable characteristics of the SAM. These studies demonstrated how the enhancement is dependent on the chain length, as well as on the nature of the functional groups, of the SAM used.¹¹³ The convolution of packing density and number of defect sites for very low chain length and for polar functional group did not allow a complete understanding of the role of the dielectric spacer and of enhancement mechanism.

The use of ALD-deposited dielectric spacers in multi-layered structures is described, as well as the use of these structures in relevant SERS applications. The use of solid state spacers based on ALD are shown to solve part of the issues faced with SAM. Such structures were used to study the dependence of the multi-layer enhancement on the thickness of the spacer, demonstrating the origin of the non-monotonic behavior. The dependence of the multi-layer enhancement on the physical properties of the spacer was also studied and will be discussed herein. The multi-layered structures were applied to different systems (i.e., a single probe and a planar SERS substrate) to demonstrate the versatility of the enhancement mechanism.

1.6 References

- (1) Lyon, L. A.; Keating, C. D.; Fox, A. P.; Baker, B. E.; He, L.; Nicewarner, S. R.; Mulvaney, S. P.; Natan, M. J. *Analytical Chemistry* **1998**, *70*, 341.
- (2) Gerrard, D. L.; Birnie, J. *Analytical Chemistry* **1990**, *62*, 140R.
- (3) Gerrard, D. L.; Bowley, H. J. *Analytical Chemistry* **1988**, *60*, 368R.
- (4) Mulvaney, S. P.; Keating, C. D. *Analytical Chemistry* **2000**, *72*, 145.
- (5) Raman, C. V.; Krishnan, K. S. *Indian J. Phys.* **1928**, *2*, 399.
- (6) Long, D. A. In *The Raman Effect*; John Wiley & Sons, Ltd: 2002, p 31.
- (7) Maier, S. A. *Plasmonics: Fundamentals and Applications*; Springer US: New York USA, 2007.

- (8) Gardiner, D. J. In *Practical Raman Spectroscopy*; Gardiner, D. J., Graves, P. R., Eds.; Springer Berlin Heidelberg: Berlin, Heidelberg, 1989, p 1.
- (9) Long, D. A. In *The Raman Effect*; John Wiley & Sons, Ltd: 2002, p 49.
- (10) Ingle, J. D.; Crouch, S. R. *Spectrochemical Analysis*; Prentice Hall, 1988.
- (11) Le Ru, E. C.; Etchegoin, P. G. In *Principles of Surface-Enhanced Raman Spectroscopy*; Ru, E. C. L., Etchegoin, P. G., Eds.; Elsevier: Amsterdam, 2009, p 121.
- (12) Brongersma, M. L.; Hartman, J. W.; Atwater, H. H. *MRS Online Proceedings Library* **1999**, 582.
- (13) Atwater, H. A. *Scientific American* **2007**, 296, 56.
- (14) Haynes, C. L.; Van Duyne, R. P. *The Journal of Physical Chemistry B* **2001**, 105, 5599.
- (15) Orendorff, C. J.; Gearheart, L.; Jana, N. R.; Murphy, C. J. *Physical Chemistry Chemical Physics* **2006**, 8, 165.
- (16) Chan, G. H.; Zhao, J.; Schatz, G. C.; Duyne, R. P. V. *The Journal of Physical Chemistry C* **2008**, 112, 13958.
- (17) Fraire, J. C.; Pérez, L. A.; Coronado, E. A. *The Journal of Physical Chemistry C* **2013**, 117, 23090.
- (18) Knight, M. W.; King, N. S.; Liu, L.; Everitt, H. O.; Nordlander, P.; Halas, N. J. *ACS Nano* **2014**, 8, 834.
- (19) McMahon, J. M.; Schatz, G. C.; Gray, S. K. *Physical Chemistry Chemical Physics* **2013**, 15, 5415.
- (20) Eustis, S.; El-Sayed, M. A. *Journal of Applied Physics* **2006**, 100, 044324.
- (21) Gans, R. *Annalen der Physik* **1915**, 352, 270.
- (22) Nanorods. nanocomposix.com (accessed 6/2/2016)
- (23) Wang, J.-F.; Li, H.-J.; Zhou, Z.-Y.; Li, X.-Y.; Liu, J.; Yang, H.-Y. *Chin. Phys. B* **2010**, 19, 117310/1.
- (24) Fleischmann, M.; Hendra, P. J.; McQuillan, A. J. *Chemical Physics Letters* **1974**, 26, 163.
- (25) Jeanmaire, D. L.; Van Duyne, R. P. *Journal of Electroanalytical Chemistry and Interfacial Electrochemistry* **1977**, 84, 1.
- (26) Albrecht, M. G.; Creighton, J. A. *Journal of the American Chemical Society* **1977**, 99, 5215.
- (27) Moskovits, M. *The Journal of Chemical Physics* **1978**, 69, 4159.
- (28) Moskovits, M. *Notes and Records of the Royal Society* **2012**, 66, 195.
- (29) Gersten, J.; Nitzan, A. *Journal of Chemical Physics* **1980**, 73, 3023.
- (30) Schatz, G. C. *Accounts of Chemical Research* **1984**, 17, 370.
- (31) Moskovits, M. *Reviews of Modern Physics* **1985**, 57, 783.
- (32) Moskovits, M. *Journal of Raman Spectroscopy* **2005**, 36, 485.
- (33) Kneipp, K.; Kneipp, H. *Applied Spectroscopy* **2006**, 60, 322A.
- (34) Le Ru, E. C.; Etchegoin, P. G. In *Principles of Surface-Enhanced Raman Spectroscopy*; Ru, E. C. L., Etchegoin, P. G., Eds.; Elsevier: Amsterdam, 2009, p 185.
- (35) Moskovits, M. *Physical Chemistry Chemical Physics* **2013**, 15, 5301.
- (36) Xu, H.; Aizpurua, J.; Käll, M.; Apell, P. *Physical Review E* **2000**, 62, 4318.
- (37) Doering, W. E.; Nie, S. *The Journal of Physical Chemistry B* **2002**, 106, 311.
- (38) Kelly, K. L.; Coronado, E.; Zhao, L. L.; Schatz, G. C. *The Journal of Physical Chemistry B* **2003**, 107, 668.

- (39) Lal, S.; Grady, N. K.; Goodrich, G. P.; Halas, N. J. *Nano Letters* **2006**, *6*, 2338.
- (40) Kneipp, K.; Moskovits, M.; Kneipp, H. *Surface-Enhanced Raman Scattering: Physics and Applications*; Springer Berlin Heidelberg, 2006.
- (41) Sharma, B.; Fernanda Cardinal, M.; Kleinman, S. L.; Greeneltch, N. G.; Frontiera, R. R.; Blaber, M. G.; Schatz, G. C.; Van Duyne, R. P. *MRS Bulletin* **2013**, *38*, 615.
- (42) Tanabe, K. *The Journal of Physical Chemistry C* **2008**, *112*, 15721.
- (43) Jha, S. K.; Ahmed, Z.; Agio, M.; Ekinici, Y.; Löffler, J. F. *Journal of the American Chemical Society* **2012**, *134*, 1966.
- (44) Le Ru, E. C.; Blackie, E.; Meyer, M.; Etchegoin, P. G. *The Journal of Physical Chemistry C* **2007**, *111*, 13794.
- (45) Guicheteau, J. A.; Farrell, M. E.; Christesen, S. D.; Fountain, A. W.; Pellegrino, P. M.; Emmons, E. D.; Tripathi, A.; Wilcox, P.; Emge, D. *Applied Spectroscopy* **2013**, *67*, 396.
- (46) Yuan, H.; Register, J.; Wang, H.-N.; Fales, A.; Liu, Y.; Vo-Dinh, T. *Analytical and Bioanalytical Chemistry* **2013**, *405*, 6165.
- (47) Auchinclove, C. A. R.; Richardson, P.; McGuinness, C.; Mallikarjun, V.; Donaldson, K.; McNab, H.; Campbell, C. J. *ACS Nano* **2012**, *6*, 888.
- (48) Sun, J.; Hankus, M. E.; Cullum, B. M. *Proc. SPIE* **2009**, 7313, 73130K0.
- (49) Rodriguez-Lorenzo, L.; Fabris, L.; Alvarez-Puebla, R. A. *Analytica Chimica Acta* **2012**, *745*, 10.
- (50) Sirimuthu, N. M. S.; Syme, C. D.; Cooper, J. M. *Proc. SPIE* **2012**, 8234, 82340F.
- (51) Liu, Y.; Ashton, J. R.; Moding, E. J.; Yuan, H.; Register, J. K.; Fales, A. M.; Choi, J.; Whitley, M. J.; Zhao, X.; Qi, Y.; Ma, Y.; Vaidyanathan, G.; Zalutsky, M. R.; Kirsch, D. G.; Badea, C. T.; Vo-Dinh, T. *Theranostics* **2015**, *5*, 946.
- (52) Yuen, J. M.; Shah, N. C.; Walsh, J. T.; Glucksberg, M. R.; Van Duyne, R. P. *Analytical Chemistry* **2010**, *82*, 8382.
- (53) Sharma, B.; Ma, K.; Glucksberg, M. R.; Van Duyne, R. P. *Journal of the American Chemical Society* **2013**, *135*, 17290.
- (54) Graham, D.; Thompson, D. G.; Smith, W. E.; Faulds, K. *Nature Nanotechnology* **2008**, *3*, 548.
- (55) Harper, M. M.; McKeating, K. S.; Faulds, K. *Physical Chemistry Chemical Physics* **2013**, *15*, 5312.
- (56) Ding, T.; Sigle, D. O.; Herrmann, L. O.; Wolverson, D.; Baumberg, J. J. *ACS Applied Materials & Interfaces* **2014**, *6*, 17358.
- (57) Hulteen, J. C.; Treichel, D. A.; Smith, M. T.; Duval, M. L.; Jensen, T. R.; Van Duyne, R. P. *The Journal of Physical Chemistry B* **1999**, *103*, 3854.
- (58) Masango, S. S.; Hackler, R. A.; Henry, A.-I.; McAnally, M. O.; Schatz, G. C.; Stair, P. C.; Van Duyne, R. P. *The Journal of Physical Chemistry C* **2016**, *120*, 3822.
- (59) Qi, D.; Yan, X.; Wang, L.; Zhang, J. *Chemical Communications* **2015**, *51*, 8813.
- (60) Pozzi, F.; Leona, M. *Journal of Raman Spectroscopy* **2016**, *47*, 67.
- (61) Muehlethaler, C.; Leona, M.; Lombardi, J. R. *Analytical Chemistry* **2016**, *88*, 152.
- (62) Smitha, S. L.; Gopchandran, K. G.; Ravindran, T. R.; Prasad, V. S. *Nanotechnology* **2011**, *22*, 265705.
- (63) Nie, S.; Emory, S. R. *Science* **1997**, *275*, 1102.
- (64) Kneipp, K.; Wang, Y.; Kneipp, H.; Perelman, L. T.; Itzkan, I.; Dasari, R. R.; Feld, M. S. *Physical Review Letters* **1997**, *78*, 1667.

- (65) Kneipp, K.; Kneipp, H.; Manoharan, R.; Hanlon, E. B.; Itzkan, I.; Dasari, R. R.; Feld, M. S. *Applied Spectroscopy* **1998**, *52*, 1493.
- (66) Hao, E.; Schatz, G. C. *The Journal of Chemical Physics* **2004**, *120*, 357.
- (67) Kneipp, K.; Haka, A. S.; Kneipp, H.; Badizadegan, K.; Yoshizawa, N.; Boone, C.; Shafer-Peltier, K. E.; Motz, J. T.; Dasari, R. R.; Feld, M. S. *Applied Spectroscopy* **2002**, *56*, 150.
- (68) Gunnarsson, L.; Bjerneld, E. J.; Xu, H.; Petronis, S.; Kasemo, B.; Käll, M. *Applied Physics Letters* **2001**, *78*, 802.
- (69) Van Duyne, R. P.; Hulteen, J. C.; Treichel, D. A. *Journal of Chemical Physics* **1993**, *99*, 2101.
- (70) Ibrahim, A.; Oldham, P. B.; Stokes, D. L.; Vo-Dinh, T. *Journal of Raman Spectroscopy* **1996**, *27*, 887.
- (71) Bao, L.; Mahurin, S. M.; Dai, S. *Analytical Chemistry* **2004**, *76*, 4531.
- (72) Vo-Dinh, T.; Hiromoto, M. Y. K.; Begun, G. M.; Moody, R. L. *Analytical Chemistry* **1984**, *56*, 1667.
- (73) McFarland, A. D.; Young, M. A.; Dieringer, J. A.; Van Duyne, R. P. *The Journal of Physical Chemistry B* **2005**, *109*, 11279.
- (74) Li, H.; Cullum, B. M. *Applied Spectroscopy* **2005**, *59*, 410.
- (75) Chaney, S. B.; Shanmukh, S.; Dluhy, R. A.; Zhao, Y. P. *Applied Physics Letters* **2005**, *87*, 031908/1.
- (76) Driskell, J. D.; Shanmukh, S.; Liu, Y.; Chaney, S. B.; Tang, X. J.; Zhao, Y. P.; Dluhy, R. A. *The Journal of Physical Chemistry C* **2008**, *112*, 895.
- (77) Hankus, M. E.; Li, H.; Gibson, G. J.; Cullum, B. M. *Analytical Chemistry* **2006**, *78*, 7535.
- (78) Greeneltch, N. G.; Blaber, M. G.; Henry, A.-I.; Schatz, G. C.; Van Duyne, R. P. *Analytical Chemistry* **2013**, *85*, 2297.
- (79) Khoury, C. G.; Vo-Dinh, T. *The Journal of Physical Chemistry C* **2008**, *112*, 18849.
- (80) Yuan, H.; Fales, A. M.; Khoury, C. G.; Liu, J.; Vo-Dinh, T. *Journal of Raman Spectroscopy* **2013**, *44*, 234.
- (81) Cullum, B. M.; Li, H.; Hankus, M. E.; Schiza, M. V. *NanoBiotechnology* **2007**, *3*, 1.
- (82) Gersten, J. I. *Journal of Chemical Physics* **1980**, *72*, 5779.
- (83) Sardar, R.; Shumaker-Parry, J. S. *Nano Letters* **2008**, *8*, 731.
- (84) Sardar, R.; Heap, T. B.; Shumaker-Parry, J. S. *Journal of the American Chemical Society* **2007**, *129*, 5356.
- (85) Qin, L.; Zou, S.; Xue, C.; Atkinson, A.; Schatz, G. C.; Mirkin, C. A. *Proceedings of the National Academy of Sciences* **2006**, *103*, 13300.
- (86) Osberg, K. D.; Rycenga, M.; Harris, N.; Schmucker, A. L.; Langille, M. R.; Schatz, G. C.; Mirkin, C. A. *Nano Letters* **2012**, *12*, 3828.
- (87) Pilo-Pais, M.; Watson, A.; Demers, S.; LaBean, T. H.; Finkelstein, G. *Nano Letters* **2014**, *14*, 2099.
- (88) Penn, M. A.; Drake, D. M.; Driskell, J. D. *Analytical Chemistry* **2013**, *85*, 8609.
- (89) Kim, N. H.; Lee, S. J.; Moskovits, M. *Nano Letters* **2010**, *10*, 4181.
- (90) Hu, M.; Ou, F. S.; Wu, W.; Naumov, I.; Li, X.; Bratkovsky, A. M.; Williams, R. S.; Li, Z. *Journal of the American Chemical Society* **2010**, *132*, 12820.
- (91) Ngo, H. T.; Wang, H.-N.; Fales, A. M.; Vo-Dinh, T. *Analytical Chemistry* **2013**, *85*, 6378.

- (92) Elghanian, R.; Storhoff, J. J.; Mucic, R. C.; Letsinger, R. L.; Mirkin, C. A. *Science* **1997**, *277*, 1078.
- (93) Kim, Y.; Johnson, R. C.; Hupp, J. T. *Nano Letters* **2001**, *1*, 165.
- (94) Pham, T.; Jackson, J. B.; Halas, N. J.; Lee, T. R. *Langmuir* **2002**, *18*, 4915.
- (95) Oldenburg, S. J.; Westcott, S. L.; Averitt, R. D.; Halas, N. J. *The Journal of Chemical Physics* **1999**, *111*, 4729.
- (96) Prodan, E.; Radloff, C.; Halas, N. J.; Nordlander, P. *Science* **2003**, *302*, 419.
- (97) Jackson, J. B.; Halas, N. J. *Proceedings of the National Academy of Sciences* **2004**, *101*, 17930.
- (98) Talley, C. E.; Jackson, J. B.; Oubre, C.; Grady, N. K.; Hollars, C. W.; Lane, S. M.; Huser, T. R.; Nordlander, P.; Halas, N. J. *Nano Letters* **2005**, *5*, 1569.
- (99) Zhang, X.; Zhao, J.; Whitney, A. V.; Elam, J. W.; Van Duyne, R. P. *Journal of the American Chemical Society* **2006**, *128*, 10304.
- (100) Roca, M.; Haes, A. J. *Journal of the American Chemical Society* **2008**, *130*, 14273.
- (101) Li, J. F.; Huang, Y. F.; Ding, Y.; Yang, Z. L.; Li, S. B.; Zhou, X. S.; Fan, F. R.; Zhang, W.; Zhou, Z. Y.; WuDe, Y.; Ren, B.; Wang, Z. L.; Tian, Z. Q. *Nature* **2010**, *464*, 392.
- (102) Lin, X.-D.; Li, J.-F.; Huang, Y.-F.; Tian, X.-D.; Uzayisenga, V.; Li, S.-B.; Ren, B.; Tian, Z.-Q. *Journal of Electroanalytical Chemistry* **2013**, *688*, 5.
- (103) Li, X.; Hu, H.; Li, D.; Shen, Z.; Xiong, Q.; Li, S.; Fan, H. J. *ACS Applied Materials & Interfaces* **2012**, *4*, 2180.
- (104) Zhao, Y.; Sun, L.; Xi, M.; Feng, Q.; Jiang, C.; Fong, H. *ACS Applied Materials & Interfaces* **2014**, *6*, 5759.
- (105) Li, H.; Patel, P. H.; Cullum, B. M. *Proc. SPIE* **2004**, 5588, 558887.
- (106) Li, H.; Baum, C. E.; Sun, J.; Cullum, B. M. *Proc. SPIE* **2006**, 6218, 6218041.
- (107) Li, H.; Baum, C. E.; Sun, J.; Cullum, B. M. *Applied Spectroscopy* **2006**, *60*, 1377.
- (108) Mubeen, S.; Zhang, S.; Kim, N.; Lee, S.; Krämer, S.; Xu, H.; Moskovits, M. *Nano Letters* **2012**, *12*, 2088.
- (109) Schultz, Z. D.; Wang, H.; Kwasnieski, D. T.; Marr, J. M. *Proc. SPIE* **2015**, 9554, 9554091.
- (110) Leverette, C. L.; Shubert, V. A.; Wade, T. L.; Varazo, K.; Dluhy, R. A. *The Journal of Physical Chemistry B* **2002**, *106*, 8747.
- (111) Im, H.; Bantz, K. C.; Lee, S. H.; Johnson, T. W.; Haynes, C. L.; Oh, S.-H. *Advanced Materials* **2013**, *25*, 2678.
- (112) Chae, J.; Lahiri, B.; Kohoutek, J.; Holland, G.; Lezec, H.; Centrone, A. *Optics Express* **2015**, *23*, 25912.
- (113) Culha, M.; Cullum, B.; Lavrik, N.; Klutse, C. K. *Journal of Nanotechnology* **2012**, *2012*, 15.

Chapter 2:

Layered Gold and Titanium Dioxide Substrates for Improved Surface Enhanced Raman Spectroscopic Sensing

2.1. Introduction

Surface enhanced Raman scattering (SERS) has been applied as a detection method in various sensing scenarios,^{1,2} exploiting the molecular recognition and multiplexability of Raman spectroscopy, while also taking advantage of the high sensitivity.³⁻⁵ To maximize SERS enhancement a large number of structures have been developed over the years to manipulate electric fields and surface plasmons.⁶⁻⁹ From the earliest demonstrations of single molecule detection via SERS,^{10,11} in which colloidal aggregates provided extreme SERS signal enhancements (10^{10} - 10^{14}) but low reproducibility,¹² to the development larger planar arrays^{9,13} with lower enhancement factors (10^5 - 10^8) but better reproducibility (i.e., RSD < 10%)¹⁴ the ability of SERS to chemically probe complex microenvironments has offered great promise for many applications. As the size of the sample environment continues to decrease, such as in single cell analyses and ultra-trace forensic detection applications,³⁻⁵ continued methods for improving the sensitivity of the SERS enhancement from reproducible structures (e.g., nanostars and nanoshells)¹⁵⁻¹⁷ is of critical importance.

Recently, novel multi-layered plasmonic nanostructures have been demonstrated to enhance native SERS signals associated with traditional silver SERS substrates,^{14,18,19} as well as the absorption experienced in silver-based, surface enhanced infrared absorption

(SEIRA) structures.²⁰ These multi-layered structures are fabricated by interleaving continuous silver films with thin dielectric spacer layers of silver oxide.¹⁴ The resulting substrates demonstrate enhanced SERS signals on their outermost surface by as much as 2.5-fold per silver oxide layer applied, with more than an order of magnitude improvement in SERS enhancement factors generated by applying multiple layers.¹⁴ The ultimate number of layers that can be applied for this enhancement is limited by the laser penetration depth as well as sample photo-stability, making it a powerful method to further enhance SERS substrates of various underlying structures.¹⁹ Using these initial silver multi-layered substrates, in which silver oxide spacer layers were generated by exposure to ambient air, a distinct optimal time for silver oxidation was found to exist (i.e., 50 hours).¹⁴ Improvements in SERS enhancement were observed with increasing exposure times up to 50 hr. At spacer layer growth times greater than 50 hours, a significant decrease in the signal was found with additional exposure, suggesting a distinct spacer layer thickness dependence.¹⁴

Due to the rapid degradation of silver-based SERS substrates resulting from surface oxidation, as well as issues associated with sample compatibility in many cases, the transfer of this multi-layer architecture to gold-based substrates would be ideal for many applications. Such multi-layer enhancements would allow the gap in sensitivity of gold-based substrates, relative to silver-based substrates, to be overcome or dramatically reduced.^{17,21} The development of multi-layered gold substrates has been explored as a mean to counteract the reduced enhancement associated with gold. The resulting multi-layer enhancement obtained was lower with respect to what was previously observed for multi-

layered silver substrates.¹⁸ In these previous attempts, the spacer layers were generated by physical vapor deposition (PVD) of silver island films followed by their complete oxidation to silver oxide islands to match the composition of silver multi-layer substrates previously employed.¹⁸ Although the resulting substrates showed an enhancement over comparable single layer substrates, their dual-layer enhancement (i.e., 1.4-fold/spacer layer) was significantly less than that achieved for dual-layered silver substrates (i.e., 2.7-fold/spacer layer), representing only a marginal improvement.^{14,18} This difference in multi-layer enhancement factors can be ascribed to the spacer layer fabrication technique employed. In the case of the dual-layered silver substrates, a continuous thin film of oxide could be grown across the entire surface of the underlying silver layer, whereas in the case of the gold/silver oxide island/gold dual-layered substrates, only discrete islands of the spacer could be generated. These discrete sites of spacer layer material reduced the multi-layered active surface area and thus the resulting multi-layer enhancement.

In this chapter, oxides deposited by atomic layer deposition (ALD) were used to fabricate dual- and multi-layered gold film over nanospheres (AuFON) SERS substrates capable of providing multi-layer enhancements comparable to those achieved only with silver multi-layered structures. The use of ALD for the deposition of TiO₂ spacers allowed for ultrathin films to be produced that can result in complete surface coverage with precisely controlled thicknesses. The self-limiting properties of this technique also allow for characterization of the dependence of the enhancement on spacer layer coverage and thickness. The advantages offered by these substrates, as well as the possibility of using wet chemistry methods for their fabrication was also explored.

2.2 Experimental

Chemicals

Mercaptobenzoic acid (Tokyo Chemical Industry), rhodamine 6G (Sigma), toluene (Baker), 2-mercaptoethanol (Sigma Aldrich) and ethyl alcohol (200 proof; Parmco-Aaper) were used as is, without further purification. Silica spheres (390 nm) were purchased from Bangs Laboratories as a 10% w/w suspension in water. Silver and gold shot (< 4 mm) used for physical vapor deposition were purchased from Kurt J. Lesker Company with a purity of 99.99%. The TiO₂ precursor for ALD, tetrakis (dimethylamido) titanium IV (TDMAT), was purchased from Sigma Aldrich.

Preparation of Metallic Film over Nanospheres Substrates

Gold film over nanostructure SERS substrates were generated in a process similar to that previously published.¹⁴ Glass microscope slides (VWR) were cut into uniform strips of 1×2.5 cm, cleaned in a RCA1 solution (1:1:5 NH₄OH: H₂O₂: H₂O) followed by a 1 N HCl solution, each for 1 hr. Subsequently, the strips were washed with distilled water several times prior to a final rinse in 200 proof ethanol and air drying in an oven at 60° C. The silica nanospheres for providing the underlying nanostructure of the film over nanostructure substrates were prepared from a 10% w/w stock suspension. This stock suspension was washed multiple times with deionized water and reconcentrated by centrifugation. The washed nanospheres were placed in neat ethanol and sonicated to generate the final 7% w/w suspension used for deposition on the microscope slide. 10 μL drops were then coated onto the microscope slide and the ethanol was allowed to evaporate, leaving a uniform layer of closely packed nanospheres. Deposition of gold films on these

nanosphere-coated slides was performed by mounting them on a rotating sample holder 15 cm above the tungsten boat in the vacuum evaporator (Explorer 14; Denton Vacuum). To ensure an even coating of gold was formed on the nanostructured substrate, the sample holder was slowly rotated during evaporation. The chamber was maintained at a pressure of 2×10^{-6} Torr and an evaporation rate of 1.0 \AA/s (monitored by a quartz crystal microbalance, XTM/2 film thickness monitor; Inficon) was employed during the entire deposition to obtain a high quality film. The reported thicknesses were determined using a calibration of the planar gold film thicknesses performed via profilometry. Figures 2.1a and 2.1b show atomic force (AFM) and scanning electron micrographs (SEM) of the substrates, respectively, demonstrating the close hexagonal packing of the spheres. The micrographs were taken with a Quanta 200 FEG (FEI) environmental SEM and a Dimension 3100 (Veeco) AFM. In the case of dual-layered structures, deposition of the second metallic film was performed following atomic layer deposition of the appropriate thickness of TiO_2 . The same procedure was used to fabricate silver film over nanospheres.

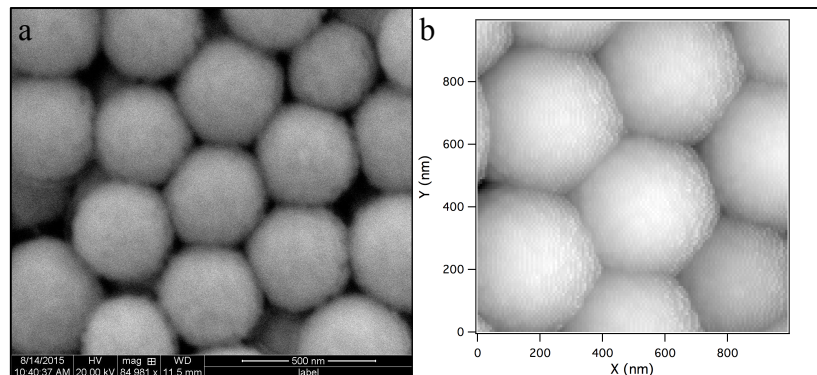


Figure 2.1. (a) Scanning electron micrograph and (b) atomic force micrograph revealing the hexagonally packed silica nanospheres and surface roughness of dual-AuFON substrates.

Spacer Layer Deposition

ALD:

The TiO₂ spacers were fabricated using a flow tube-based, hot-wall ALD reactor,²² by alternating exposure of the metallic surface to a vapor of the titanium precursor TDMAT and an oxidizer (H₂O) in a complementary, self-limiting manner. TiO₂ was deposited at a temperature of 100°C. Spacer layers of different nominal thicknesses were obtained by varying the number of deposition cycles employed from 1 to 32, corresponding to sub-monolayer films through multiple TiO₂ layers. The film thickness and growth rate per cycle were determined using spectroscopic ellipsometry on companion Si samples, revealing a linear growth versus number of cycles. The nominal film thicknesses reported are based on this linear growth rate and the specific number of cycles employed.

Surface Sol-Gel:

These TiO₂ spacers were fabricated using a previously developed technique.²³ In brief, the substrates were immersed in 2-mercaptoethanol (MET) for 2 min and rinsed with ethanol. The substrates were immersed for 8 min in a titanium(IV) butoxide in 1:1 toluene/methanol mixture, freshly daily prepared, and rinsed with ethanol. This procedure was followed by the immersion of the substrates in water for 1 min and rinsing with ethanol. To fabricate additional titania layers the same process was repeated with the exclusion of the MET coating step which is only required to activate the surface.

Surface Enhanced Raman Scattering Measurement System

SERS spectra were obtained using a laboratory built system (Figure 2.2). A 21 mW CW HeNe (632.8 nm) laser (JDS Uniphase) followed by a band-pass filter, to remove plasma emission lines, was used as the excitation source. This beam is reflected off of a silver mirror, to obtain the angle necessary for the backscattered setup, and then reflected by a holographic notch filter (Kaiser Optical Systems; super notch) onto a 10× objective (0.25 NA) which focuses the laser onto the SERS substrate surface. The resulting backscattered light is then collected and collimated by the same microscope objective before being filtered by two holographic notch filters to reject the elastically scattered light. The filtered signal is then focused with a lens (f/4) onto the slit of a 0.5 m spectrometer (Spectrapro 500i; Acton Research). The dispersed light is then detected with a liquid nitrogen cooled charged coupled device (Princeton Instruments). Slit widths on the spectrometer were set to provide a spectral resolution of 10 cm^{-1} . Control of the spectrometer and CCD was performed using WinSpec 32 acquisition software (Roper Scientific) and acquisition times of 500 ms with 9 accumulations were employed for all analyses unless otherwise specified. Data analysis was performed using Igor Pro 6.36A (WaveMetrics; see Macro A1 and A2 in Appendix A). SERS intensities reported represent the average of 18 measurements (3 substrates with 6 different random locations measured on each). Before each experiment a

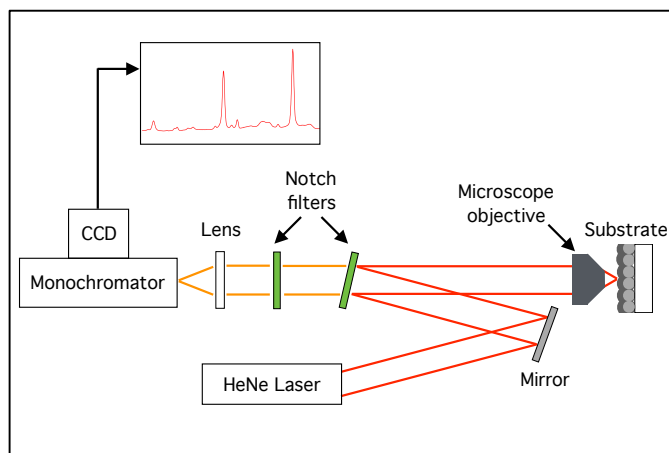


Figure 2.2. Schematic diagram depicting optical system used for the SERS measurements.

reference Raman spectrum of toluene was taken to calibrate the wavelength, as well as, to measure the background signal, which was subsequently subtracted.

Diffuse Reflectance Measurements System

Diffuse reflectance spectra were obtained using a laboratory built system (Figure 2.3). The system was used to measure the absorption profile of coated and uncoated SERS substrates and consisted in an Ocean Optics HR2000 spectrometer coupled to a mini deuterium halogen light source (DT-Mini-2-GS; Ocean Optics) and a fiber optic reflection probe

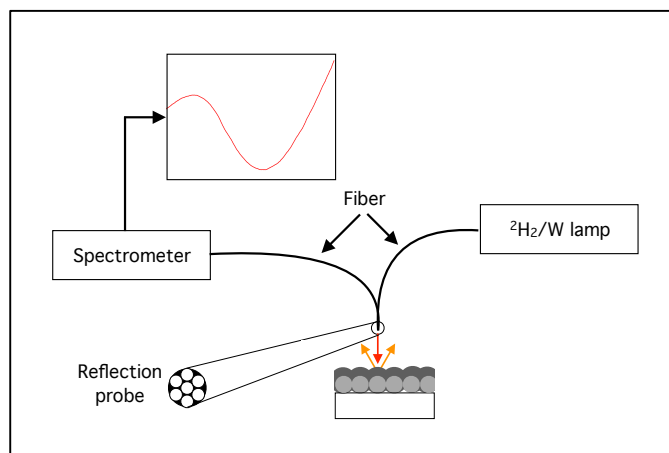


Figure 2.3. Schematic diagram depicting the system used for the diffuse reflectance measurements.

(R400-7-SR; Ocean Optics). The reflection probe operates in a six around one geometry, with six collection fibers around a single illumination fiber each of which is 400 μm in diameter. Data analysis was performed using Igor Pro 6.36A (WaveMetrics; see Macro A1 in Appendix A).

2.3 Results and Discussion

Due to its affinity to metallic surfaces, mercaptobenzoic acid was used as a reporter molecule to determine the characteristics of SERS substrates. To verify the origin of the observed peak intensities the MBA SERS spectrum was analyzed and its peaks assigned. The reported assignments were accomplished with a comparison of semi-empirical calculations compared to assignments of the SERS peaks reported in the literature.²⁴⁻²⁶

Figure 2.4 shows the spectrum of MBA chemisorbed on a silver film over nanospheres SERS substrate. The two major transitions at 1075 and 1588 rel. cm^{-1} (corresponding to c and g in Fig. 2.4) were assigned to asymmetric and symmetric ring breathing modes, respectively.^{24,25} The peak at 712 rel. cm^{-1} (a) was assigned to an out of plane vibration of

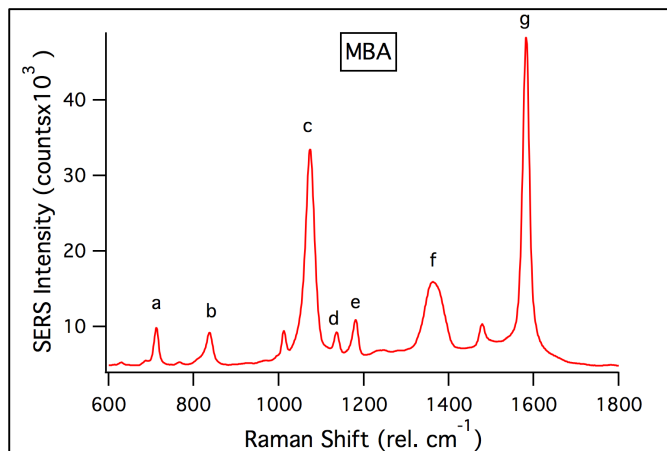


Figure 2.4. Spectrum of MBA chemisorbed on a SERS substrate with the identified peaks labeled (a-g).

the aromatic ring ($\gamma(\text{CCC})$).²⁴ The transition at 836 rel. cm^{-1} (b) was assigned to the in plane deformation of the carboxylic group ($\delta(\text{COO}^-)$).^{24,26} Transitions at 1137 and 1181 rel. cm^{-1} (corresponding to d and e) were assigned to the C-H bending modes of carbons in different positions on the ring ($\beta(\text{CH})$).²⁶ The broad peak at approximately 1363 rel. cm^{-1} (f) was assigned to the stretching of the carboxyl group and the broad profile ascribed to the different states in which the molecules are found on the surface of the substrate ($\nu(\text{COO}^-)$).^{24,27} To note that in the spectra reported in this chapter some of these features are not visible due to the lower enhancement offered by gold substrate and by the use of complete self-assembled monolayers of MBA, which geometrically reduce the signal relative to the vibrations of the carboxylic group. The peak at 1075 rel. cm^{-1} was used to compare the SERS intensities from the different substrates, even though the results observed were confirmed for other peaks identified as MBA.

Multi-layer Enhancement

In order to increase the limited active surface area associated with gold/silver oxide island/gold multi-layered substrates, ALD was employed in this work for the deposition of ultrathin, highly controlled dielectric spacer layers. Generating contiguous films of ultrathin dielectric between alternating layers of gold allows significant increases in the multi-layer enhanced active area have been achieved. To determine the optimal dielectric spacer layer thickness, a series of gold/TiO₂/gold dual-layered substrates were fabricated with varying thicknesses of TiO₂ deposited, ranging in nominal thickness from 0 to 2 nm. Titanium dioxide was chosen as the spacer material due to reports of its successful deposition on gold films via ALD and to its characteristic formation of coalescent films at

very low thicknesses.²⁸ To provide optimal surface plasmon resonance for SERS, as well as to allow for comparison to previous gold/silver oxide islands/gold multi-layered substrates gold thicknesses for each alternating layer were maintained at 65 nm. Using dual-layered substrates with 65 nm gold layers provides surface plasmon resonances in the range of 610 to 750 nm, with maxima ranging between 660 and 700 nm, ideal for excitation via HeNe laser. Extinction spectra of the substrates and SERS spectra of model chemical species were then obtained for each sample. For all spacer layer thicknesses employed no significant shift of the surface plasmon resonance was found. However, a clear optimal spacer layer thickness was observed for SERS enhancement. The effect of spacer layer thickness on the overall SERS enhancement for these dual-layered SERS substrates can be seen in Figure 2.5. To perform SERS measurements, the outer gold surface of each substrate was spotted with 10 μL of 10^{-3}M 4-mercapto-benzoic acid (MBA) solution in ethanol and measured in the SERS setup described previously. Typical SERS spectra obtained on single layer and dual-layered substrates of 10^{-3}M MBA can be seen in Figure 3a. From these spectra, significant enhancement in SERS signal for all of the major bands can be observed for the dual-layered substrates.

Figure 2.5b reports the SERS intensity of the MBA band at 1075 rel. cm^{-1} for the substrates as a function of the nominal thickness of the TiO_2 spacer. Each data point corresponds to the average of 12 measurements taken in different locations of 3 different substrates fabricated in the same batch. The error bars correspond to the standard deviation of these averages. As can be seen from Figure 2.5b a significant increase in SERS signal from $(8.5\pm 0.5)\times 10^3$ to $(19\pm 2)\times 10^3$ counts is observed for spacer layer thicknesses ranging

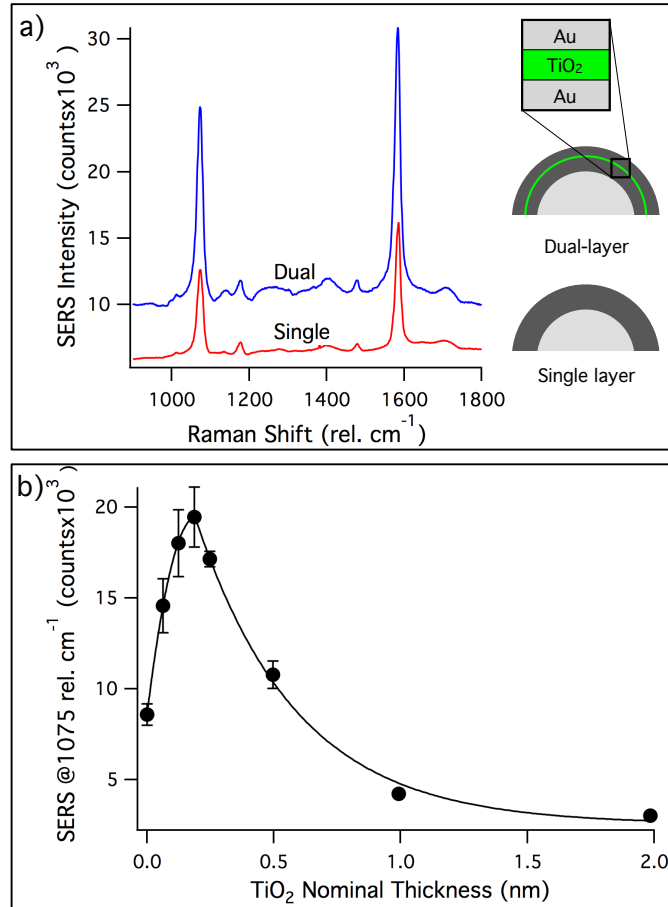


Figure 2.5. (a) Spectra of MBA chemisorbed on a dual-layered substrate with two 125 nm gold layers separated by a 0.19 nm TiO_2 spacer layer (Single) and on a single layer substrate with 250 nm of gold (Dual). Inset shows a schematic representation of the two substrates. **(b)** Effect of TiO_2 nominal spacer layer thickness on the intensity of the 1075 rel. cm^{-1} band of MBA for dual-layer gold substrates.

between nominal thicknesses, as measured by ellipsometry, of 0 to 0.19 nm. For thicknesses ranging from 0.19 to 1.98 nm a dramatic decrease in SERS enhancement is observed. This non-monotonic relationship between spacer layer thickness and SERS enhancement is similar to that observed for silver/silver oxide/silver substrates although the optimal SERS enhancement occurs at a different nominal spacer layer thickness. The corresponding dual-layer enhancement, the ratio of the optimal dual-layer SERS signal to the corresponding single layer SERS intensity (i.e., spacer layer thickness of 0 nm), was found to be 2.3-fold. This multi-layer enhancement is significantly greater than the 1.4-

fold dual-layer enhancement previously achieved in gold/silver oxide island/gold substrates and is comparable to the optimal dual-layer enhancement observed for silver/silver oxide/silver substrates.

Spacer Layer Thickness Dependence

To better understand the source of the non-monotonic relationship between the multi-layer enhancement and the spacer layer thickness for these (and previous silver/silver oxide/silver) substrates, surface coverage studies of the spacer layer on the underlying gold were performed. In these studies, single layered gold substrates each coated with a different number of TiO₂ deposition cycles via ALD, corresponding to different surface coverage, were incubated in a 10⁻³M solution of the reporter thiol molecule (MBA) for 5 minutes. The substrates were then washed thoroughly with ethanol to remove unbound MBA so that only molecules chemisorbed on the gold surface were left behind on the substrates. The SERS signals from these substrates were measured and used to estimate the surface coverage of the TiO₂ spacer on the gold surface. A schematic cartoon demonstrating the inverse relationship between TiO₂ coverage and amount of MBA chemisorbed to the gold is shown in Figure 2.6a, revealing how by increasing the number of ALD cycles (i.e., the nominal thickness of TiO₂) the gold surface area exposed for chemisorption of MBA decreases concomitantly with the increase in TiO₂ surface coverage.

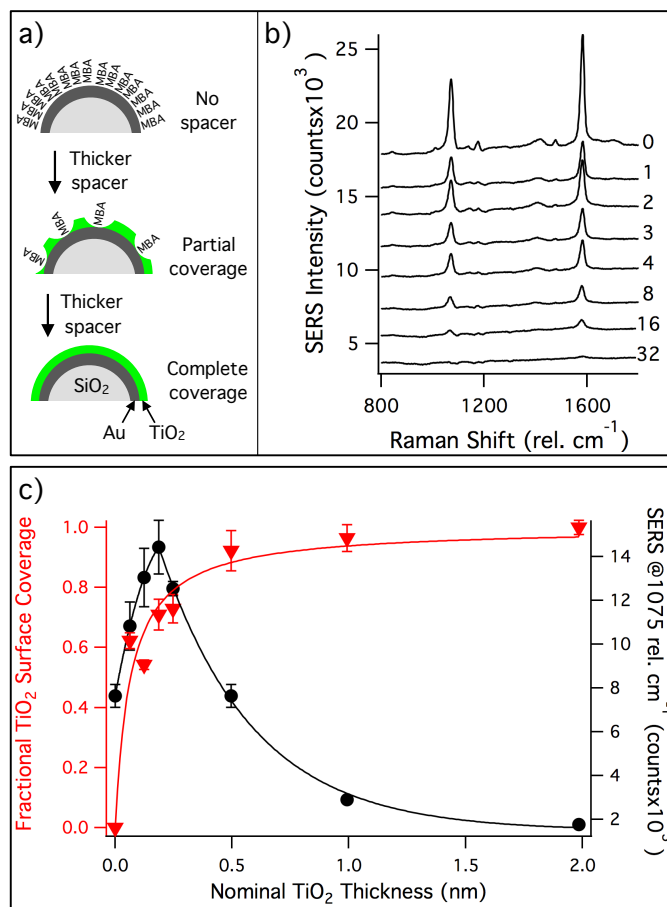


Figure 2.6. (a) Schematic diagram depicting the inverse relationship between TiO₂ surface coverage and the number of MBA molecules that can chemisorb to the gold for surface coverage studies. (b) SERS spectra of MBA on gold substrates following increasing numbers of ALD cycles (0 – 32) for TiO₂ deposition. (c) Surface coverage of TiO₂ on gold substrates as a function of nominal TiO₂ thickness (red triangles). The error bars represent to the 99% confidence limit and the red curve shows the fit of the data with a Langmuir-like function to describe the saturation behavior observed. Overlaid is the plot is the relative dual layer SERS intensity of the 1075 rel. cm⁻¹ band of MBA (right axis) as a function of nominal TiO₂ spacer layer thickness (black circles and black trend line).

Typical SERS spectra of MBA from these studies can be seen in Figure 2.6b for spacer layers ranging from 0 to 32 cycles with each cycle corresponding to a nominal thickness increase of 0.06 nm. Each spectrum corresponds to the average of 6 measurements taken in different locations on a substrate. As expected, the signal from the SERS active bands associated with MBA decrease with the increased number of ALD cycles, up to 32 cycles. After 32 cycles SERS active bands from MBA are no longer observed. This behavior is

due to the loss of the exposed gold surface area available for MBA chemisorption as the amount of TiO₂ deposited increases. The SERS intensities of the 1075 rel. cm⁻¹ band of MBA from these spectra were then used to obtain surface coverage estimates for the different number of ALD cycles employed. Prior to measuring the peak intensity of the 1075 rel. cm⁻¹ band, each spectrum was background corrected. The correction was performed by subtracting the baseline from the spectrum of 32 ALD cycles from each. This spectrum had no distinguishable SERS bands associated with MBA. At 32 cycles or more, ALD films of TiO₂ using TDMAT and H₂O are known to completely cover the surface on which they are deposited. The estimated fraction of surface coverage was then calculated with Equation 2.1.

$$SC(x) = 1 - \frac{I(x)}{I(0)} \quad (2.1)$$

where $SC(x)$ is the surface coverage of the spacer deposited for x ALD cycles, $I(x)$ represents the baseline-corrected intensity for a substrate coated with an x number of ALD cycles and $I(0)$ is the intensity of the baseline-corrected intensity for a MBA coated substrate with no TiO₂ (0 ALD cycles).

In Figure 2.6c, the triangles and corresponding fit (solid line) show the fraction of the gold surface covered by TiO₂ as a function of nominal surface coverage (as estimated by ellipsometry). Each data point (triangles) represents the average of six measurements and the error bars correspond to the 99% confidence interval associated with these values as propagated from the initial SERS signals. As can be seen from these results, surface coverages of approximately 100% are achieved at thicknesses of 0.22 nm or greater, which corresponds to the thickness of a monolayer of TiO₂.²⁹ For the first 4 cycles, corresponding

to nominal thicknesses from 0 to 0.25 nm, the surface coverage rapidly increases before plateauing at thicknesses of 0.25 nm or greater. This plateau can be seen in Figure 2.6c as well with 8, 16 and 32 cycles providing the statistically identical surface coverage values of $92\pm 7\%$, $96\pm 4\%$ and $99\pm 2\%$, respectively. When this surface coverage relationship is correlated to the SERS multi-layer enhancement trend as a function of nominal thickness of the spacer it suggests a relationship between spacer layer coverage of the underlayer and optimal SERS enhancement performance. The multi-layer SERS enhancement (i.e., SERS intensity) increases with increases in surface coverage for the first several cycles, reaching a maximum at the thickness corresponding to a monolayer, where complete surface coverage of the underlying gold layer in dual-layer SERS substrates is achieved. This behavior is ascribed to an increase in the dual-layer active enhancement area experienced with an increase in surface coverage of the spacer on the underlying gold surface, thereby preventing direct contact between the two gold films. The exponential decrease in SERS enhancement observed at nominal TiO_2 thicknesses corresponding to more than a monolayer of dielectric spacer material is due to a decreased electronic interaction between proximal gold layers. This observation is in agreement with previous hypotheses on the mechanism of action for dual and multi-layered substrates, in which separate plasmons are produced in each isolated metal layer and reinforce each other providing a greater electromagnetic field at the substrates outer surface.¹⁴

Enhanced Shelf Life

In addition to providing greater SERS signals than comparable single layered substrates, with over an order of magnitude improvement possible by applying multiple layers, the use

of gold instead of silver also results in greater sample compatibility for certain applications (e.g., biological analyses), as well as improved shelf life and long term stability.¹⁷ To evaluate the long-term stability of these dual-layered AuFON SERS substrates, their SERS response was monitored for a period of months following the fabrication of a batch of comparable substrates. These substrates were composed of two 125 nm thick gold films separated by a TiO₂ spacer of 0.19 nm (i.e., 3 ALD cycles), corresponding to the optimal geometry determined previously. After fabrication, the substrates remained in ambient conditions and were analyzed over a period of greater than 5 months. Prior to the measurement of each substrate, the substrates were spotted with 10 μ L of a 10⁻³M MBA solution. The results from this study can be seen in Figure 2.7 as the black circles and associated trend line, which shows the relative intensities of the MBA band at 1075 rel. cm⁻¹ normalized respect to the initial value for a freshly prepared substrate. Each data point represents the average of 6 measurements from different locations on a single dual-layered substrate. Only a single substrate was employed for each time point in this study to ensure that the substrates produced from a single batch could cover a sufficient time period. As can be seen from these results, only a slight decrease in SERS intensity is observed over time. After a period of 2 weeks exposure to ambient conditions, greater than 80% SERS enhancement continues to be observed. Although this increased stability is directly attributable to the relatively inert properties of the gold surface, and not the dual-layer architecture, the dual- or multi-layered structure results in a improved initial SERS enhancement factor (i.e., signal intensity) allowing them to provide useful results for a longer period of time than comparable single layered substrates. This can be seen from the dashed black line in Figure 2.7, which shows the relative SERS signal intensity from a

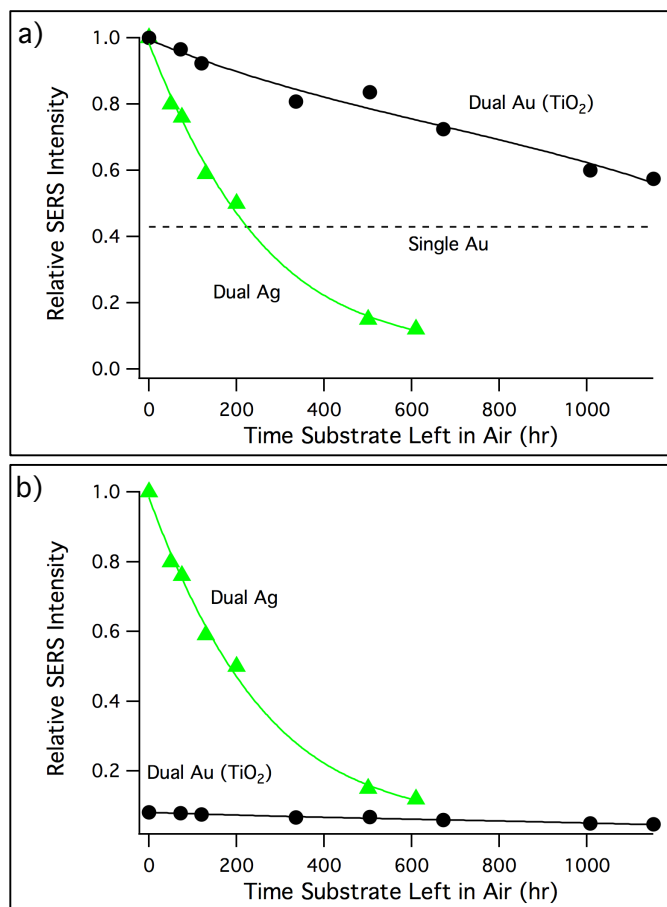


Figure 2.7. (a) Relative SERS intensities of the 1075 rel. cm⁻¹ band of MBA on gold dual-layered substrates (black circles and black trend line curve) and silver dual-layered substrates (green triangles and green trend line curve) exposed to air under ambient conditions for different periods of time. Trend lines have been added to each of these sets of data to aid in visualization of the trends. Straight dashed black line represents the relative SERS intensity of the 1075 rel. cm⁻¹ band of MBA on comparable single layered gold substrates (Single Au). **(b)** Relative SERS intensity of silver and gold multilayer substrates normalized with respect to the absolute signal of a newly made silver/silver oxide/silver SERS structure.

freshly made, single layer gold substrate (i.e., total gold thickness of 250 nm) with the same 10 μ L of 10⁻³ M MBA solution applied prior to analysis. Even after a period of 48 days, the dual-layered gold substrate provided greater SERS enhancement than the single layer gold substrate (i.e., 36% greater), retaining 57% of the original SERS signal intensity obtained from a fresh dual-layered gold substrate. Although the rate at which the SERS signals decrease over time with exposure to ambient conditions is the same for both the

single layer and dual-layered gold substrates, the ability to apply two or more layers of gold and increase the initial SERS enhancement results in substrates with longer shelf lives. This phenomenon is similar to what has been observed for multi-layered silver substrates compared to single layer silver substrates.¹⁴ The enhanced shelf life for the dual- and multi-layered gold SERS substrates is even more pronounced when compared to optimized dual-layer silver substrates with silver oxide spacer layers (shown as triangles with trend line in Figure 2.7). In the case of the dual-layered silver substrates, silver oxide has been found to be the optimal spacer material, providing signal enhancements of 2.7-fold per additional layer of silver and it was used for comparison.¹⁴ The comparison of the gold/TiO₂/gold results with silver/silver oxide/silver clarifies the shelf life advantages offered by the use of gold in these structures. Even though the silver-based dual-layered substrates provide increased shelf life with respect to their single layer silver counterparts, as a consequence of increased signal, their overall SERS response dropped to approximately 50% within one week of fabrication, whereas the dual-layered gold substrates last almost two months prior to degrading to 50% of their original enhancement.

This difference in decay rate and the longer shelf life of the gold-based substrates, compared to the silver multi-layer substrates, can also be seen in Figure 2.7b, in which the relative SERS intensities of dual-layer gold with optimized TiO₂ spacer and dual-layer silver with optimized silver oxide spacer have both been normalized to the SERS intensity of an optimized dual-layer silver substrate immediately following fabrication. As expected initially the silver dual-layer structure outperforms (12-fold larger signal) the optimized dual-layer gold substrates due to the inherent plasmonic characteristics of the two

materials. Because of the rapid degradation of the silver SERS substrates due to surface oxidation, the dual-layered gold substrates begin to exhibit comparable SERS response after only 600 hr (i.e., 25 days) of storage in ambient conditions. After 600 hr, the gold substrates exhibit greater SERS enhancements than silver, suggesting that gold multilayered structures not only offer a means of obtaining a more bio-compatible enhanced SERS substrate but also perform better than silver substrates in cases where long storage times before analysis are necessary.

In addition to gold substrates providing an inherently longer shelf life than comparable silver-based substrates, the electro-active nature of the gold surface also allows for further extension of their useful lifetime through electrochemical regeneration of the gold surface to remove environmental contaminants. Demonstration of the electrochemical regeneration of these dual-layered gold substrates was performed using dual-layer gold substrates (two 125 nm thick gold layers separated by a 0.19 nm thick TiO₂ spacer layer) that have been exposed to 10 μ L of a 3×10^{-3} M solution of MBA and left in ambient conditions for a period of 158 days. The resulting SERS spectra were then measured and a representative spectrum is shown in Figure 2.8 (bottom spectrum). Several SERS active bands can be seen in this spectrum, with the band at 1075 rel. cm^{-1} corresponding to MBA. In addition, the second prominent SERS active MBA band at 1588 rel. cm^{-1} is also present but is convoluted with background SERS signals at 1592 rel. cm^{-1} . The SERS signal decreased over the 158 days since fabrication and that the adsorption of a number of environmental contaminants has occurred, resulting in a significantly convoluted background. Based on the 1075 rel. cm^{-1} band, the SERS signal from MBA had degraded to 11% of the intensity when measured on

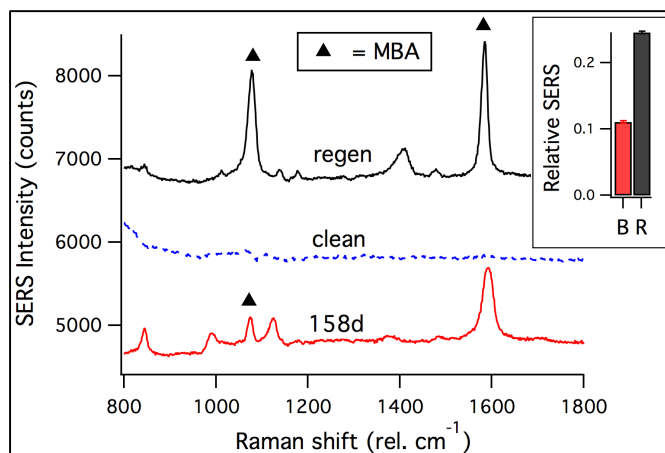


Figure 2.8. SERS spectra for a 158-day old substrate exposed to MBA, prior to the electrochemical regeneration (solid black line; 158d), after electrochemical cleaning (dashed blue line; clean) and after being regenerated and exposed to MBA again (solid red line; regen). Spectra have been offset for visualization. * - denotes MBA specific SERS bands. Inset shows the relative intensities of the MBA peak at 1075 rel. cm^{-1} for the substrate before (B) and after regeneration (R).

a fresh dual-layer substrate. Following the SERS measurement, after 158 days exposure to ambient conditions, the substrate was electrochemically regenerated by placing it in a 0.1M NaOH solution while performing cyclic voltammetry (CV). The CV was scanned from 0 to -1.4 V at 0.1 V/s, followed by maintaining a constant potential of -1.4 V for 120 seconds to remove any adsorbed species present, including MBA. From the initial CV scan, a prominent peak at -0.3 V was found. Following the 120 second reduction period at -1.4 V, a second CV scan was performed to ensure all of the adsorbed species had been removed. Following this electrochemical treatment, SERS spectra of the cleaned substrate were measured with a typical spectrum shown as the dashed line in Figure 2.8 (spectrum has been offset for visualization purposes). As can be seen from this spectrum, all prominent SERS active bands have disappeared following this cleaning process with only a small amount of residual broadband background present near 800 cm^{-1} . Immediately following SERS analysis of the cleaned substrate, $10 \mu\text{l}$ of a 10^{-3} M MBA solution was placed on the substrate surface and another SERS spectrum was obtained with the same acquisition

parameters (shown as the upper spectrum in Figure 2.8). From this spectrum, the two prominent MBA bands at 1075 rel. cm^{-1} and 1588 rel. cm^{-1} can be seen and with greater intensity than before cleaning. The SERS signal from the 158 day old recovered substrate increased more than 2-fold (as calculated based on the 1075 rel. cm^{-1} band of MBA) to 25% of the SERS intensity measured on a fresh dual-layer substrate. The inset in Figure 2.8 shows the relative SERS signal from the 1075 rel. cm^{-1} band of MBA normalized to the signal from a newly generated dual-layer gold substrate both before (labeled “B”) and after regeneration (labeled “R”), revealing this approximately two-fold improvement in performance even after more than five months of exposure to ambient conditions. The electrochemical regeneration did not completely restore the original sensitivity of the SERS substrate, likely due to the instability of nanoscopic features on the outer surface over time.³⁰ However, this technique was demonstrated to remove the SERS background associated with environmental contaminants chemisorbed to the surface as well as oxides that have slowly formed over time.

Surface sol-gel spacers

Although ALD is an ideal solution to fabricate model systems due its precision, the scalability of this technique could present challenges. Alternatively, wet chemistry techniques can be employed to fabricate effective oxide films, for example, with surface sol-gel.^{23,31} To explore the capabilities of wet chemistry in fabricating ultrathin oxide films

on metallic surfaces, the surface sol-gel technique was used to grow TiO_2 films. The resulting substrates were characterized to determine the cyclical growth of the films.

Figure 2.9 shows the normalized SERS intensity from substrates coated with different number of cycles of surface sol-gel. The intensities were calculated from the peak at $1363 \text{ rel. cm}^{-1}$ of rhodamine 6g (R6G) adsorbed on the surface of the substrate and normalized for the uncoated substrate (0 surface sol-gel cycles). R6G was used in place of MBA to avoid preferential binding to the metallic surface. The abscissa in the graph represent the thickness of the TiO_2 coating calculated from growth rates (in thickness/cycle) previously reported.²³

As it can be observed from Figure 2.9 the intensities decay exponentially as a function of TiO_2 coating thickness. This result was expected and is ascribed to the exponential dependence that SERS signals have with respect to distance from a metallic surface.^{5,23} R6G, the molecule responsible for the measured signal, is progressively distanced from the

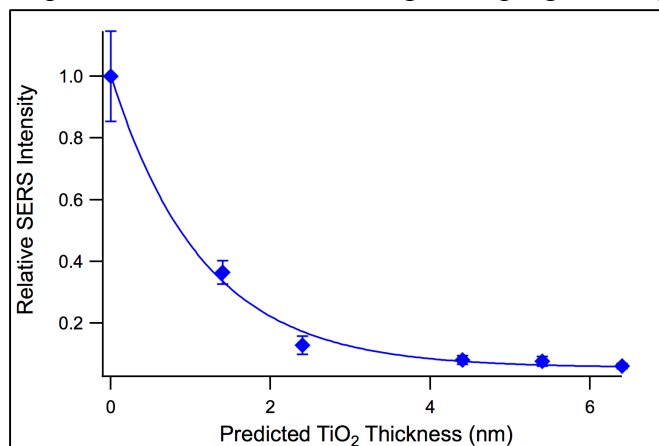


Figure 2.9. SERS intensities from the $1363 \text{ rel. cm}^{-1}$ peak of R6G adsorbed on substrates coated with different thicknesses of TiO_2 . The coating layer was fabricated with surface sol-gel. The number of cycles of synthesis was changed to vary the thickness of TiO_2 , the thicknesses were extrapolated from the known growth rate.

surface by the TiO₂ coating. The distance at which the decay reaches its minimum is consistent with what is currently considered the maximum distance at which a SERS enhancement can be obtained (i.e., ≈ 5 nm).⁵ These observations demonstrate the possibility of fabricating TiO₂ spacers for multi-layered structures using a simple synthesis procedure (surface sol-gel), and that the spacer thickness can be controlled by varying the number of cycles used.

The increase in thickness of the TiO₂ spacer as a function of increasing number of synthesis cycles was also observed by looking at the shift in surface plasmon resonance of the substrates. Figure 2.10 shows the reflectance spectra of substrates coated with increasing thicknesses of TiO₂ (i.e., 0, 2.4, 4.4 and 6.4 nm for a, b, c and d, respectively). As expected the increase in the number of cycles caused a red shift in the surface plasmon of the substrates due to change in refractive index at the metal/dielectric interface.³² To validate the predicted thickness of the spacers, the red shift spectra were compared to what observed in ALD-coated substrate. Although the shifts had similar slopes, the thickness from the

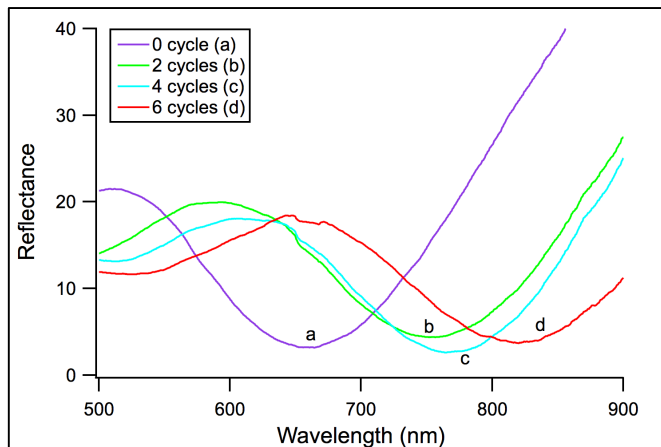


Figure 2.10. Reflectance spectra of substrates coated with varying thicknesses of TiO₂, fabricated via surface sol-gel. The number of cycles of surface sol-gel control the thickness of the TiO₂ coating.

resonances observed in the ALD experiments differ from the predicted thickness. The disagreement was ascribed to the presence of MET on the metallic surface and to different densities of TiO₂. From these results it was concluded that surface sol-gel was able to coat the substrate surface with progressively increasing thicknesses as a function of cycles. Additional characterization of the thickness and optimization of the quality of the TiO₂ spacer via post-process treatments are required for the fabrication of spacers for multi-layered structures via wet chemistry.

2.4 Conclusions

This paper demonstrates the ability to fabricate dual and multi-layer gold substrates with multi-layer enhancements (i.e., ~ 2.3-fold/additional metal layer) comparable to those previously only observed in silver multi-layered substrates (i.e., 2.7-fold/additional metal layer). Correlation of the maximum SERS enhancement achieved to the surface coverage of the underlying gold layer by TiO₂ has revealed the critical importance of complete separation of the gold layers for maximum SERS enhancement. Using ALD, the generation of controlled ultrathin spacer layers allows this optimal surface coverage while minimizing the overall spacer layer thickness, thereby providing an ideal method for dual and multi-layer gold SERS substrates. The long-term shelf life of these gold dual-layer substrates was also demonstrated, revealing their ability to retain SERS for more than 48 days and provide useful SERS signals for months after fabrication even when exposed to ambient conditions. The ability to electrochemically regenerate these substrates after 5 months of exposure to ambient conditions and increase the SERS signal by 200% has also been shown. Finally,

the fabrication of TiO₂ spacer via surface sol-gel was investigated to fabricate multi-layered structures with scalable processes.

2.5 References

- (1) Sharma, B.; Frontiera, R. R.; Henry, A.-I.; Ringe, E.; Van Duyne, R. P. *Materials Today* **2012**, *15*, 16.
- (2) Harper, M. M.; McKeating, K. S.; Faulds, K. *Physical Chemistry Chemical Physics* **2013**, *15*, 5312.
- (3) Moskovits, M. *Journal of Raman Spectroscopy* **2005**, *36*, 485.
- (4) Xu, H.; Aizpurua, J.; Käll, M.; Apell, P. *Physical Review E* **2000**, *62*, 4318.
- (5) Strobbia, P.; Languirand, E.; Cullum, B. M. *Optical Engineering* **2015**, *54*, 100902.
- (6) Vo-Dinh, T.; Hiromoto, M. Y. K.; Begun, G. M.; Moody, R. L. *Analytical Chemistry* **1984**, *56*, 1667.
- (7) Gunnarsson, L.; Bjerneld, E. J.; Xu, H.; Petronis, S.; Kasemo, B.; Käll, M. *Applied Physics Letters* **2001**, *78*, 802.
- (8) Haynes, C. L.; Van Duyne, R. P. *The Journal of Physical Chemistry B* **2001**, *105*, 5599.
- (9) Driskell, J. D.; Shanmukh, S.; Liu, Y.; Chaney, S. B.; Tang, X. J.; Zhao, Y. P.; Dluhy, R. A. *The Journal of Physical Chemistry C* **2008**, *112*, 895.
- (10) Kneipp, K.; Wang, Y.; Kneipp, H.; Perelman, L. T.; Itzkan, I.; Dasari, R. R.; Feld, M. S. *Physical Review Letters* **1997**, *78*, 1667.
- (11) Nie, S.; Emory, S. R. *Science* **1997**, *275*, 1102.
- (12) Kneipp, K.; Haka, A. S.; Kneipp, H.; Badizadegan, K.; Yoshizawa, N.; Boone, C.; Shafer-Peltier, K. E.; Motz, J. T.; Dasari, R. R.; Feld, M. S. *Applied Spectroscopy* **2002**, *56*, 150.
- (13) Van Duyne, R. P.; Hulteen, J. C.; Treichel, D. A. *Journal of Chemical Physics* **1993**, *99*, 2101.
- (14) Li, H.; Cullum, B. M. *Applied Spectroscopy* **2005**, *59*, 410.
- (15) Talley, C. E.; Jackson, J. B.; Oubre, C.; Grady, N. K.; Hollars, C. W.; Lane, S. M.; Huser, T. R.; Nordlander, P.; Halas, N. J. *Nano Letters* **2005**, *5*, 1569.
- (16) Khoury, C. G.; Vo-Dinh, T. *The Journal of Physical Chemistry C* **2008**, *112*, 18849.
- (17) Yuan, H.; Fales, A. M.; Khoury, C. G.; Liu, J.; Vo-Dinh, T. *Journal of Raman Spectroscopy* **2013**, *44*, 234.
- (18) Li, H.; Baum, C. E.; Sun, J.; Cullum, B. M. *Applied Spectroscopy* **2006**, *60*, 1377.
- (19) Cullum, B. M.; Li, H.; Hankus, M. E.; Schiza, M. V. *NanoBiotechnology* **2007**, *3*, 1.
- (20) Chae, J.; Lahiri, B.; Kohoutek, J.; Holland, G.; Lezec, H.; Centrone, A. *Optics Express* **2015**, *23*, 25912.
- (21) Orendorff, C. J.; Gearheart, L.; Jana, N. R.; Murphy, C. J. *Physical Chemistry Chemical Physics* **2006**, *8*, 165.
- (22) Hackley, J. C.; Gougousi, T.; Demaree, J. D. *Journal of Applied Physics* **2007**, *102*, 034101.
- (23) Bao, L.; Mahurin, S. M.; Dai, S. *Analytical Chemistry* **2004**, *76*, 4531.
- (24) Michota, A.; Bukowska, J. *Journal of Raman Spectroscopy* **2003**, *34*, 21.

- (25) Orendorff, C. J.; Gole, A.; Sau, T. K.; Murphy, C. J. *Analytical Chemistry* **2005**, *77*, 3261.
- (26) Marks, H. L.; Pishko, M. V.; Jackson, G. W.; Coté, G. L. *Analytical Chemistry* **2014**, *86*, 11614.
- (27) Jamieson, L. E.; Jaworska, A.; Jiang, J.; Baranska, M.; Harrison, D. J.; Campbell, C. J. *Analyst* **2015**, *140*, 2330.
- (28) Biener, M. M.; Biener, J.; Wichmann, A.; Wittstock, A.; Baumann, T. F.; Bäumer, M.; Hamza, A. V. *Nano Letters* **2011**, *11*, 3085.
- (29) Ferguson, J. D.; Yoder, A. R.; Weimer, A. W.; George, S. M. *Applied Surface Science* **2004**, *226*, 393.
- (30) Dick, L. A.; McFarland, A. D.; Haynes, C. L.; Van Duyne, R. P. *The Journal of Physical Chemistry B* **2002**, *106*, 853.
- (31) Ichinose, I.; Senzu, H.; Kunitake, T. *Chemistry of Materials* **1997**, *9*, 1296.
- (32) Maier, S. A. *Plasmonics: Fundamentals and Applications*; Springer US: New York USA, 2007.

Chapter 3:

Dielectric Spacer Dependence of Multi-Layered Structures for Enhanced SERS Sensing

3.1 Introduction

Surface enhanced Raman spectroscopy (SERS) is a powerful analytical technique due to its ability to give intrinsic molecule-specific information, which results from the combination of Raman spectroscopy and nanophotonics.¹⁻⁴ In fact, although the vibrational nature of Raman spectra yields chemical information, the inherently low Raman signal has limited its utilization in real-world sensing scenarios. SERS exploits the scattering characteristics of metallic nanoparticles or nanostructures to amplify the intensity of Raman scattering by 6 - 11 orders of magnitude.^{3,5,6} The development of SERS substrates and probes, aided by the rapid development of nanotechnology, has allowed the emergence of numerous sensing platform based on this technique, which can be found in many reviews.⁷⁻¹¹

Although SERS substrates have achieved limits of detection up to a single molecule, the reproducibility of the generated SERS enhancement often limits their applicability.^{12,13} Single molecule SERS was first obtained with colloidal aggregates, in which nanometric gaps between metallic nanoparticles were responsible for generating the observed SERS enhancement.^{14,15} However, due to the randomness associated with the aggregation process, these substrates cannot be used for quantitative intrinsic SERS sensing and have

to rely on additional transduction mechanisms to detect a target, partially defeating the main advantage of this technique.^{7,16,17} To obtain large enhancement factors while conserving reproducibility, alternative structures based on organized arrays and single particles have been developed.¹⁸⁻²¹ Although these strategies yield reproducible substrates, the enhancement factors obtained are small compared to that of aggregates.⁷

Multi-layered structures were developed in our lab as a mean to further amplify the enhancement of a SERS substrate independently of the underlying structure.²²⁻²⁷ These structures are based on alternating layers of thin metallic films and ultrathin dielectric spacers.^{23,25} The additive property of this geometry arises from amplifying the SERS enhancement via interaction between layers happening in the volume of the substrate, rather than on its surface alone, therefore conserving the substrate surface characteristics. In addition, this multi-layer enhancement was observed to increase as the number of metallic layers applied and was seen to also work in surface enhanced IR absorption (SEIRA) substrates.^{23,28} This enhancing strategy permits amplification of the SERS enhancement of a previously developed sensing platform to obtain the desired sensitivity.

A complete mechanism for the multi-layer enhancement has not been demonstrated yet, however, this phenomenon is currently believed to be due to the interaction between surface plasmons excited on proximal metallic films.^{29,30} Similar mechanisms have been demonstrated in analogous but less complex systems, such as dimers of metallic nanoparticles. In fact, although the large enhancement generated in the nano-gap of a dimer is the most extensively studied phenomenon in these systems, these structures have also

shown an enhancement at the poles of the dimer.^{5,31} This enhancement was observed to be smaller with respect to the enhancement observed in the gap and to be dependent on the spacing between the nanoparticles.^{5,32} In an analogy, multi-layered structures are composed of metallic thin films separated by nanometric gaps (i.e., dielectric spacers) with one of the poles of this dimer represented by the outermost surface of the substrate, where the multi-layer enhancement is exploited. Furthermore, the multi-layer enhancement has been observed to depend on the thickness of the spacer, in agreement with what was observed in particles dimers.³⁰

The composition of the dielectric spacer material has also been observed to influence the SERS enhancement in dimeric systems. Previous reports have shown that in particle-mirror dimers, which in first approximation behaves as simple dimers, the observed SERS enhancement decrease as a function of the dielectric constant (ϵ) of the spacer material (i.e., the composition of the nano-gap).³² This phenomenon is due to the dielectric constant influencing the SERS enhancement by varying the resistance to the electric field of the material in the gap.

Schottky barrier height (SBH) and interfacial potential ($\Delta\phi$) could also influence the interaction of adjacent metallic films. The SBH is defined as the potential barrier between the Fermi energy of the metal and the bottom of the oxide conductive band at the interface.^{33,34} This property is known to influence the rate at which hot electrons, generated by the decay of a surface plasmon, migrate from the metal to the oxide.³⁵⁻³⁷ Similarly, $\Delta\phi$ can induce migration of the electrons of the metal at the interface into gap states on the

oxide.³⁴ Although these properties have limited impact in phenomena related to the bulk metal, due to the surface nature of SERS and of the multi-layer enhancement phenomenon, they could have a significant impact in the overall enhancement by reducing the electron density at the interface.

In this chapter the dependence of the multi-layer enhancement on the material used as the dielectric spacer is characterized to determine which bulk physical properties can predict the observed behavior. The use of different oxides as spacer materials allow the isolation of trends with respect to SBH, $\Delta\phi$ and ϵ . The behavior of the SERS signal obtained on substrates of different thicknesses was characterized for the oxides to compare different materials. The multi-layer enhancement for substrates made with different spacer materials was studied in relation to the different trends in the physical properties under examination. In addition, the red shift observed in dual-layered structures was also evaluated.

3.2 Experimental

Chemicals

Mercaptobenzoic acid (Tokyo Chemical Industry), ethyl alcohol (200 proof; Parmco-Aaper) and toluene (Baker) were used as is, without further purification. Silica spheres (390 nm) were purchased from Bangs Laboratories as a 10% w/w suspension in water. Silver and gold shot (< 4 mm) used for physical vapor deposition were purchased from Kurt J. Lesker with a purity of 99.99%. The precursors for ALD, tetrakis (dimethylamido) titanium IV (TDMAT) and trimethyl aluminum (TMA) were purchased from Sigma Aldrich, and tetrakis (dimethylamino) hafnium IV (TDMAH) was purchased from Strem.

Preparation of Metallic Film over Nanospheres Substrates

Metallic film over nanostructure (MeFON) SERS substrates were generated using a process published previously.²³ Briefly, glass microscope slides (VWR) were cut into uniform strips of 1×2.5 cm, cleaned in a RCA1 solution (1:1:5 NH₄OH: H₂O₂: H₂O) followed by a 1 N HCl solution, for 1 hr each. Subsequently, the strips were washed with distilled water several times prior to a final rinse in 200 proof ethanol and air dried in an oven at 60° C. The silica nanospheres used to provide the underlying nanostructure in the MeFON substrates were prepared from a 10% w/w stock suspension. This stock suspension was washed multiple times with deionized water and reconcentrated by centrifugation. The washed nanospheres were placed in ethanol and sonicated to generate the final 7% w/w suspension used for deposition on the microscope slide. 10 μL drops were then coated onto the microscope slide and the ethanol was allowed to evaporate, leaving a uniform layer of closely packed nanospheres.

Deposition of metallic films on the nanosphere-coated slides was performed by mounting them on a rotating sample holder 15 cm above the tungsten boat in a physical vapor deposition system (Explorer 14; Denton Vacuum). To ensure that the film was grown evenly on the nanostructured substrate, the sample holder was slowly rotated during evaporation. The chamber was maintained at a pressure of 2×10^{-6} Torr and an evaporation rate of 1.0 Å/s (monitored by a quartz crystal microbalance, XTM/2 film thickness monitor; Inficon) was employed during the entire deposition to obtain a high quality film. A film thickness of 250 nm for single layered films and 2×125 nm for dual-layered structures was

kept throughout the experiment, measuring the thickness with the microbalance. In the case of dual-layered structures, deposition of the second metallic film was performed using atomic layer deposition (ALD), or oxidation in the case of silver oxide. Silver film over nanostructures were used for multi-layered structures composed with silver oxide as spacer material. Gold film over nanostructures were used for all the remaining oxides.

Spacer Layer Deposition

The titanium dioxide (TiO_2), hafnium dioxide (HfO_2) and aluminum oxide (Al_2O_3) spacers were fabricated using a flow tube-based, hot-wall ALD reactor,³⁸ by alternating exposure of the metallic surface to a vapor of a precursor and an oxidizer (H_2O) in a complementary, self-limiting manner. The spacer materials were deposited at a temperature of 100°C . Spacer layers of different nominal thicknesses were obtained by varying the number of deposition cycles employed, corresponding to sub-monolayer films through multiple layers. The film thickness and growth rate per cycle were determined using spectroscopic ellipsometry on companion Si samples, revealing a linear growth versus number of cycles. The nominal film thicknesses reported are based on this linear growth rate and the specific number of cycles employed (0.6 \AA/cycle for TiO_2 , 1.5 \AA/cycle for HfO_2 and 0.7 for Al_2O_3). The precursors used were TDMAT, TDMAH and TMA for TiO_2 , HfO_2 and Al_2O_3 , respectively. Silver oxide (Ag_2O) spacers were grown by air oxidation of the silver film for 48 hr. This oxidation time was shown to generate optimal multi-layer enhancements.²³

Surface Enhanced Raman Scattering Measurement System

SERS spectra were obtained using a laboratory built system (see Figure 2.1). A 22.5 mW CW HeNe (632.8 nm) laser (JDS Uniphase) followed by a band-pass filter, to remove plasma emission lines, was used as the excitation source. This beam is reflected off a silver mirror, to obtain the angle necessary for the backscattered setup, and then reflected off a holographic notch filter (Kaiser Optical Systems; super notch) onto a 10× objective (0.25 NA) which focuses the laser onto the SERS substrate surface. The resulting backscattered light is collected and collimated by the same microscope objective before being filtered by two holographic notch filters to reject the elastically scattered light. The filtered signal is then focused with a lens (f/4) onto the slit of a 0.5 m spectrometer (Spectrapro 500i; Acton Research). The dispersed light is detected with a liquid nitrogen cooled charged coupled device (Princeton Instruments). Slit widths on the spectrometer were set to provide a spectral resolution of 10 cm^{-1} . Control of the spectrometer and CCD was performed using WinSpec 32 acquisition software (Roper Scientific) and acquisition times of 500 ms with 9 accumulations were employed for all analyses. Data analysis was performed using Igor Pro 6.36A (WaveMetrics; see Macro A1 and A2 in Appendix A). SERS intensities reported represent the average of 18 measurements (3 substrates with 6 different random locations measured on each).

Diffuse Reflectance Measurements System

Diffuse reflectance spectra were obtained using a laboratory built system (see Figure 2.2). The system used to measure the absorption profile of SERS substrates consisted of an Ocean Optics HR2000 spectrometer coupled to a mini deuterium halogen light source (DT-

Mini-2-GS; Ocean Optics) and a fiber optic reflection probe (R400-7-SR; Ocean Optics). The reflection probe operates in a six around one geometry, with six collection fibers around a single illumination fiber each of which is 400 μm in diameter. The spectrum at each thickness is the average of spectra taken at 3 points on 3 analogous substrates. Data analysis was performed using Igor Pro 6.36A (WaveMetrics; see Macro A1 in Appendix A).

3.3 Results and Discussion

Thickness dependence for different spacer materials

To allow for correct comparison of substrates of different compositions, the spacer thickness dependence of the multi-layer enhancement was studied in substrates having TiO_2 , HfO_2 and Al_2O_3 as spacer materials. These studies involved fabricating and characterizing dual-layered substrates with dielectric spacers of varying thicknesses. To obtain a SERS signal from the outermost surface, the substrates were drop coated with 10 μL of a thiol Raman reporter molecule in ethanol solution (MBA 10^{-3} M). The SERS spectra from the different substrates were measured and the peak at 1075 rel. cm^{-1} (relative to a ring breathing mode of MBA)³⁹ was used to study the behavior of the multi-layer enhancement (i.e., the intensity relative to a single layer substrate of the same overall thickness).

Figure 3.1 shows the SERS intensities of the 1075 rel. cm^{-1} peak as a function of the nominal thickness of the spacer for TiO_2 , HfO_2 and Al_2O_3 , in section a, b and c, respectively. In each of the sections, the vertical dashed line represents the thickness of a

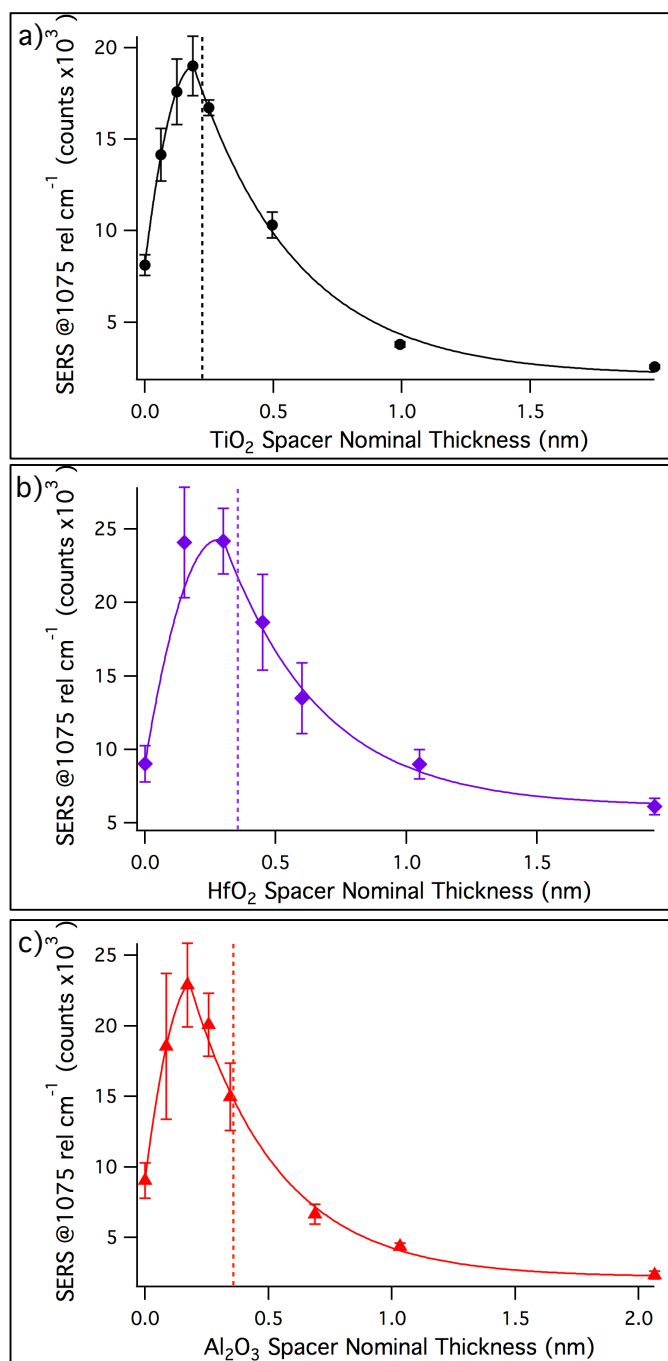


Figure 3.1. Thickness dependence behavior of different multi-layered substrates. **(a)** SERS intensities of a ring breathing mode of MBA chemisorbed on dual-layered substrate made with TiO₂ spacers of different thicknesses. **(b)** For HfO₂ spacers **(c)** For Al₂O₃ spacer. The dashed lines in each of the figures represent the monolayer thickness of the respective materials (0.22, 0.36 and 0.36 nm in respectively a, b and c).

monolayer of the different materials. Literature values were used for the monolayer thickness of TiO₂ and Al₂O₃ (i.e., 0.22 and 0.36 nm, respectively),^{40,41} while for HfO₂ the thickness of a monolayer was calculated with Equation 3.1, by reducing the the number density (i.e., molecules per unit volume) to a single dimension.

$$thickness (ML) = \frac{1}{\sqrt[3]{d}} \quad (3.1)$$

In Equation 3.1 d represent the number density (for HfO₂ equal to 2.77×10^{22} molecules/cm³). The monolayer thickness for HfO₂ was found to be 0.36 nm.

As expected the dual-layered substrates showed an initial growth followed by a decay in the multi-layer enhancement, due to the dependence of the latter on spacer surface coverage and thickness. In Figure 3.1 a trend line was added to the data to aid the visualization of this behavior. The growth in enhancement was demonstrated to be due to the surface coverage of the spacer (Chapter 2), with the maximum enhancement obtained with the thinnest coalescent spacer layer. This condition is found ideally for a monolayer of the material used. The results observed for TiO₂ and HfO₂ spacers confirmed the mechanism proposed to explain the thickness dependence. In contrast, Al₂O₃ spacers showed a maximum in enhancement at thickness lower than a monolayer. Previous reports have shown how it was possible to coat an MeFON substrate with Al₂O₃ with 2 ALD cycles and keep its signal constant for 9 months.⁴² These results suggested the possibility of a coating rate of Al₂O₃ at low ALD cycles larger than the value used herein or a preferential coating in the regions responsible for the SERS enhancement. Despite its initial observation for TiO₂ spacers, the results of these experiments demonstrate the ubiquity of the thickness dependence behavior in oxides and reinforce the hypothesis behind its mechanism.

Surface plasmon resonance vs spacer thickness

To demonstrate that the thickness dependence behavior observed is independent from a shift in the surface plasmon, the reflectance of dual-layered substrates was measured for different spacer thicknesses and compared to that of a single layer substrate. Figure 3.2 shows the reflectance of substrates with HfO₂ spacer layers of different thicknesses (0, 0.15, 0.30, 0.45 and 1.95 nm). As expected, the substrates show a red shift in the maximum surface plasmon resonance (i.e., the minimum in the reflectance trace). In fact, layered nanostructures have been observed to shift the surface plasmon resonance towards the IR as a function of the spacing between adjacent metallic films, due to the stronger interaction between layers.⁴³ In agreement with this mechanism, the observed behavior also correlates with the SERS spectra, as the largest shift was observed for 0.15 and 0.30 nm (b and c in Figure 3.2, respectively) which are the substrates that showed the highest SERS intensities (Figure 3.1b). Although the overlapping of the surface plasmon with the Rayleigh and Raman scattering is known to determine the SERS signal magnitude, it was not the cause of the larger enhancement in the red-shifted substrates. An optimum surface plasmon

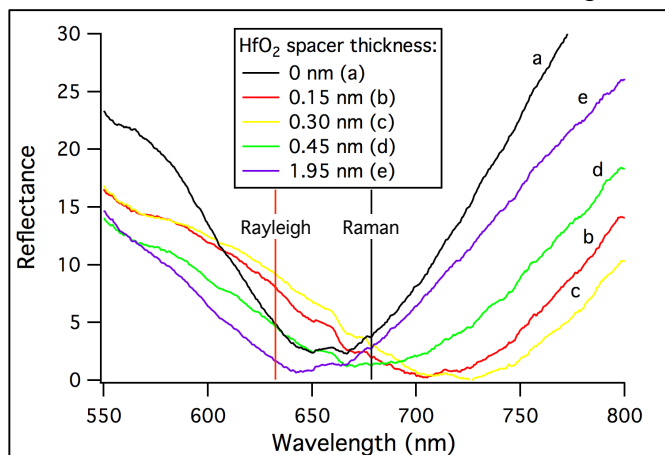


Figure 3.2. Reflectance spectra of dual-layered substrates made with various thicknesses of HfO₂ (see legend in the inset). In the figure are also reported the wavelength of Rayleigh scattering (633 nm) and of the Raman band observed at 1075 rel. cm⁻¹ (679 nm), red and black solid lines, respectively.

resonance for the laser source used would have had a maximum around 656 nm, the median point between Rayleigh and observed Raman peak. To note, this optimal condition is observed in the single-layer substrate, which was optimized to give the strongest SERS enhancement (trace a in Figure 3.2).

Multi-layer enhancement vs spacer properties

To compare the dual-layered substrates fabricated with different spacer materials the maximum multi-layer enhancement (i.e., maximum improvement in SERS signal of a dual-layered substrates with respect to a single layer analogous) for each material was obtained. The maximum enhancement was used to ensure that the spacers for each material were composed of a single monolayer, making them deviate in parallel from the bulk properties. The enhancement was calculated from the substrate with the spacer thickness that showed the highest SERS intensity for each material as the ratio of the SERS intensity of MBA on the dual-layered substrate over that on a single layer substrate of the same overall thickness. The intensity of the MBA that was drop coated on the substrates (10 μ L of 10^{-3} M solution in ethanol) was measured as the mean of the intensities of the two ring breathing mode of MBA at 1075 and 1588 rel. cm^{-1} .³⁹ The spectra used to calculate the intensities were background subtracted using the baseline of a single layer substrate made of 125 nm of gold, and was also used to normalize the intensities obtained on different days.

Figure 3.3a shows the SERS spectra of MBA on the dual-layered substrate made with different spacer materials and on a conventional single layer substrate. Figure 3.3b shows a particular of the spectra, near the 1588 rel. cm^{-1} peak, to allow visualization of the

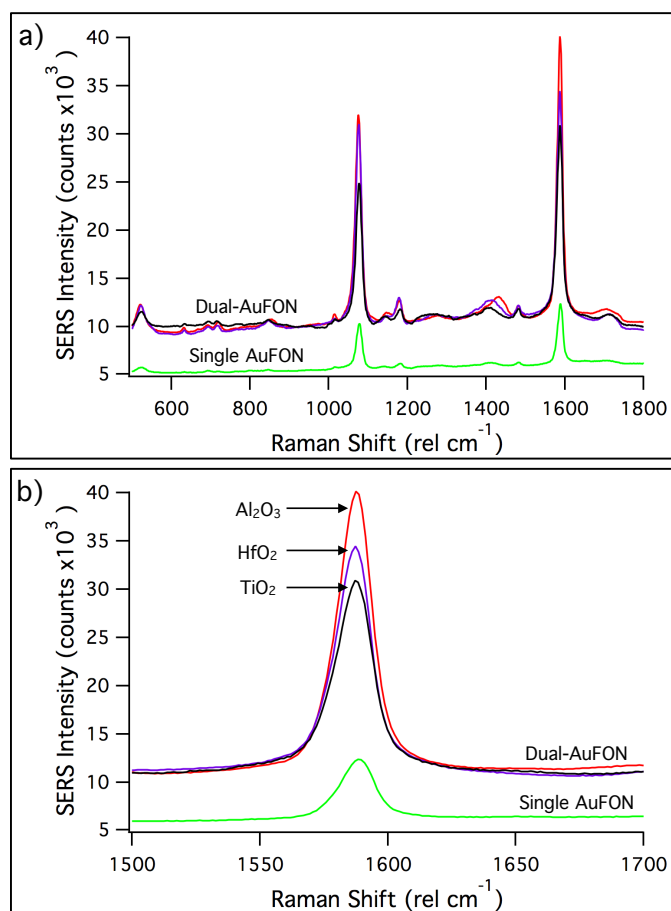


Figure 3.3. (a) Spectra of MBA chemisorbed on the surface of dual-layered substrates (Dual-AuFON) fabricated with dielectric spacer composed of differ materials, indicated by the different colored lines. The spectrum labeled as Single-AuFON is relative to a single layer substrate of the same overall thickness. (b) A close up of the spectra reported in section (a) around the 1588 rel. cm^{-1} peak of MBA. The labels next to the spectra show the spacer oxide relative to the spectrum.

different traces. The multi-layer enhancements calculated for the different substrates were of 2.31 ± 0.03 , 2.58 ± 0.04 and 2.63 ± 0.04 respectively for TiO_2 , HfO_2 and Al_2O_3 . The enhancement was also calculated for optimized silver dual-layered substrates using the native oxide as spacer material, which is the composition used in the original discovery of the multi-layer enhancement. These substrates showed a multi-layered enhancement of 2.7 ± 0.2 . The larger error observed for these substrates is due to the low control of the fabrication of native oxide spacers, which can result in spacers layers with spatially

inhomogeneous surface coverage. All the enhancements reported herein are calculated for dual-layer substrates, however, previous results have shown that the enhancement can be increased further by using a larger number of isolated metallic layers.²³

The oxides used as spacer materials were selected to isolate trends in the physical properties thought to influence the multi-layer enhancement (i.e., SBH, $\Delta\phi$ and ϵ). The multi-layer enhancements obtained with the different spacer materials were plotted as a function of the property and the data were compared to the expected trends. To aid the understanding of the expected trends, a scheme of the mechanism of influence for each property is also represented.

Figure 3.4a depicts the mechanism by which SBH could influence the multi-layer enhancement. The mechanism consists in the excitation source radiating the metallic nanostructures and exciting a surface plasmon, which decays by generating excited electrons with increased energies comparable to the incoming radiation.^{36,37} If the energy of the excited electrons is higher than the potential barrier formed at the oxide/metal interface (i.e., Schottky barrier), such electrons can populate the conduction band of the oxide.³⁷ The energy necessary to overcome this barrier is the SBH.

SBH of an oxide/metal interface can be calculated as the difference in energy between the Fermi level (E_f) of the metal used and the bottom of the conductive band of the oxide (E_c), as shown in Figure 3.4a. These energies are calculated from the work function (ϕ_M) and electron affinity (χ) of the materials, respectively, for Fermi level and bottom of conductive band.³⁴ The SBH calculated for the interfaces with the materials used in these experiments

were of 0.3 eV for Ag₂O/Au,⁴⁴ 0.85 eV for TiO₂/Au,³⁶ 2.9 eV for HfO₂/Au,^{34,45} and 4.4 eV for Al₂O₃/Au.^{34,45}

The multi-layer enhancement is expected to vary according to the number of free charges at the interface of the metal. Therefore, oxides with low SBH are expected to perform as less efficient spacer materials due to the depopulation of electrons at the interface. According to the mechanism proposed, the multi-layer enhancement should gradually

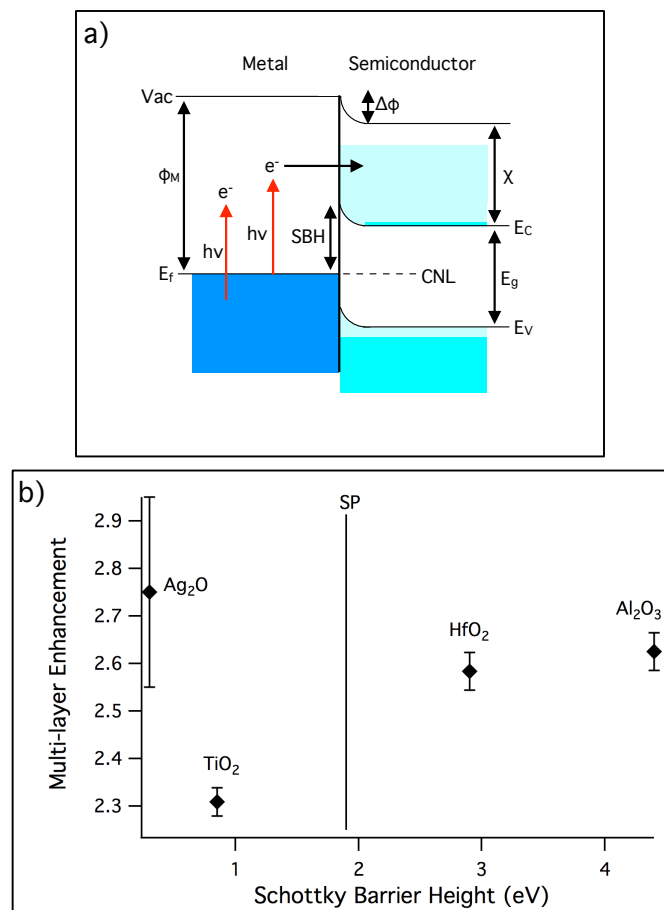


Figure 3.4. (a) Schematic representation of the mechanism by which SBH influences the multi-layer enhancement. Excited electrons generated by the surface plasmon populate the conduction band of the oxide. This process is controlled by the SBH, which can be calculated from the work function of the metal (ϕ_M) and the electron affinity of the oxide (χ) (b) Multi-layer enhancement magnitude plotted as a function of SBH for the spacer material. The vertical solid line mark the energy of the incoming radiation and of the excited surface plasmon, 1.9 eV (633 nm).

increase as a function of the SBH of the oxide as a results of the smaller number of electrons that can be excited to energies above this barrier, considering a monochromatic and constant excitation source. For SBH with energies greater than the incoming radiation of 633 nm (1.9 eV) the multi-layer enhancement is expected to plateau at its maximum, since electrons cannot be excited over the potential barrier.

The results shown in Figure 3.4b in part disagree with the expected behavior. While for materials with SBH larger than 1.9 eV (solid line labeled as SP in the figure) the enhancement observed have statistical identical magnitudes, these values do not represent the maximum enhancement observed. The multi-layer enhancement was observed to first decrease at low SBH values, between Ag₂O and TiO₂, suggesting that this property alone cannot predict the trend observed in the multi-layer enhancement.

$\Delta\phi$ was also evaluated for the interfaces to determine its influence on the multi-layer enhancement, due in this case to the migration of the semiconductor electrons into the metal. Figure 3.5a shows the mechanism by which $\Delta\phi$ could influence the multi-layer enhancement. The electrons population of the semiconductor bands rearrange due to the contact with the metal and the necessary alignment of the Fermi energy of these materials. The magnitude of this electrons migration depends on the relative Fermi energy of the metal and the charge neutrality level (CNL) of the oxide.³⁴ The difference between these potentials determine the $\Delta\phi$, and can be calculated from the work function of the metal and the theoretical work function of the oxide (ϕ_S). The multi-layer enhancement is expected to decrease as a function of $\Delta\phi$ (calculated as $\phi_S - \phi_M$), due to a reduced migration of

electrons into the metallic interface. $\text{Ag}_2\text{O}/\text{Ag}$, TiO_2/Au , HfO_2/Au and $\text{Al}_2\text{O}_3/\text{Au}$ have $\Delta\phi$ of 0, -0.7, -0.6 and -1.1 eV, respectively.^{33,34,44,45} $\Delta\phi$ is also responsible for the band bending represented in Figure 3.4a.

The multi-layer enhancement obtained with the spacer materials as a function of $\Delta\phi$ is shown in Figure 3.5b. As can be observed, the data are scattered and do not follow any determined trend. The expected decrease in multi-layer enhancement as function of $\Delta\phi$ was

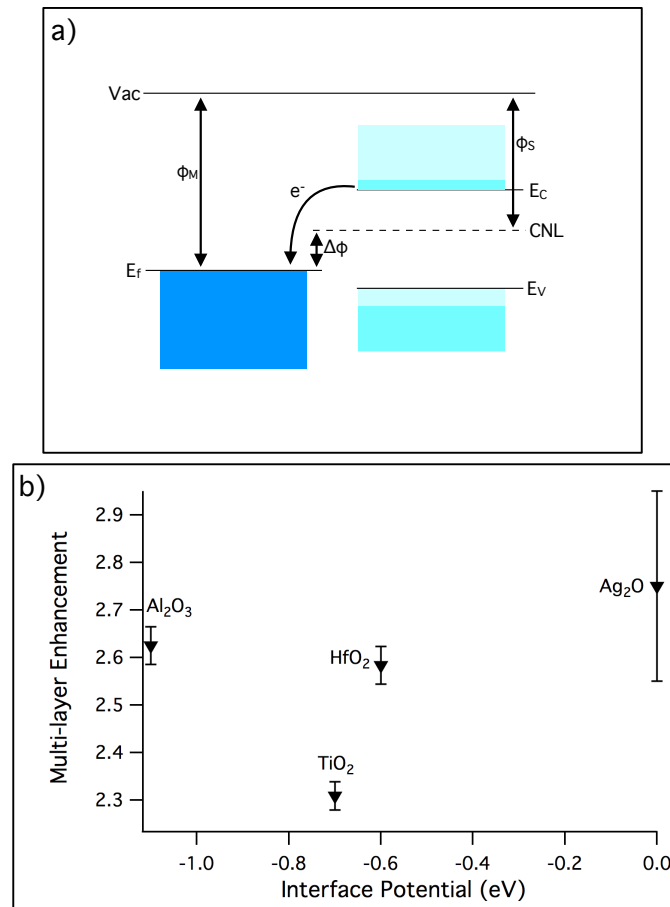


Figure 3.5. (a) Schematic representation of the mechanism by which $\Delta\phi$ influences the multi-layer enhancement. Electrons from the metal are depleted at the interface into gap states of the oxide layer. This process is driven by the difference between the Fermi energy of the metal (E_f) and the charge neutrality level of the oxide (CNL). These quantities can be calculated from the respective work functions (ϕ_M and ϕ_S) **(b)** Multi-layer enhancement magnitude plotted as a function of $\Delta\phi$ for the spacer material.

not observed in the data, suggesting that this physical property does not have a strong influence on the multi-layer enhancement observed.

In contrast with the other properties investigated, the dielectric constant was observed to predict the trend in multi-layer enhancement. Figure 3.6a shows the mechanism by which the dielectric constant might influence the multi-layer enhancement. The electric field from the surface plasmon generated on a metallic surface decays exponentially with distance from

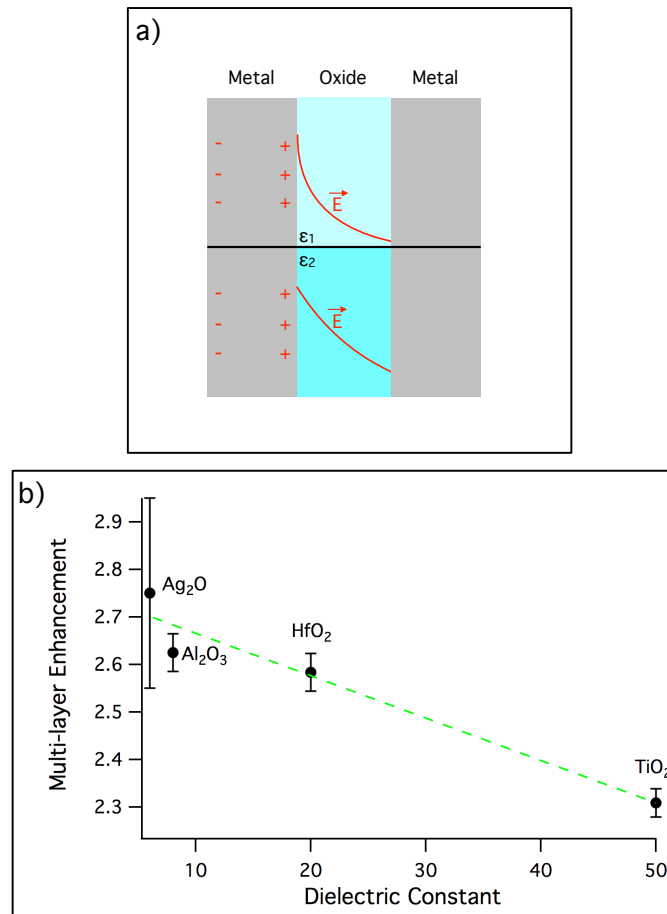


Figure 3.6. (a) Schematic representation of the mechanism by which ϵ influences the multi-layer enhancement in two different systems, with high and low dielectric constants (ϵ_1 and ϵ_2). The top system depicts how in a high dielectric constant medium the electric field (solid line labeled as \vec{E}) decays more rapidly with distance (on the x-axis) with respect to the bottom system, characterized by a low dielectric constant. (b) Multi-layer enhancement magnitude plotted as a function of ϵ of the spacer material. The data were fitted to a line (dashed line) to aid the visualization of the trend.

the surface, represented by the solid line labeled as \mathbf{E} in the figure.⁴⁶ The damping of the electric field in the propagation medium (i.e., the oxide layer) depends on its dielectric constant (ϵ_i). The electric field has a steeper decay in a medium with a larger dielectric constant (ϵ_1) with respect to a low dielectric constant (ϵ_2) analogous. Because the multi-layer enhancement is generated by the interaction between the surface plasmons in proximal metallic films, a lower dielectric constant material is expected to work as a more efficient spacer by increasing such interaction.

Figure 3.6b shows the multi-layer enhancement as a function of the dielectric constant of the spacer material, which are of 6, 8, 20 and 50 for respectively Ag_2O , Al_2O_3 , HfO_2 and TiO_2 .⁴⁷⁻⁴⁹ The multi-layer enhancement was observed to monotonically increase by reducing the dielectric constant, in agreement with the expected results. In the figure the trend was fitted to a straight line to aid its visualization. To be noticed that although the errors in the enhancement do not allow the clear distinction between the enhancements in low dielectric materials, the trend in the data is clear, in fact, to every decrease in dielectric constant is associated an increase in multi-layer enhancement. The overall results suggest that the dielectric constant, rather than SBH and $\Delta\phi$, can be used to predict the multi-layer enhancement obtained for a specific spacer material.

3.4 Conclusions

This chapter focused on understanding the role of the physical properties of materials used as dielectric spacer in multi-layered structures. The dielectric constant of the material was observed to predict the trend in multi-layer enhancement, while other hypothesized

dependences (SBH and $\Delta\phi$) showed very low or no correlation with the enhancement data. In order to compare substrates composed with different spacer materials, the thickness dependence for each was studied, consistently showing a non-monotonic behavior. Furthermore, the enhancement trends were also demonstrated to be independent from the shifts observed in the surface plasmon resonance of substrates.

The results of this chapter in combination with the known thickness dependence of multi-layered structures, discussed in Chapter 2, allow for the design of optimal spacers for multi-layer structures. In particular, the use of bulk properties rather than the specific spacer properties permits to know *a priori* the efficiency of a spacer. Optimal spacers for multi-layered structures are composed of the lowest obtainable coalescent film of a low dielectric constant material. Future direction will focus on the use of low dielectric constant materials and in the technological challenges associated with growing ultrathin coalescent films with such materials.

3.5 References

- (1) Fleischmann, M.; Hendra, P. J.; McQuillan, A. J. *Chemical Physics Letters* **1974**, *26*, 163.
- (2) Jeanmaire, D. L.; Van Duyne, R. P. *Journal of Electroanalytical Chemistry and Interfacial Electrochemistry* **1977**, *84*, 1.
- (3) Moskovits, M. *Journal of Raman Spectroscopy* **2005**, *36*, 485.
- (4) Rodriguez-Lorenzo, L.; Fabris, L.; Alvarez-Puebla, R. A. *Analytica Chimica Acta* **2012**, *745*, 10.
- (5) Kelly, K. L.; Coronado, E.; Zhao, L. L.; Schatz, G. C. *The Journal of Physical Chemistry B* **2003**, *107*, 668.
- (6) Xu, H.; Aizpurua, J.; Käll, M.; Apell, P. *Physical Review E* **2000**, *62*, 4318.
- (7) Strobbia, P.; Languirand, E.; Cullum, B. M. *Optical Engineering* **2015**, *54*, 100902.
- (8) Yuan, H.; Register, J.; Wang, H.-N.; Fales, A.; Liu, Y.; Vo-Dinh, T. *Analytical and Bioanalytical Chemistry* **2013**, *405*, 6165.

- (9) McNay, G.; Eustace, D.; Smith, W. E.; Faulds, K.; Graham, D. *Applied Spectroscopy* **2011**, *65*, 825.
- (10) Sharma, B.; Frontiera, R. R.; Henry, A.-I.; Ringe, E.; Van Duyne, R. P. *Materials Today* **2012**, *15*, 16.
- (11) Harper, M. M.; McKeating, K. S.; Faulds, K. *Physical Chemistry Chemical Physics* **2013**, *15*, 5312.
- (12) Kneipp, K.; Haka, A. S.; Kneipp, H.; Badizadegan, K.; Yoshizawa, N.; Boone, C.; Shafer-Peltier, K. E.; Motz, J. T.; Dasari, R. R.; Feld, M. S. *Applied Spectroscopy* **2002**, *56*, 150.
- (13) Kneipp, K.; Kneipp, H. *Applied Spectroscopy* **2006**, *60*, 322A.
- (14) Moskovits, M. *Physical Chemistry Chemical Physics* **2013**, *15*, 5301.
- (15) Kneipp, K.; Kneipp, H.; Manoharan, R.; Hanlon, E. B.; Itzkan, I.; Dasari, R. R.; Feld, M. S. *Applied Spectroscopy* **1998**, *52*, 1493.
- (16) Graham, D.; Thompson, D. G.; Smith, W. E.; Faulds, K. *Nature Nanotechnology* **2008**, *3*, 548.
- (17) Kim, N. H.; Lee, S. J.; Moskovits, M. *Nano Letters* **2010**, *10*, 4181.
- (18) Vo-Dinh, T.; Hiromoto, M. Y. K.; Begun, G. M.; Moody, R. L. *Analytical Chemistry* **1984**, *56*, 1667.
- (19) Hulteen, J. C.; Treichel, D. A.; Smith, M. T.; Duval, M. L.; Jensen, T. R.; Van Duyne, R. P. *The Journal of Physical Chemistry B* **1999**, *103*, 3854.
- (20) Leverette, C. L.; Shubert, V. A.; Wade, T. L.; Varazo, K.; Dluhy, R. A. *The Journal of Physical Chemistry B* **2002**, *106*, 8747.
- (21) Khoury, C. G.; Vo-Dinh, T. *The Journal of Physical Chemistry C* **2008**, *112*, 18849.
- (22) Li, H.; Patel, P. H.; Cullum, B. M. *Proc. SPIE* **2004**, 5588, 558887.
- (23) Li, H.; Cullum, B. M. *Applied Spectroscopy* **2005**, *59*, 410.
- (24) Li, H.; Baum, C. E.; Sun, J.; Cullum, B. M. *Proc. SPIE* **2006**, 6218, 6218041.
- (25) Li, H.; Baum, C. E.; Sun, J.; Cullum, B. M. *Applied Spectroscopy* **2006**, *60*, 1377.
- (26) Hankus, M. E.; Li, H.; Gibson, G. J.; Cullum, B. M. *Analytical Chemistry* **2006**, *78*, 7535.
- (27) Cullum, B. M.; Li, H.; Hankus, M. E.; Schiza, M. V. *NanoBiotechnology* **2007**, *3*, 1.
- (28) Chae, J.; Lahiri, B.; Kohoutek, J.; Holland, G.; Lezec, H.; Centrone, A. *Optics Express* **2015**, *23*, 25912.
- (29) Strobbia, P.; Henegar, A.; Gougousi, T.; Cullum, B. M. *Proc. SPIE* **2015**, 9487, 94870P.
- (30) Strobbia, P.; Henegar, A. J.; Gougousi, T.; Cullum, B. M. *Applied Spectroscopy* **2016**, (in press).
- (31) Schultz, Z. D.; Wang, H.; Kwasnieski, D. T.; Marr, J. M. *Proc. SPIE* **2015**, 9554, 9554091.
- (32) Mubeen, S.; Zhang, S.; Kim, N.; Lee, S.; Krämer, S.; Xu, H.; Moskovits, M. *Nano Letters* **2012**, *12*, 2088.
- (33) Robertson, J. *The European Physical Journal - Applied Physics* **2004**, *28*, 265.
- (34) Robertson, J. *Journal of Vacuum Science & Technology B* **2000**, *18*, 1785.
- (35) Brongersma, M. L.; Halas, N. J.; Nordlander, P. *Nat Nano* **2015**, *10*, 25.
- (36) Mubeen, S.; Hernandez-Sosa, G.; Moses, D.; Lee, J.; Moskovits, M. *Nano Letters* **2011**, *11*, 5548.
- (37) Clavero, C. *Nature Photonics* **2014**, *8*, 95.

- (38) Hackley, J. C.; Gougousi, T.; Demaree, J. D. *Journal of Applied Physics* **2007**, *102*, 034101.
- (39) Michota, A.; Bukowska, J. *Journal of Raman Spectroscopy* **2003**, *34*, 21.
- (40) Ferguson, J. D.; Yoder, A. R.; Weimer, A. W.; George, S. M. *Applied Surface Science* **2004**, *226*, 393.
- (41) Wilson, C. A.; Grubbs, R. K.; George, S. M. *Chemistry of Materials* **2005**, *17*, 5625.
- (42) Zhang, X.; Zhao, J.; Whitney, A. V.; Elam, J. W.; Van Duyne, R. P. *Journal of the American Chemical Society* **2006**, *128*, 10304.
- (43) Bardhan, R.; Mukherjee, S.; Mirin, N. A.; Levit, S. D.; Nordlander, P.; Halas, N. J. *The Journal of Physical Chemistry C* **2010**, *114*, 7378.
- (44) Tjeng, L. H.; Meinders, M. B. J.; van Elp, J.; Ghijsen, J.; Sawatzky, G. A.; Johnson, R. L. *Physical Review B* **1990**, *41*, 3190.
- (45) Hölzl, J.; Schulte, F. K. In *Solid Surface Physics*; Hölzl, J., Schulte, F. K., Wagner, H., Eds.; Springer Berlin Heidelberg: Berlin, Heidelberg, 1979, p 1.
- (46) Maier, S. A. *Plasmonics: Fundamentals and Applications*; Springer US: New York USA, 2007.
- (47) Rentería-Tapia, V. M.; Valverde-Aguilar, G.; García-Macedo, J. A. **2007**, 6641, 66411W.
- (48) Groner, M.; George, S. *Interlayer Dielectrics for Semiconductor Technologies* **2003**, *1*, 327.
- (49) Singh, R.; Ulrich, R. K. *Electrochem. Soc. Interface* **1999**, *8*, 26.

Chapter 4:

Regeneration and Multi-Layer Amplification of Sensing

Characteristics in Commercial Substrates for SERS

4.1 Introduction

Surface enhanced Raman spectroscopy (SERS) is an analytical technique that exploits the enhanced scattering properties of metallic nanostructures.¹⁻³ In fact, on the surfaces of such structures the intensity of Raman scattering is amplified of numerous orders of magnitude, providing chemical and structural information regarding molecules in the surface proximities.^{4,5} Numerous sensing platform based on this technique have been developed over the years, and can be found in many reviews.⁶⁻¹⁰ However, due to issues with obtaining simultaneously large and reproducible SERS enhancements, the applications of this sensing technique in real-world scenarios have been limited.

Issues with reproducibility arise from the structural motifs used to generate large SERS enhancements, nano-gaps and sharp edges.⁶ The techniques commonly used for the fabrication of these motifs, such as colloidal aggregation and anisotropic growth of nanoparticles, are not capable to yield SERS substrates with homogeneous enhancements over a large area.^{11,12} However, this characteristic is required to achieve the use of SERS sensing platforms in real world applications. To this end, SERS substrates based on organized arrays have been developed, achieving reproducibilities over the substrate area lower than 10%.¹³

SERS substrates based on arrays of nanostructures have been fabricated in numerous ways, generating varying reproducibilities and enhancements.¹⁴⁻¹⁹ Among them, structures fabricated with lithographic techniques can yield structures with the highest precision. Due to this characteristic, such structures have been used for fundamental studies of the SERS phenomenon.^{14,15} However, due to the high expenses of time and cost that these techniques require, lithography is generally not considered as a viable option for the development of SERS sensors for real world applications. Wet chemistry techniques have also been used to fabricate nanoscopic features in SERS substrates (e.g., metallic film over nanospheres, nanospheres lithography and chemical etching).^{16,18} The use of these techniques allow for the production of SERS substrates with good reproducibility throughout their surfaces in a cost effective and scalable manner.

Klarite substrates are one of the first examples of commercial SERS substrates fabricated by chemical etching. The substrates consist in silicon wafers chemically etched, to form an inverted pyramids surface topography, prior to coating with a thin film of gold (i.e., 500 nm).²⁰ These substrates have been used in numerous publication, as primary SERS substrates or as a standard for the comparison of sensing figures of merit.²¹⁻²³ However, these substrates were designed for a single measurement and to be disposable, reducing their applicability.²⁴

In this paper, the possibility to regenerate and amplify Klarite substrates is demonstrated. A regeneration process was developed and its results studied by measuring the Raman

signal from the substrate surface. Sensing and surface characteristics of the substrates, such as surface plasmon resonance (SPR), sensitivity and reproducibility, were compared between regenerated and original substrates and for different regeneration cycles. Multi-layered Klarite substrates were also fabricated and their sensing performance compared with single layered substrates.

4.2 Experimental

Chemicals

Chemicals used included benzoic acid (BA; Sigma), 1,2-Di(4-pirydy)ethylene (BPE; Aldrich), nitric acid (15 M; Fisher), hydrochloric acid (12 M; Fisher), sulfuric acid (36M; Fisher), hydrogen peroxide (36% v/v; VWR) and ethanol (200 proof; Parmco-Aaper). Gold pellets used for physical vapor deposition were purchased from Kurt J. Lesker with a purity of 99.99%. The precursors for atomic layer deposition (ALD), tetrakis (dimethylamido) titanium IV (TDMAT), was purchased from Sigma Aldrich. All chemicals were used as received without further purification.

Substrates

Commercially available slide mounted Klarite SERS substrates were purchased from D3 Technologies. Slides were individually wrapped and vacuum sealed. The SERS active area on these slides was a small 4 x 4 mm wafer with a gold surface. The original Klarite substrates were opened just prior to measurement to avoid any possible surface fouling. The substrates used were from the series #302, #312 and #313.

Metallic Film Deposition

Deposition of metallic films on the silicon wafers (i.e., gold-stripped substrates) was performed after mounting them on a rotating sample holder 15 cm above the tungsten boat in a physical vapor deposition system (Explorer 14; Denton Vacuum). To ensure that the film was grown evenly on the nanostructured substrate, the sample holder was slowly rotated during evaporation. The chamber was maintained at a pressure of 1.5×10^{-6} Torr and an evaporation rate of 0.7 Å/s (monitored by a quartz crystal microbalance, XTM/2 film thickness monitor; Inficon) was employed during the entire deposition. The thickness of the film and the deposition rate reported were extrapolated after a profilometry calibration on deposited gold films.

Spacer Layer Deposition

The titanium dioxide (TiO₂) spacers were fabricated using a flow tube-based, hot-wall ALD reactor,²⁵ by alternating exposure of the metallic surface to a vapor of a precursor and an oxidizer (H₂O) in a complementary, self-limiting manner. The material was deposited at a temperature of 100° C. The thickness of the spacer was kept at 0.19 nm (3 cycles), as optimized elsewhere.²⁶ The precursors used was TDMAT.

Surface Enhanced Raman Scattering Measurement System

SERS spectra were obtained using a laboratory built system (Figure 4.1). A 22.5 mW CW HeNe (632.8 nm) laser (JDS Uniphase) followed by a band-pass filter, to remove plasma emission lines, was used as the excitation source. This beam is reflected off of a silver mirror, to obtain the angle necessary for the backscattered setup, and then reflected by a

holographic notch filter (Kaiser Optical Systems; super notch) onto a 10× objective (0.25 NA) which focuses the laser onto the SERS substrate surface. The resulting backscattered light is collected and collimated by the same microscope objective before being filtered by two holographic notch filters to reject the elastically scattered light. The filtered signal is then focused with a lens (f/4) onto the slit of a 0.5 m spectrometer (Spectrapro 500i; Acton Research). The dispersed light is detected with a liquid nitrogen cooled charged coupled device (Princeton Instruments). Control of the spectrometer and CCD was performed using WinSpec 32 acquisition software (Roper Scientific) and acquisition times of 10 s were employed the analyses. Data analysis was performed using Igor Pro 6.36A (WaveMetrics; see Macro A1 and A3 in Appendix A).

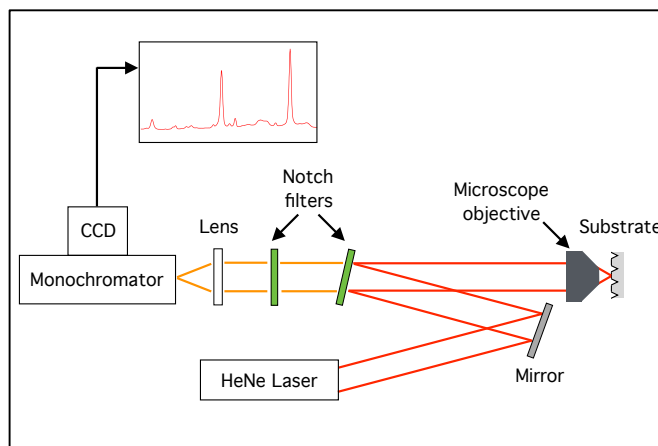


Figure 4.1. Schematic diagram depicting optical system used for the SERS measurements.

Diffuse Reflectance Measurements System

Diffuse reflectance spectra were obtained using a laboratory built system (Figure 4.2). The system used to measure the absorption profile of SERS substrates consisted in an Ocean Optics HR2000 spectrometer coupled to a mini deuterium halogen light source (DT-Mini-

2-GS; Ocean Optics) and a fiber optic reflection probe (R400-7-SR; Ocean Optics). The reflection probe operates in a six around one geometry, with six collection fibers around a single illumination fiber each of which is 400 μm in diameter. Data analysis was performed using Igor Pro 6.36A (WaveMetrics; see Macro A1 in Appendix A).

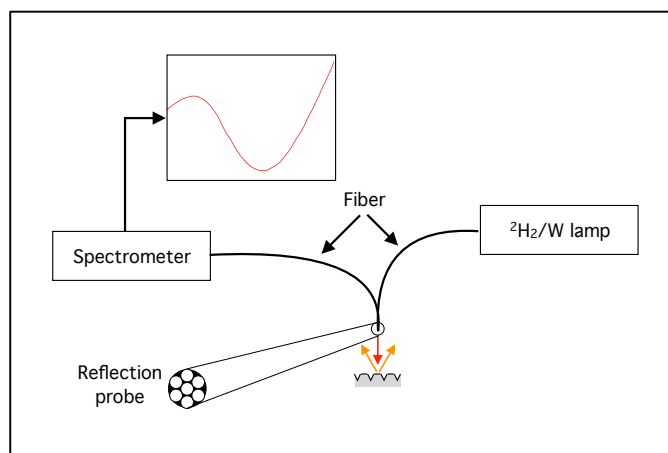


Figure 4.2. Schematic diagram depicting the system used for the diffuse reflectance measurements.

4.3 Results and Discussion

Regeneration of Klarite substrates

To reuse the Klarite substrates, the original gold surface was removed from the silicon underlying structure and a new gold thin film applied. Gold removal on the substrate surface was achieved using a solution of aqua regia (1:3 concentrated nitric acid: concentrated hydrochloric acid) followed by cleaning with piranha solution (1:3 hydrogen peroxide: concentrated sulfuric acid), to remove any contaminant from the substrate surface. Approximately 2 mL of each solution were used to drop coat the Klarite substrates. The process consisted of drop coating the substrate in aqua regia letting it react for 5 min, followed by 15 min with piranha solution and an additional 5 min in aqua regia, to ensure that all the gold was removed. After the gold removal the substrates were

rinsed with 0.1 N nitric acid, deionized water, ethanol and dried under airflow to avoid watermarks. Substrates treated as described were then regenerated by depositing a gold thin film of 480 nm thickness using physical vapor deposition. In the following sections the physical characteristics and analytical figures of merits are analyzed for such regenerated substrates.

To verify the effectiveness and completion of the regeneration process Raman spectra of the surface of the substrates were taken at the different stages into the procedure described above. Figure 4 shows the spectra measured on a K302 substrate as received (a), after the removal of gold (b, d), after a regeneration cycle (c). The substrates were all drop coated with 10 μL of a 10^{-2} M solution of BPE in ethanol, except for spectrum b. Several characteristics peaks of BPE were observed at 994, 1197, 1595 and 1636 rel. cm^{-1} , as previously observed in SERS spectra of this molecule.²⁷ For spectra measured after gold removal a peak was observed at 520 rel. cm^{-1} , relative to the spontaneous Raman band of crystalline silicon. The spectrum from the original substrate (a) shows peaks relative to BPE with a signal-to-noise ratio (SNR) of 79 for the band at 1636 rel. cm^{-1} . After

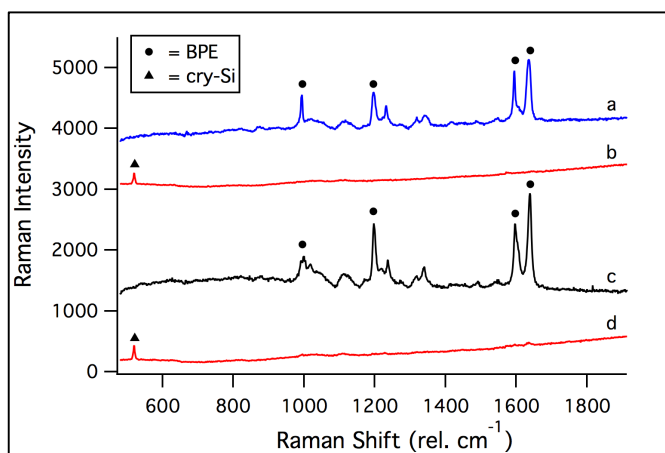


Figure 4.3. (a) Raman spectrum of BPE adsorbed on the surface of a new Klarite substrate. (b) Raman spectrum measured from the surface of a Klarite substrate after the removal of the gold film. (c) Raman spectrum of BPE adsorbed on the surface of a regenerated Klarite substrate. (d) Raman spectrum of BPE adsorbed on the surface of a Klarite substrate after the removal of the gold film.

the removal of the gold film (b) the SERS signal of BPE is no longer observed. In spectrum b is observed a peak ascribed to crystalline silicon, due to the silicon underlying structure being exposed to the laser excitation. When the substrate is regenerated and drop coated again with BPE (c) the spectrum shows the bands observed for the initial substrate, with a SNR at $1636 \text{ rel. cm}^{-1}$ consistent with that observed on the original substrate. After an additional removal of the gold film the substrate was also drop coated with BPE (d) to verify that the bands observed were not from spontaneous Raman. The spectrum of such treated substrate shows none of the peaks previously observed except for at $1636 \text{ rel. cm}^{-1}$, where is visible a peak which has a SNR barely over the limit of detection (i.e., 3.1). The results obtained in the experiment suggest that gold and previous surface contaminants can be removed using the regeneration process described above and that the SERS properties of the substrates can also be regenerated.

Surface Plasmon Resonance

Due to the strong relation between the SPR and SERS phenomena,²⁸ the SPR of each substrate was measured to ensure that the SPR peaks fall at the same wavelength values for original and regenerated substrates. Figure 4.4a shows the reflectance spectra of 3 different #302 Klarite substrates after a varying number of regeneration cycles. The spectra from the substrates show multiple minima, which correspond to the resonant wavelengths of different surface plasmon modes, around 565 and 745 nm. As it can be observed from the figure the minima of the regenerated substrates fell at identical wavelengths with respect to the original and to each other.

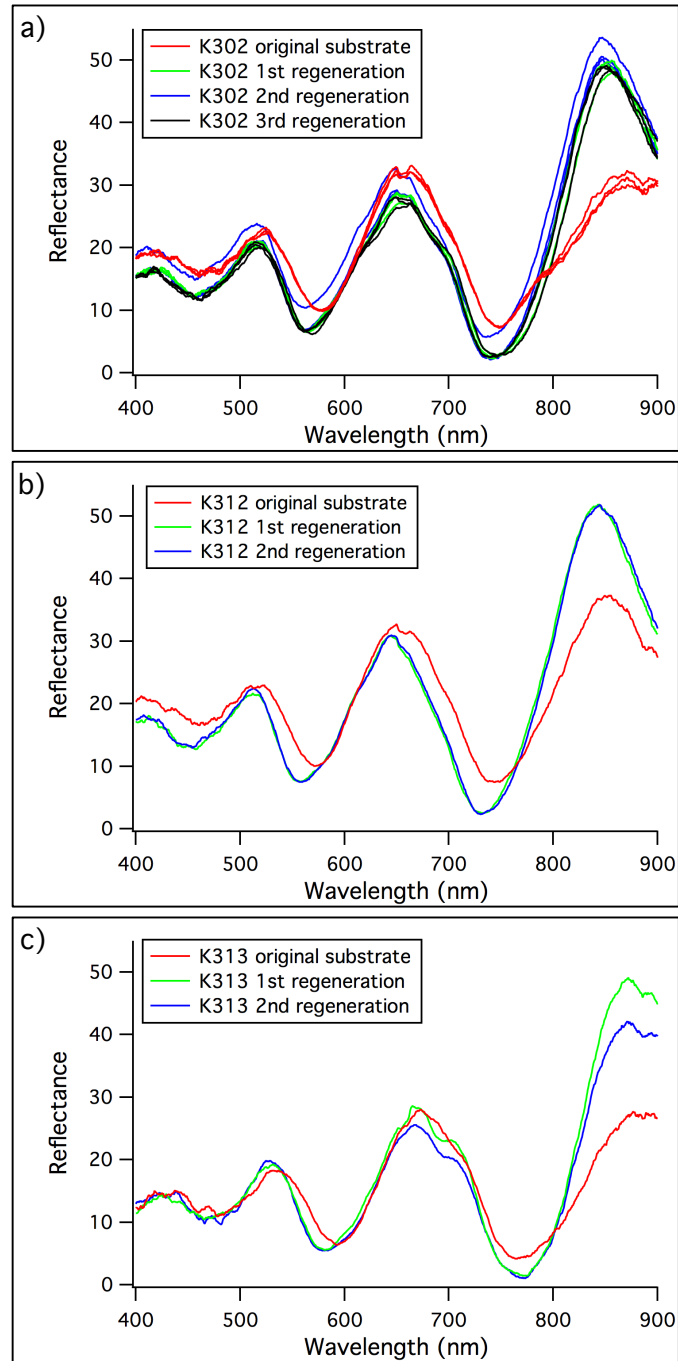


Figure 4.4. Reflectance spectra of Klarite substrates from different series. Different colors represent the different regeneration cycles red, green, blue and black lines for 0, 1, 2 and 3 regenerations, respectively. **(a)** For #302 Klarite substrates (3 substrates), **(b)** For a #312 Klarite substrate, and **(c)** for a #312 Klarite substrate.

These results demonstrate that after several regeneration processes the plasmonic characteristics of the metallic surface are not significantly modified.

To demonstrate the versatility of this regeneration process, different types of Klarite substrate were used in this experiment. Figure 4.4b and 4.4c shows the spectra of a #313 and #312 Klarite substrate, respectively, after different regeneration cycles. In Figure 4.4b the SPR minima are at slightly different wavelength, 585 and 770 nm with respect to Figure 4.4a, whereas in Figure 4.4c the minima are at roughly the same wavelengths (570 and 745 nm) of the #302 Klarite. As it can be observed in the case of the #313 (Figure 3b) the reflectance spectra do not change after the regeneration. Figure 4.4c shows a small shift in the spectra of the regenerated substrates with respect to the original, such shift was ascribed to the amount of metal deposited being different on the original and on the regenerated sample, as the amount of gold for each substrate type was not disclosed. In addition, a shift in the surface plasmon as a function of the amount of metal deposited was observed in Klarite regenerations, substrates deposited with 310 nm of Au shown a red shift ($\Delta\lambda = 40$ nm) with respect to the 480 nm depositions. This phenomenon could be useful for application that require SPR in different regions of the spectrum. These results show that the regeneration process is valid for different types of Klarite substrates and suggest that this method could be used for any substrate composed of a silicon structures coated with a metallic thin film, a common motif in SERS substrates.

SERS-sensing figures of merit of regenerated substrates

To compare the sensing-related figures of merit of the regenerated substrates the standard Raman/SERS response of a common reporter molecule, benzoic acid (BA), was measured. For data analysis, the signal from the major BA peak at $1002 \text{ rel. cm}^{-1}$ was chosen for signal-to-noise determination, with the noise determined as the standard deviation over a range of wavelengths from 1752 to $1874 \text{ rel. cm}^{-1}$. For these experiments several solutions of BA in ethanol were produced ranging from $1.1 \times 10^{-6} \text{ M}$ to $1.14 \times 10^{-2} \text{ M}$ to determine the standard response curve on a batch of 3 #302 Klarite substrates. The substrate were drop coated with $20 \mu\text{L}$ of solution and allowed to air dry, followed by the collection of SERS spectra of 8 separate measurements from random locations across the surface. This was repeated for all concentrations.

Figure 4.5 show the SERS response of the substrates for the original substrates (triangles) and for the regenerated substrates (circles). As can be observed the sensitivity of the Klarite substrates, calculated in unit of SNR over pBA, is not compromised after the regeneration process but is instead improved, from 5 ± 2 to 13 ± 4 , for original and regenerated substrates, respectively. Such a behavior was ascribed to the measure of SERS from regenerated substrates happening after a short time interval from the deposition of the metallic film, whereas the original substrates were 1 to 6 years old (stored in vacuum sealed containers). SERS substrates are known to undergo a time dependent irreversible loss in enhancement due to changes in the fine surface roughness.²⁹ In addition to the sensitivity the substrate-to-substrate variation of original and regenerated substrates was calculated at 3 different

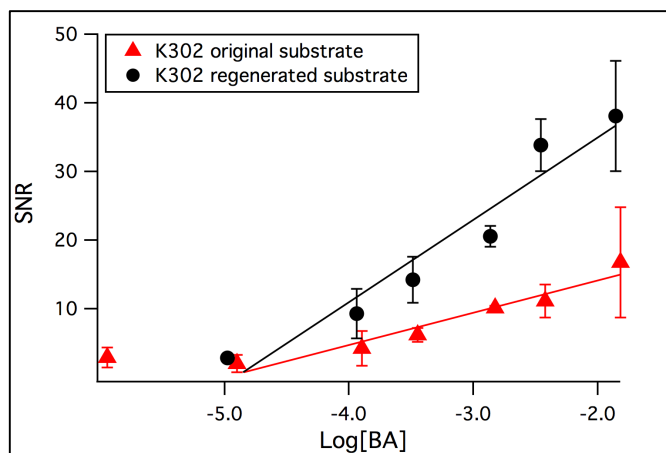


Figure 4.5. Logarithmic standard curves for the SERS detection of BA on Klarite substrates. Signal to noise for original substrates (triangles) and regenerated substrates (circles) was reported as a function of the logarithm of the concentration of BA. The data were fitted to a line to calculate the sensitivities, found to be of 5 ± 2 and 13 ± 4 for original and regenerated substrates, respectively, and in units of SNR/pBA (i.e., $-\log[\text{BA}]$). The data and fit relative to the original substrate are shown in red while that relative to the regenerated substrate are shown in black.

concentrations. The average response was observed to be of 14% and to be statistically identical between the original and regenerated substrates, confirming that the regeneration process does not significantly modify the substrate surface. The larger error observed in Figure 4.5 for the substrates drop coated with the BA solution at 10^{-2} M is likely due to BA clusters visible on the surface of the substrate.

To understand if the regeneration process could be repeated for multiple cycles, sensitivities and reproducibility of the substrates were measured after each regeneration, up to 4 cycles. The sensitivities of the Klarite substrates as a function of the regeneration cycles are shown in Figure 4.6a. The sensitivities from the regenerated substrates were observed to decrease as a function of the regeneration cycles after the initial increase, due to the fine structure of the metallic surface. However, the values for the first 3 cycles were

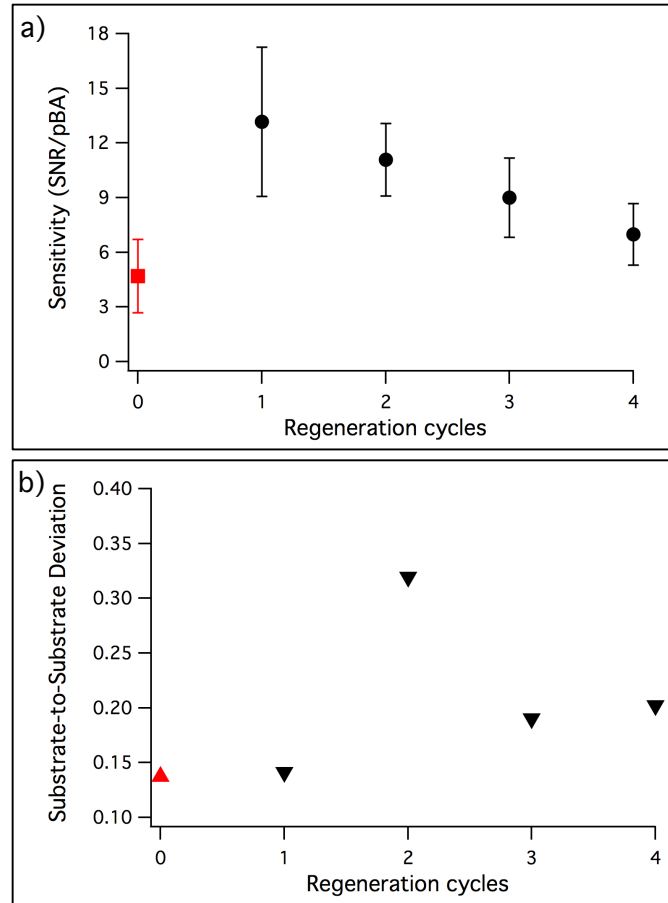


Figure 4.6. (a) Sensitivities of regenerated Klarite substrates as a function of number of regeneration cycles. **(b)** Substrate-to-substrate deviation of regenerated Klarite substrates as a function of number of regeneration cycles. The markers relative to the original substrate (0 regenerations) are shown in red.

observed to be statistically identical. While the regeneration was observed to reduce the sensitivity of the substrates, for the first 4 cycles the values obtained were greater than the initial sensitivity of the original substrate.

Figure 4.6b shows the substrate-to-substrate reproducibility as a function of the regeneration cycles. Although the deviations were observed to increase slowly as a function of regeneration cycles, their values were under 20% throughout the experiment with the exception of an outlier for 2 cycles. While such value may seem high, it has to be

considered that other than the variability between substrates, the reproducibility is also also influenced by the variability of the drop coating method, known to be far from optimal for species that do not chemisorb strongly on the metallic surface.

In conclusion, the sensing figures of merit were observed to degrade slowly as a function of the number of regenerations performed. However, after 4 regeneration cycles performed the sensitivity of the substrates was at least as good as the original and the deviation across the batch was only slightly increased. Table 4.1 reports the sensitivities and substrate-to-substrate deviation of 3 #302 Klarite substrates with respect to the regeneration cycle.

Table 4.1. Sensing figures of merit of Klarite substrates with respect to the regeneration cycle.

Regeneration cycle	Sensitivity	Substrate-to-substrate deviation
0	5±2	14%
1	13±4	14%
2	11±2	31%
3	9±2	19%
4	7±2	18%

Multi-layered enhanced substrates

Incorporating a multi-layered structure (metal-dielectric-metal) in a substrate has been shown to amplify the SERS signal from the substrate surface.^{13,26,30,31} To exploit this multi-layer enhancement in regenerated Klarite substrate, multi-layer structures were deposited on the substrates in place of a simple gold film. Such structures were fabricated with a

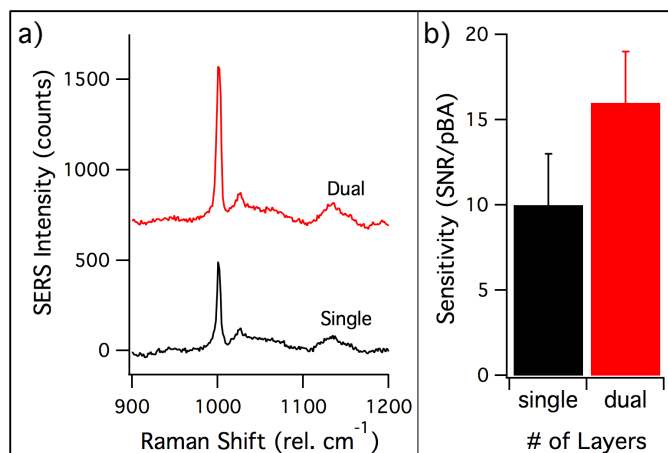


Figure 4.7. (a) SERS signal from 1002 rel. cm⁻¹ ring breathing mode of BA on a on a single layer regenerated Klarite substrate (single) and on a dual-layered Klarite substrate (dual). (b) Bar graph of the sensitivities for the detection of BA on single and dual-layered Klarite substrate.

procedure developed elsewhere by depositing thin gold films separated by an ultrathin TiO₂ spacer, grown with ALD.²⁶ Substrates composed by 2 gold layers, of 240 nm each, were compared to a conventional Klarite substrates. The substrates were drop coated with increasing concentrations of benzoic to study their sensitivity and SERS enhancement as for the previous section. The transition used for the calibration was the 1002 rel. cm⁻¹ ring breathing mode of BA. The signal of the band from a single layer substrate and a dual-layered Klarite substrates are reported in Figure 4.6a. As expected, the signal increases by using a dual-layered structure. The increase in sensitivity due to the multi-layer signal enhancement was also quantified. Figure 4.6b shows the sensitivities of the Klarite substrates, single and dual-layered. The sensitivity was observed to increase by applying a dual-layered structure to the substrates, from 10±3 to 16±3. These results show how by employing multi-layered structures is possible to further increase various figures of merit of Klarite substrates.

4.4 Conclusions

The ability to regenerate and amplify Klarite substrates was demonstrated herein. The substrates were regenerated by chemically stripping the original gold surface and depositing on the substrates a new gold film. SPR measurements suggest that the substrates surface characteristics are not varied by the regeneration process. The regenerated substrates showed sensitivities comparable with the initial Klarite substrates, with an additional increase in sensitivity due to irreversible degradation of SERS substrates over time. The sensitivities of regenerated substrates were observed to degrade as a function of regeneration cycle but to be conserved greater than the initial sensitivity for 4 regeneration cycles. The substrate-to-substrate reproducibility was also observed to slowly increase as a function of the regenerations. Finally, the application of multi-layered structures on regenerated Klarite substrates increased the signal-to-noise and sensitivities of the substrates, if compared to a single layered analogous. The overall results demonstrated the possibility to reuse disposable Klarite substrates, as well as to amplify the initial sensitivity and throughput of the substrates.

4.5 References

- (1) Fleischmann, M.; Hendra, P. J.; McQuillan, A. J. *Chemical Physics Letters* **1974**, *26*, 163.
- (2) Jeanmaire, D. L.; Van Duyne, R. P. *Journal of Electroanalytical Chemistry and Interfacial Electrochemistry* **1977**, *84*, 1.
- (3) Moskovits, M. *Reviews of Modern Physics* **1985**, *57*, 783.
- (4) Kelly, K. L.; Coronado, E.; Zhao, L. L.; Schatz, G. C. *The Journal of Physical Chemistry B* **2003**, *107*, 668.
- (5) Moskovits, M. *Journal of Raman Spectroscopy* **2005**, *36*, 485.
- (6) Strobbia, P.; Languirand, E.; Cullum, B. M. *Optical Engineering* **2015**, *54*, 100902.

- (7) Yuan, H.; Register, J.; Wang, H.-N.; Fales, A.; Liu, Y.; Vo-Dinh, T. *Analytical and Bioanalytical Chemistry* **2013**, *405*, 6165.
- (8) McNay, G.; Eustace, D.; Smith, W. E.; Faulds, K.; Graham, D. *Applied Spectroscopy* **2011**, *65*, 825.
- (9) Sharma, B.; Frontiera, R. R.; Henry, A.-I.; Ringe, E.; Van Duyne, R. P. *Materials Today* **2012**, *15*, 16.
- (10) Harper, M. M.; McKeating, K. S.; Faulds, K. *Physical Chemistry Chemical Physics* **2013**, *15*, 5312.
- (11) Kneipp, K.; Haka, A. S.; Kneipp, H.; Badizadegan, K.; Yoshizawa, N.; Boone, C.; Shafer-Peltier, K. E.; Motz, J. T.; Dasari, R. R.; Feld, M. S. *Applied Spectroscopy* **2002**, *56*, 150.
- (12) Orendorff, C. J.; Gearheart, L.; Jana, N. R.; Murphy, C. J. *Physical Chemistry Chemical Physics* **2006**, *8*, 165.
- (13) Li, H.; Cullum, B. M. *Applied Spectroscopy* **2005**, *59*, 410.
- (14) Gunnarsson, L.; Bjerneld, E. J.; Xu, H.; Petronis, S.; Kasemo, B.; Käll, M. *Applied Physics Letters* **2001**, *78*, 802.
- (15) Qin, L.; Zou, S.; Xue, C.; Atkinson, A.; Schatz, G. C.; Mirkin, C. A. *Proceedings of the National Academy of Sciences* **2006**, *103*, 13300.
- (16) Vo-Dinh, T.; Hiromoto, M. Y. K.; Begun, G. M.; Moody, R. L. *Analytical Chemistry* **1984**, *56*, 1667.
- (17) Farcau, C.; Astilean, S. *The Journal of Physical Chemistry C* **2010**, *114*, 11717.
- (18) Hulteen, J. C.; Treichel, D. A.; Smith, M. T.; Duval, M. L.; Jensen, T. R.; Van Duyne, R. P. *The Journal of Physical Chemistry B* **1999**, *103*, 3854.
- (19) Haynes, C. L.; Van Duyne, R. P. *The Journal of Physical Chemistry B* **2001**, *105*, 5599.
- (20) Klarite™ - Substrates for Surface Enhanced Raman Scattering. <http://resources.renishaw.com/en/details/klarite-datasheet--26857> (accessed 7/2/2015)
- (21) Qi, J.; Li, Y.; Yang, M.; Wu, Q.; Chen, Z.; Peng, J.; Liu, Y.; Wang, W.; Yu, X.; Sun, Q.; Xu, J. *Nanoscale Res. Lett.* **2013**, *8*, 495/1.
- (22) Tripathi, A.; Emmons, E. D.; Fountain, A. W.; Guicheteau, J. A.; Moskovits, M.; Christesen, S. D. *ACS Nano* **2015**, *9*, 584.
- (23) Stokes, R. J.; Macaskill, A.; Dougan, J. A.; Hargreaves, P. G.; Stanford, H. M.; Smith, W. E.; Faulds, K.; Graham, D. *Chem. Commun. (Cambridge, U. K.)* **2007**, 2811.
- (24) Kassu, A.; Robinson, P.; Sharma, A.; Ruffin, P. B.; Brantley, C.; Edwards, E. *Proc. SPIE* **2010**, *7764*, 77640Q/1.
- (25) Hackley, J. C.; Gougousi, T.; Demaree, J. D. *Journal of Applied Physics* **2007**, *102*, 034101.
- (26) Strobbia, P.; Henegar, A. J.; Gougousi, T.; Cullum, B. M. *Applied Spectroscopy* **2016**, (in press).
- (27) Wu, H.-Y.; Choi, C. J.; Cunningham, B. T. *Small* **2012**, *8*, 2878.
- (28) Sharma, B.; Fernanda Cardinal, M.; Kleinman, S. L.; Greeneltch, N. G.; Frontiera, R. R.; Blaber, M. G.; Schatz, G. C.; Van Duyne, R. P. *MRS Bulletin* **2013**, *38*, 615.
- (29) Dick, L. A.; McFarland, A. D.; Haynes, C. L.; Van Duyne, R. P. *The Journal of Physical Chemistry B* **2002**, *106*, 853.
- (30) Li, H.; Baum, C. E.; Sun, J.; Cullum, B. M. *Applied Spectroscopy* **2006**, *60*, 1377.

(31) Hankus, M. E.; Li, H.; Gibson, G. J.; Cullum, B. M. *Analytical Chemistry* **2006**, *78*, 7535.

Chapter 5:

Improving Sensitivity and Reproducibility of SERS Sensing in Micro-environments Using Individual, Optically Trapped SERS Probes

5.1 Introduction

Numerous nano- and submicron sensors capable of chemical measurement and imaging in a variety of environments have been developed.¹⁻³ Of these sensors, those based on surface enhanced Raman spectroscopy (SERS) offer several advantages over those employing other spectroscopic techniques, including being capable of: multiplexed detection of target species (due to the narrow spectral linewidth), molecular recognition (associated with vibrational spectroscopy), and extremely sensitive analysis.⁴⁻⁶ Despite these advantages, SERS sensors are not as commonly employed for real-world applications as other techniques (e.g., fluorescence) often due to issues with sensitivity and reproducibility.^{1,7}

One well-cited downfall of SERS sensing is the inherently weak Raman signals that must be enhanced. To achieve the required sensitivities for trace and ultratrace chemical analyses in many environments, sensors based on SERS require large enhancement factors (i.e., $> 10^6$) to amplify the Raman scatter over the background present. Several strategies have been applied to improve the sensitivity of SERS probes.⁸⁻¹³ Excellent results have been achieved with the development of SERS-active metal colloids. Enhancement factors obtainable with these aggregates produce SERS signals comparable to fluorescence, with

detection limits capable of single molecule detection.¹⁴⁻¹⁶ Unfortunately, colloids lack in reproducibility due to the random location and magnitude of the SERS “hot spots” generated.¹⁷

Probes based on isolated particles have also been developed, to obtain SERS sensing platforms with the reproducibility necessary for analytical applications. Due to the absence of nano-gaps between particles, alternative strategies are necessary to achieve comparable or even suitable signal enhancements for trace and ultra-trace analyses with individual particle-based probes. Several recent classes of individual particle-based probes provide increased SERS enhancement independent of aggregation, due to increased charge confinement at desired locations.¹⁸⁻²¹ Metal-dielectric-metal multi-layered structures have also shown enhanced SERS signals from individual particles/probes.²²⁻²⁶ In particular, probes based on this multi-layered geometry have shown enhancements in SERS signals of more than an order of magnitude²⁵ (compared to similar single layered metallic probes) providing the potential to further improve already advanced SERS structures such as nanostars and nanocrescents.²⁶

Large enhancement factors are important to obtain detectable signals in trace and ultra-trace analyses, where background Raman and fluorescence signals associated with major constituents in the local probe volume can cause significant interference or mask the SERS signal from the analyte of interest. Controlling the reproducibility and the location of the SERS signal enhancement is crucial. Many applications require spatially resolved mapping of the target analytes’ relative concentrations, which can be difficult to perform with

randomly distributed SERS probes exhibiting non-uniform SERS enhancement factors across the sample. One approach to overcome this limitation is to integrate the SERS measurement system with optical tweezers, thereby providing a means of probing the origin of the measured signal and its distribution. Early examples of combining optical tweezers and SERS focused on using the optical trap to aggregate multiple SERS active nanoparticles to achieve the enhancements necessary for detection of the trace amount of analyte present.^{27,28} While successful at providing improved enhancements, the randomness of the aggregation and “hot spot” formation in the optical trapping volume limited its applicability. Two groups have demonstrated the ability to measure SERS and surface enhanced resonance Raman scattering (SERRS) signals from individually trapped SERS active nanoparticles coated with SERRS active labels, demonstrating the potential for quantitative or semi-quantitative SERS imaging/mapping.^{29,30} However, in both of these cases, a separate higher power NIR laser was used for trapping, while a lower power visible laser was used for SERS excitation to prevent degradation or photobleaching of the SERS/SERRS nanoparticles and labels by the trapping beam.

Recent demonstration of the ability to generate stable optical traps for plasmonic nanoparticles of shapes and sizes ranging from a tens of nanometers to hundreds of nanometers using a low numerical aperture (NA) lens,³¹ such as those employed for typical SERS analyses, suggest the possibility to perform SERS probing and imaging analyses with a single beam for both trapping and probing. In this chapter, we demonstrate the use of just such a single, low power HeNe laser for the simultaneous trapping and probing of individual, several hundred nanometer diameter, SERS-active plasmonic particles and

quantify the significant improvements in analytical figures of merit achieved by such a system. While the size of the probes being trapped are almost two-fold larger than those previously trapped by Brzobohaty et. al. using low NA lens, this chapter demonstrates that it is possible to trap and manipulate these slightly larger plasmonic SERS probes to desired locations as is possible for smaller plasmonic particles. By employing a single laser beam for both trapping and probing SERS probes, the resulting SERS signals were improved by more than an order of magnitude compared to untrapped particles excited with the same laser power. This enhancement was accompanied by a simultaneous reduction of the variability in the resulting SERS signals to minimal levels. By employing SERS active probes on the same size scale as the optical trap, suppression of Raman background signals from the surrounding environment is achieved resulting in improved signal-to-background and signal-to-noise ratios.

5.2 Experimental

Materials

Mercaptobenzoic acid (MBA; Tokyo Chemical Industry) and ethyl alcohol 200 proof (Parmco-Aaper) were each used without further purification. Silica spheres were purchased from Bangs Laboratories as a suspension 10% w/w in water. The silver and gold utilized were purchased from Kurt J. Lesker as shots with dimensions < 4 mm and a purity of 99.99%. SERS measurements were all performed in glass cuvettes of 1 mm (model 1G1; Precision Cells Inc.).

Preparation of SERS Probes

Individual SERS probes were generated in a process similar to that used to produce SERS nanocrescents, in which a large majority of the sphere is coated with metal.²⁶ Glass microscope slides (VWR) were cut into uniform strips of 0.5×2.5 cm, cleaned in a RCA1 solution and subsequently in a 0.1 N HCl solution, then washed with distilled water followed by ethanol and air dried in an oven at 60° C. The silica sphere suspension was prepared by washing monodisperse silica spheres (390 nm diameter) several times with deionized water and 200-proof ethanol via multiple sonication and centrifugation cycles, before suspending them in 200-proof ethanol at a concentration of 2.2% w/w. A 10 μ L aliquot of the suspension was then drop coated onto a glass slide and air dried for 24 hours at 60°C to aid evaporation of the solvent.

Deposition of the metal film on the nanostructured surface was performed by mounting the drop-coated slides on a sample holder located 15 cm above the tungsten boat used for thermal evaporation in the physical vapor deposition system (Explorer 14; Denton Vacuum). To ensure even coating of the slides the sample holder was rotated during evaporation. A chamber pressure of 3×10^{-6} Torr was achieved prior to metal deposition. The metal thickness deposited was monitored with a quartz crystal microbalance (XTM/2 film thickness monitor; Inficon) and kept constant throughout the experiments at 125 nm (according to the QCM). The deposition rate was maintained as close as possible to 1.0 Å/s. Although the QCM thickness monitor estimates the metal thickness applied to be 125 nm, the overall size of the individual SERS probes is approximately 450 nm, as confirmed by SEM images of the spheres prior to removal from the microscope slide. This discrepancy between QCM measure and actual thickness is common for physical vapor

deposition systems and is due to the difference in position of the sample and the QCM relative to the metal source, as well as changes in QCM response over time. However, the use of QCM measurements allows for reproducible batches to be made over periods of several months, making it a convenient measure to use.

Following metal coating, individual coated spheres were obtained by carefully scraping the spheres off of the slide with an aluminum razor blade. The removed spheres were then dispersed in 1 mL of ethanol, sonicated for 15 min and then centrifuged and decanted to ensure separation into individual spheres. Verification of the individual nature of the spheres was confirmed via optical microscopy. To perform the SERS measurements the washed, coated spheres were dispersed in 250 μ L of MBA 10^{-4} M solution in ethanol, sonicated for 20 min and vortexed before being placed into a glass cuvette for measurement. Based on SERS measurements of the MBA bound to the surface of the metal coated spheres, SERS enhancement factors for the isolated (single metal layer) particles were estimated to be 1.3×10^6 , which is consistent with other individual SERS active particles, and corresponds to approximately an order of magnitude less enhancement than that observed from multi-particle arrays (i.e., 10^7) due to the absence of the “hot spots” generated at the interface between particles.³²

Multi-layer substrates were prepared with a procedure optimized elsewhere.²³ To fabricate the multi-layer structures, deposited silver films were left to oxidize in a closed Petri dish for 48 hours under ambient conditions to form a thin (i.e., monolayer) native oxide layer

prior to coating with each additional layer of silver. This process was then repeated multiple times depending on the number of layers desired.

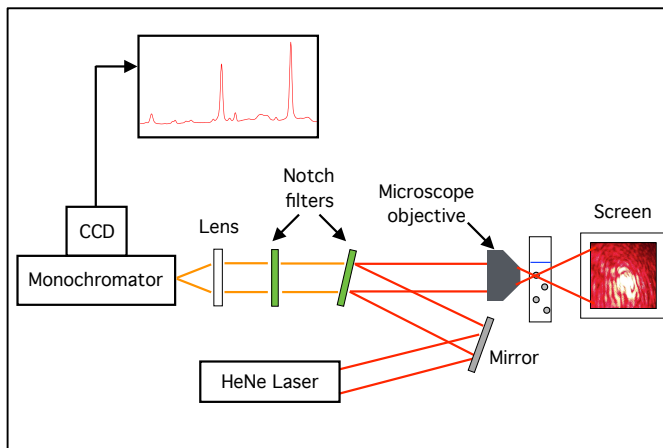


Figure 5.1. Schematic diagram depicting the SERS measurement system employed for optical trapping and SERS analyses.

Raman Measurement System

A 16 mW CW HeNe (632.8 nm) laser (JDS Uniphase) was used for excitation. The output of the laser was filtered with a bandpass filter to remove any plasma emission lines prior to being reflected off of a holographic notch filter (HNPF-632.8-1.0; Kaiser Optical Systems) onto a 10× objective (0.25 NA) that focused the laser into the center of the cuvette. The resulting backscattered light was collected by the same microscope objective and collimated prior to being filtered by the original notch filter and a second one (HNPF-632.8-1.0; Kaiser Optical Systems) to ensure complete rejection of the excitation light. This filtered light is then focused with an f/4 biconvex lens onto the slit of a 0.5 m spectrometer (Spectrapro 500i; Acton Research) with a spectral resolution of 10 cm^{-1} at 633 nm. The dispersed light was detected with a liquid nitrogen cooled charged coupled device (LN/CCD; Princeton Instruments). Control of the detection system was performed

using WinSpec 32 acquisition software (Roper Scientific) and the data was analyzed using Igor Pro 6.34A (WaveMetrics; see Macro A1 in Appendix A). A schematic diagram depicting this optical measurement configuration can be seen in Figure 5.1. To ensure constant optical alignment and calibration from day-to-day, spontaneous Raman spectra of neat toluene were taken each day.

5.3 Results and Discussion

Signal Stability

To quantify the increase in SERS signal stability and intensity from individual SERS active probes optically trapped in the focus of a low-power SERS excitation laser (as compared to multiple untrapped probes transiting through the total optical excitation volume), the SERS spectra of model chemical species chemisorbed on the surface of a probe were monitored. Probes for this study were fabricated from a single planar substrate and suspended in a 10^{-4} M solution of MBA in ethanol in a cuvette. A series of SERS spectra (100 ms exposure times) covering the fingerprint region were then obtained over time for both freely dispersed probes (Figure 5.2a) and a solution in which an individual probe had become optically trapped at the focus of the excitation beam (Figure 5.2b). Using a 16 mW HeNe laser for SERS excitation, enough laser fluence was present to capture individual 450 nm diameter SERS probes as they passed through the beam's focal point. Toggling between trapped and untrapped particles was performed for these measurements by temporarily blocking the laser beam, allowing the particle to escape the focus (i.e., the optical trap).

To monitor whether or not a probe was trapped, forward scatter from the sample was imaged onto a projection screen located approximately 33 cm beyond the cuvette (while the laser is focused in the center of the cuvette) and videos of the resulting scattered light were obtained. When a probe becomes trapped at the laser focus, a distinctly different and minimally varying optical scatter pattern is observed, compared to images associated with suspensions of randomly moving probes. In Figure 5.2c, a series of image frames from a video associated with no SERS probes being trapped is shown, revealing variability in intensity and spatial distribution of the optical scatter from frame-to-frame as probes pass through different points of the laser beam path. Alternatively, Figure 5.2d shows a series of video frames associated with a trapped particle, revealing a consistent and invariant image profile.

When a SERS active probe becomes optically trapped in the focus of the low power SERS excitation beam, both a significant increase in SERS signal as well as a decrease in SERS signal variability occurs. This difference can be seen in the time course series of SERS spectra of MBA chemisorbed on the probe(s) surface(s) for both suspensions of freely moving untrapped probes (Figure 5.2a) and the same concentration suspension of probes in which a single probe has been trapped at the focus of the sample excitation beam (Figure 5.2b). As can be seen from these spectra, the signal variance associated with the SERS bands of MBA is dramatically reduced when a probe becomes trapped. To quantify this signal stabilization effect, the relative standard deviation of the peak intensity for each

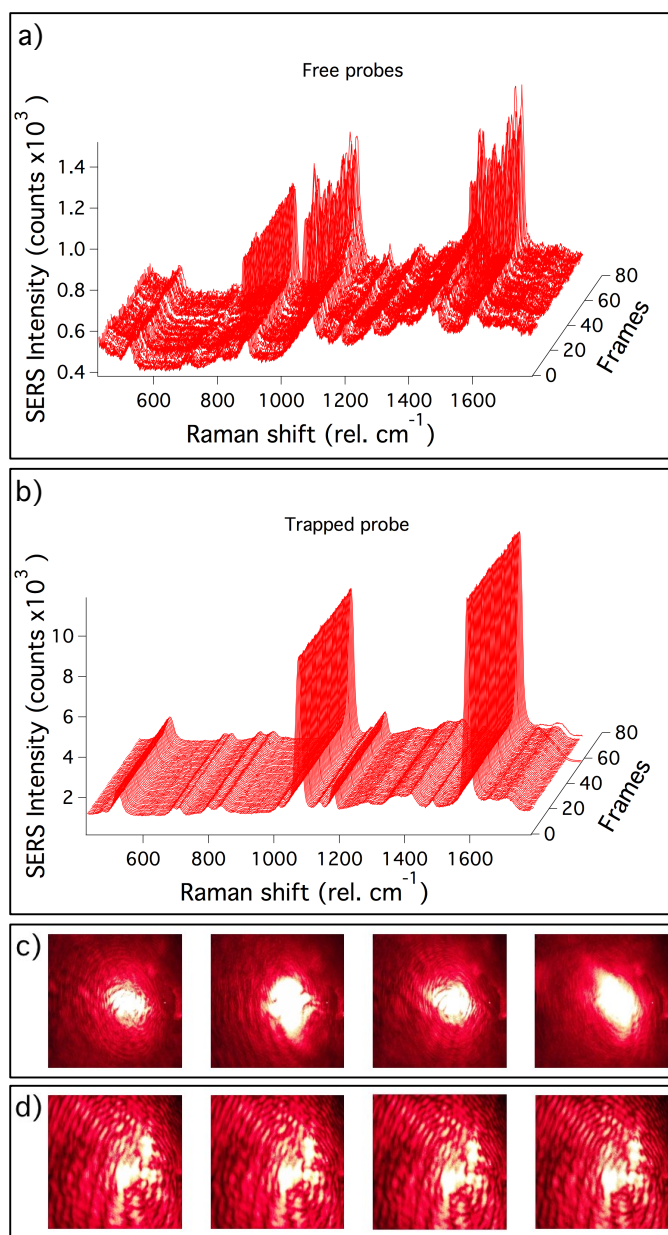


Figure 5.2. A sequential series of SERS spectra of MBA (exposure times 100 ms) demonstrating the evolution over time for (a) a suspension of freely moving single layer SERS probes and (b) the same suspension with a trapped single layer SERS probe. Images on the bottom represent a time evolution of the forward scatter image projected on a screen for (c) a suspension of freely moving SERS probes and (d) the same suspension with a trapped SERS probe.

ensemble of spectra were calculated for the most prominent peak in the MBA spectrum (i.e., $1588 \text{ rel. cm}^{-1}$; $\nu(\text{CC})_{\text{ring}}$).³³ The relative standard deviations for each of these two

ensembles were found to be 7×10^{-2} and 9×10^{-3} , respectively for the free suspension and the trapped probe, corresponding to nearly an order of magnitude reduction in signal variability for the trapped probes. Similar improvements in the relative standard deviations of the prominent $1075 \text{ rel. cm}^{-1}$ band of MBA are also observed with relative standard deviations of 6×10^{-2} and 1×10^{-2} , respectively, for the free suspension and the suspension with a single trapped probe.

This increased stabilization in SERS signal is attributed to the constant presence of the SERS active probe at the point of highest laser fluence during the entire signal acquisition time as opposed to the intermittent passing of multiple probes through the optical beam path at different locations and times. This attribution can be verified by comparing the relative standard deviations of the $1075 \text{ rel. cm}^{-1}$ SERS band of MBA chemisorbed to the SERS probes in the 10^{-4} M solution of MBA in ethanol to the relative standard deviation of the 880 rel. cm^{-1} spontaneous Raman band of ethanol in the spectra of Figure 5.2a (i.e., non-trapped analyses). Since ethanol is the solvent for the 10^{-4} M MBA solution and is always present in the optical probing volume at a nearly constant amount ($\approx 17 \text{ M}$), similar to the constant presence of the SERS probe in the optically trapped measurements, it is expected that the relative standard deviation of this signal should be approximately the same as that of the SERS signal from the trapped probes. In the case of the 880 rel. cm^{-1} spontaneous Raman band of ethanol, which is similar in average intensity to the $1075 \text{ rel. cm}^{-1}$ SERS band of MBA, the relative standard deviation was found to be 1×10^{-2} . This value is lower than the relative standard deviation of the non-trapped $1075 \text{ rel. cm}^{-1}$ SERS

band of MBA and statistically the same as the relative standard deviation of the 1075 rel. cm^{-1} band of MBA for the trapped particle (i.e., 1×10^{-2}).

Signal Enhancement and Background Suppression

In addition to a dramatic decrease in SERS signal variability by trapping an individual SERS active probe in the focus of the excitation beam, a significant increase in signal intensity and concomitant suppression of background signal occurs. This can be clearly seen in Figure 5.3, in which the SERS/Raman spectra of a 10^{-4} M MBA in ethanol solution are displayed, with (upper spectrum) and without (lower spectrum) an individual SERS probe being trapped. In both measurements, the concentration of SERS active probes was kept constant at 7.2×10^6 probes/ μL and spectral acquisition times of 500 ms were employed. In Figure 5.3a, a clear enhancement in the intensity of the SERS signals for MBA at 1588 rel. cm^{-1} and 1075 rel. cm^{-1} can be seen. The observed signal enhancement, or trapping enhancement, is defined as ratio of the MBA peak intensities of a trapped probe over those of the freely suspended probes and corresponds to a 12 ± 3 -fold improvement in signal intensity. This enhancement is based on signals of 7.6×10^4 counts and 6.2×10^3 counts associated with the 1588 rel. cm^{-1} band for the trapped and untrapped measurements, respectively. Comparable signal enhancements can also be seen for the 1075 rel. cm^{-1} band. Although calculation of a specific numerical value for this trapping enhancement factor

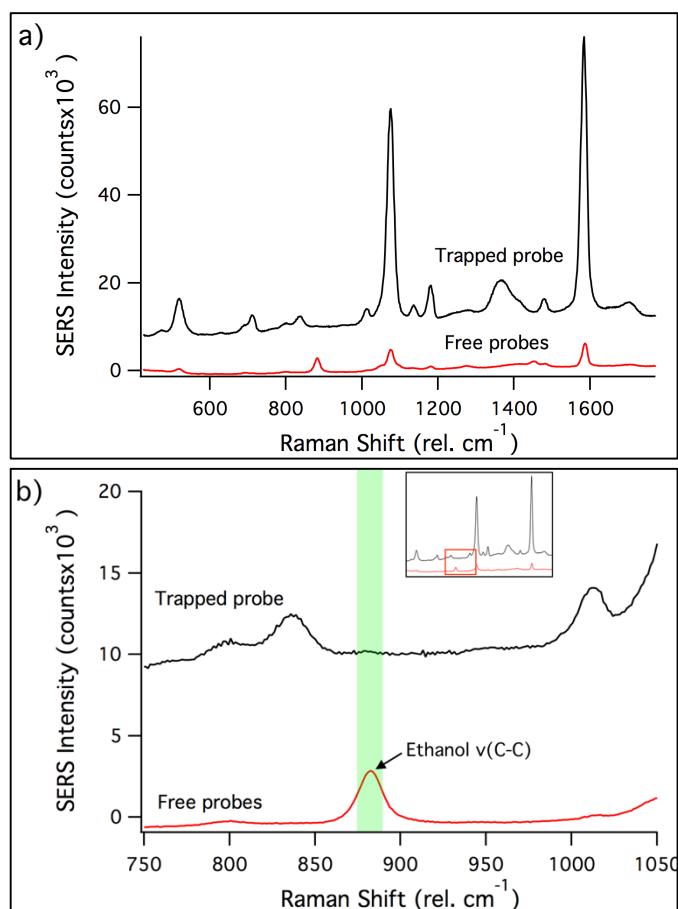


Figure 5.3. (a) SERS spectra of mercaptobenzoic acid obtained with a trapped single layer SERS probe (upper spectrum) and a freely moving suspension of single layer SERS probes (lower spectrum). (b) Raman spectra of 10^{-4} M MBA in ethanol solution with (upper spectrum) and without (lower spectrum) an individual SERS probe optically trapped at the focal point of the excitation optics. The shaded area highlights the location where the 880 cm^{-1} spontaneous Raman band of ethanol should appear. Inset shows entire Raman/SERS spectrum revealing the position of the highlighted region in the overall spectra. The spectra are not offset but reported with the increased baseline signal observed due to SERS enhancement and increased scattering.

has little explicit value, since it is dependent on the signal from the untrapped measurement and subsequently the probe concentration in solution. A clear improvement in signal intensity is seen simply by measuring an individual probe trapped at the focus of the SERS measurement beam, where the highest fluence occurs.

Because trapping of a probe in the measurement system's focus results in both improved signal intensity and decreased signal variability, significant signal-to-noise level improvements are achieved by trapping a single probe. Based on the 1588 rel. cm^{-1} band, a signal-to-noise ratio (S/N) improvement of 8-fold (S/N of 15 for untrapped and 116 for trapped measurements) is achieved by comparing the results from the ensemble measurements of trapped and untrapped probes excited with the same laser power. Although this improvement in S/N is slightly less than the signal intensity improvements, this disparity is not unexpected as the SERS shot noise scales with the increased signal from both the analyte and any SERS enhanced background.

Even more dramatic improvements in the signal-to-background (S/B) can be achieved by employing a SERS active probe approximately the same size (i.e., within an order of magnitude) as the focal spot of the excitation beam. This improvement in S/B can be particularly important when probing micro-environments with SERS, where minimal analyte (and correspondingly analyte signal) may be present with optical signals from other major species, as spontaneous Raman and fluorescence. By trapping the relatively large SERS active probes used in this work in the focal point of the excitation beam as opposed to smaller, traditional SERS-active nanoparticles or colloids, large volumes of the background species are excluded from the area of highest excitation power density, resulting in significant suppression of non-SERS background signals. This mechanism can be seen in Figure 5.3b, which shows a magnified view of the spectra in Figure 5.3a, focusing on the 750 – 1050 rel. cm^{-1} spectral range. An improvement in the S/N ratio of all of the bands, except the 880 rel. cm^{-1} band, is again observed for the spectrum in which a

SERS probe has been trapped (upper spectrum). However, when a probe is trapped, the 880 rel. cm^{-1} band (which corresponds to the spontaneous Raman signal from the ethanol solvent) is greatly diminished. This suppression of non-SERS backgrounds from major chemical constituents in the sample simply by displacement from the excitation focal point could prove invaluable when probing micro-environments where potential background autofluorescence or spontaneous Raman from major constituents (e.g., the solvent or medium) can dramatically hamper SERS analyses otherwise.

Concentration Studies

To ensure that signal enhancements observed were the result of trapping of an individual SERS probe and not aggregation of numerous particles, causing the formation of multiple “hot spots” and increased SERS enhancement factors, as has been seen in previous optical trapping SERS analyses with small colloidal nanoparticles,^{27,28} two different studies were performed. In the first of these studies, the trapping was calculated as a function of varying SERS probe concentration in the sample. SERS measurements of the 1588 rel. cm^{-1} band of a 10^{-4} M MBA solution were taken with different concentrations of SERS probes (i.e., 7.2×10^6 , 3.6×10^6 and 1.8×10^6 probes/ μL). To minimize any uncertainty associated with probe concentration, serial dilutions were made by first dispersing SERS probes extracted from a single planar substrate suspension and then diluting aliquots of this solution into 250 μL , 500 μL and 1000 μL volumes. The results of these analyses are shown in Figure 5.4a, in which 9 spectra were averaged for each of the trapped and non-trapped measurements and trapping enhancement was calculated. The data points in Figure 5.4a

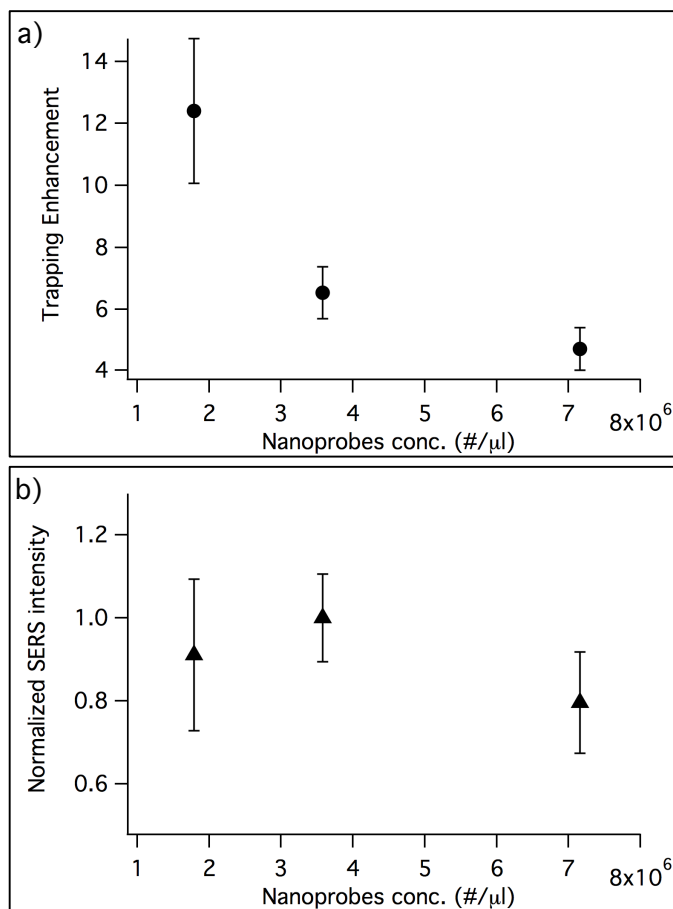


Figure 5.4. (a) Plot of trapping enhancement of the 1588 rel. cm^{-1} band of mercaptobenzoic acid as a function of SERS probe concentration. (b) Plot of the variation in SERS intensity at 1588 rel. cm^{-1} of a trapped probe as a function of concentration. Error bars represent a single standard deviation.

represent the average trapping enhancement calculated for each probe concentration and the error bars represent the standard deviation of these values.

As can be seen for Figure 5.4a, the trapping enhancement is greatest for the lowest concentration of SERS probes present and decreases with each increase in SERS probe concentration. When these results are compared to the average SERS intensity of the 1588 rel. cm^{-1} band of MBA for the trapped probe measurements versus SERS probe concentration (Figure 5.4b) it is apparent that this trapping enhancement is not due to

changes in the trapped signal intensities, but rather increases in SERS associated with the untrapped measurements as the SERS probe concentration increases. This observation is consistent with the concept that an individual probe is being trapped as opposed to aggregation of numerous probes, which would result in greater SERS signals with increasing probe concentration for the trapped measurements. Furthermore, with the size of the SERS probes being approximately 450 nm, no more than 1-2 probes could fit in the focal (i.e., trapping) volume. The variability in the average SERS signal at 1588 rel. cm^{-1} would be much larger than those measured in Figure 5.4b (i.e., 14% RSD) if different aggregates were responsible for the resulting SERS signals in the multiple trapped measurements performed. The step-wise increase and invariant nature of the 1588 rel. cm^{-1} SERS signal immediately following trapping also suggests no aggregation after trapping of a probe occurs.

Multi-layer Enhancement from Trapped Probes

While the dynamic signal enhancements and background suppression from optically trapping an individual SERS active probe in the focus of the same low power SERS excitation beam used for measurement represents a significant advance for probing micro-environments, this sensitivity can be further increased by incorporating multi-layered SERS probes.²³ As has been previously demonstrated,²³ the application of alternating layers of SERS active metal and dielectric can provide over an order of magnitude in SERS signal enhancement as compared to comparable single metallic layer SERS substrates, with the maximum enhancement achievable from this multi-layer geometry depending on the

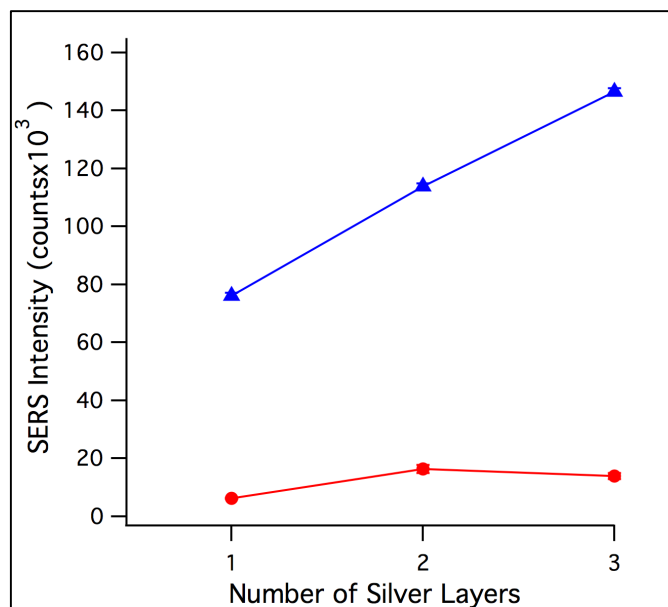


Figure 5.5. SERS intensity of the 1588 rel. cm^{-1} band of MBA as a function of the number of silver layers in multi-layered SERS probes for both trapped (triangles) and untrapped (circles) probes. Error bars for each average value represent the standard deviation in the measurements (most error bars are smaller than the markers denoting the average values).

number of layers and the thickness of each layer as well as the laser power used for excitation.²³ By optically trapping an individual SERS probe in the focal point of the excitation laser beam, the maximum excitation power density is experienced by the probe further improving the multi-layer enhancement of individual SERS probes by optically trapping. To characterize potential improvements in multi-layered SERS probe response by optically trapping in the focus of the excitation beam, a series of measurements were performed on SERS probes with different numbers of metal layers both in trapped and untrapped states. In such structures, each layer is isolated from another by a silver oxide dielectric layer. In all of these measurements, the SERS signal being measured corresponds to the 1588 rel. cm^{-1} band of a 10^{-4} M MBA solution in which SERS probes were maintained at a concentration of 7.2×10^6 probes/ μL .

The results from these measurements can be seen in Figure 5.5, with the triangles representing the average SERS intensity of the 1588 rel. cm^{-1} band from twenty measurements obtained with a single trapped probe (error bars represent a single standard deviation for an individual trapped probe) and the circles represent the SERS intensity of the 1588 rel. cm^{-1} band for untrapped probe measurements (20 measurements; error bars represent a single standard deviation of the measurements). Due to the highly reproducible nature of the SERS signal arising from a single trapped particle, the error bars associated with each of the data points in the trapped probe measurements are smaller than the individual markers denoting the average values. The relative standard deviation of the 1588 rel. cm^{-1} MBA band from 20 measurements of the same trapped particle is only 0.9%. This value is significantly better than the approximately 15% RSD associated with the same signal obtained using measurements taken with 20 different individually trapped particles (e.g., Figure 5.4b). This difference in RSD can be attributed to the particle-to-particle variability associated with multiple probes and demonstrates the significant improvements in SERS reproducibility that can be obtained by trapping and scanning a single probe thorough a sample for chemical mapping of micro-environments. Furthermore, this 0.9% RSD from a single trapped particle is also significantly than the 15% - 30% RSDs obtained from measuring different locations on an extended area of SERS substrates (i.e., metal film over nanostructure substrates like those used to generate the individual probes in this study), where the variability in such analyses arises from the particle-to-particle variability associated with different particles in contact with the sample.

As can be seen from comparison of the single layered substrate measurements (untrapped vs. trapped) in Figure 5.5, trapping results in approximately an order of magnitude improvement in signal intensity. By comparing the results from the single layered substrates to the dual-layered substrates enhancements between 1.4 – 2.0-fold can be achieved for both trapped and untrapped probes, consistent with the per layer enhancements previously reported for multi-layered SERS substrates. For the non-trapped probes which are freely passing through the excitation beam, the maximum multi-layer enhancement achievable plateaus at two layers, but it continues to increase with additional layers for the trapped probes. This further increase in SERS signal from MBA chemisorbed to the probe's surface is similar to excitation power dependent multi-layer enhancements observed.²³ While the exact multi-layer enhancement achievable will depend on the specific laser power employed for the trap/measurement system, the number of metal layers and the exact metal employed, these results demonstrate the ability to symbiotically improve native SERS enhancement factors of SERS probes by at least 24-fold simply by employing a multi-layer geometry in conjunction with optical trapping of the probe, even with only 16-mW laser excitation powers. This improvement of native SERS enhancement factors can be even further improved by applying more layers as well as employing a higher power excitation source for the analysis of interest.

5.4 Conclusions

Demonstration of the ability to use a single low power SERS excitation beam for the simultaneous optical trapping and excitation of individual SERS active probes has been performed revealing inherent signal amplification, improved signal stability and the ability

to dramatically suppress non-SERS optical backgrounds. Unlike previous colloidal-based SERS trapping measurements, no aggregation is necessary, resulting in dramatic improvements in signal reproducibility. In addition, the single beam system ensures trapping at the optimal excitation volume compared to dual-beam trap/probe geometries, resulting in greater signal strength and stability in most cases as well as greatly reduced instrumentation. The significant improvements in signal stability, signal amplification and background suppression achievable by optically trapping an individual SERS active probe in the focus of the same low power laser used for SERS excitation, offers a great deal of promise for accurately probing with minimal invasiveness chemical microenvironments (e.g., sealed environments, cells, etc.) that were previously inaccessible via techniques such as tip enhanced Raman spectroscopy (TERS). Although the laser beam used for trapping and probing must match the plasmon absorption band associated with the specific shape and size of the SERS probe employed to achieve a stable trap and efficient SERS signal enhancement, demonstration of the use of 632.8 nm light, which is good more many applications, has been shown. Combining the inherent signal amplification from optical trapping with a multi-layered probe geometry, a 24-fold improvement over the native SERS enhancement factor of the probes was demonstrated, with a potential for even more by increasing the number of metal layers employed and/or the laser power used. Furthermore, since both the multi-layer and optical trapping enhancements are largely independent of underlying particle structure, different shape probes with demonstrated large native SERS enhancement factors (e.g., nanostars, nanocrescents, etc.) could also be employed in such a measurement system. In addition, the low fluence necessary for

trapping is amenable for chemical mapping with highly reproducible SERS signal enhancements at every location simply by moving the individual probe to desired locations.

5.5 References

- (1) Ruedas-Rama, M. J.; Walters, J. D.; Orte, A.; Hall, E. A. H. *Analytica Chimica Acta* **2012**, *751*, 1.
- (2) Vitol, E. A.; Orynbayeva, Z.; Friedman, G.; Gogotsi, Y. *Journal of Raman Spectroscopy* **2012**, *43*, 817.
- (3) Yuan, H.; Register, J.; Wang, H.-N.; Fales, A.; Liu, Y.; Vo-Dinh, T. *Analytical and Bioanalytical Chemistry* **2013**, *405*, 6165.
- (4) Sirimuthu, N. M. S.; Syme, C. D.; Cooper, J. M. *Proc. SPIE* **2012**, 8234, 82340F.
- (5) Sun, J.; Hankus, M. E.; Cullum, B. M. *Proc. SPIE* **2009**, 7313, 73130K0.
- (6) Auchinvole, C. A. R.; Richardson, P.; McGuinness, C.; Mallikarjun, V.; Donaldson, K.; McNab, H.; Campbell, C. J. *ACS Nano* **2012**, *6*, 888.
- (7) Stender, A. S.; Marchuk, K.; Liu, C.; Sander, S.; Meyer, M. W.; Smith, E. A.; Neupane, B.; Wang, G.; Li, J.; Cheng, J.-X.; Huang, B.; Fang, N. *Chemical Reviews* **2013**, *113*, 2469.
- (8) Vo-Dinh, T.; Hiromoto, M. Y. K.; Begun, G. M.; Moody, R. L. *Analytical Chemistry* **1984**, *56*, 1667.
- (9) Driskell, J. D.; Shanmukh, S.; Liu, Y.; Chaney, S. B.; Tang, X. J.; Zhao, Y. P.; Dluhy, R. A. *The Journal of Physical Chemistry C* **2008**, *112*, 895.
- (10) Sharma, B.; Fernanda Cardinal, M.; Kleinman, S. L.; Greeneltch, N. G.; Frontiera, R. R.; Blaber, M. G.; Schatz, G. C.; Van Duyne, R. P. *MRS Bulletin* **2013**, *38*, 615.
- (11) Graham, D.; Thompson, D. G.; Smith, W. E.; Faulds, K. *Nature Nanotechnology* **2008**, *3*, 548.
- (12) Lee, C. H.; Hankus, M. E.; Tian, L.; Pellegrino, P. M.; Singamaneni, S. *Analytical Chemistry* **2011**, *83*, 8953.
- (13) Strobbia, P.; Languirand, E.; Cullum, B. M. *Optical Engineering* **2015**, *54*, 100902.
- (14) Kneipp, K.; Wang, Y.; Kneipp, H.; Perelman, L. T.; Itzkan, I.; Dasari, R. R.; Feld, M. S. *Physical Review Letters* **1997**, *78*, 1667.
- (15) Kneipp, K.; Kneipp, H. *Applied Spectroscopy* **2006**, *60*, 322A.
- (16) Nie, S.; Emory, S. R. *Science* **1997**, *275*, 1102.
- (17) Kneipp, K.; Haka, A. S.; Kneipp, H.; Badizadegan, K.; Yoshizawa, N.; Boone, C.; Shafer-Peltier, K. E.; Motz, J. T.; Dasari, R. R.; Feld, M. S. *Applied Spectroscopy* **2002**, *56*, 150.
- (18) Houry, C. G.; Vo-Dinh, T. *The Journal of Physical Chemistry C* **2008**, *112*, 18849.
- (19) Yuan, H.; Fales, A. M.; Houry, C. G.; Liu, J.; Vo-Dinh, T. *Journal of Raman Spectroscopy* **2013**, *44*, 234.
- (20) Talley, C. E.; Jackson, J. B.; Oubre, C.; Grady, N. K.; Hollars, C. W.; Lane, S. M.; Huser, T. R.; Nordlander, P.; Halas, N. J. *Nano Letters* **2005**, *5*, 1569.
- (21) Lu, Y.; Liu, G. L.; Kim, J.; Mejia, Y. X.; Lee, L. P. *Nano Letters* **2005**, *5*, 119.
- (22) Leverette, C. L.; Shubert, V. A.; Wade, T. L.; Varazo, K.; Dluhy, R. A. *The Journal of Physical Chemistry B* **2002**, *106*, 8747.

- (23) Li, H.; Cullum, B. M. *Applied Spectroscopy* **2005**, *59*, 410.
- (24) Li, H.; Baum, C. E.; Sun, J.; Cullum, B. M. *Proc. SPIE* **2006**, 6218, 6218041.
- (25) Li, H.; Baum, C. E.; Sun, J.; Cullum, B. M. *Applied Spectroscopy* **2006**, *60*, 1377.
- (26) Cullum, B. M.; Li, H.; Hankus, M. E.; Schiza, M. V. *NanoBiotechnology* **2007**, *3*, 1.
- (27) Svedberg, F.; Li, Z.; Xu, H.; Käll, M. *Nano Letters* **2006**, *6*, 2639.
- (28) Tong, L.; Righini, M.; Gonzalez, M. U.; Quidant, R.; Kall, M. *Lab on a Chip* **2009**, *9*, 193.
- (29) McNay, G.; Docherty, F. T.; Graham, D.; Smith, W. E.; Jordan, P.; Padgett, M.; Leach, J.; Sinclair, G.; Monaghan, P. B.; Cooper, J. M. *Angewandte Chemie International Edition* **2004**, *43*, 2512.
- (30) Stetciura, I. Y.; Yashchenok, A.; Masic, A.; Lyubin, E. V.; Inozemtseva, O. A.; Drozdova, M. G.; Markvichova, E. A.; Khlebtsov, B. N.; Fedyanin, A. A.; Sukhorukov, G. B.; Gorin, D. A.; Volodkin, D. *Analyst* **2015**, *140*, 4981.
- (31) Brzobohatý, O.; Šiler, M.; Trojek, J.; Chvátal, L.; Karásek, V.; Paták, A.; Pokorná, Z.; Mika, F.; Zemánek, P. *Scientific Reports* **2015**, *5*, 8106.
- (32) Duyne, R. P. V.; Hulteen, J. C.; Treichel, D. A. *Journal of Chemical Physics* **1993**, *99*, 2101
- (33) Michota, A.; Bukowska, J. *Journal of Raman Spectroscopy* **2003**, *34*, 21.

Chapter 6:

Conclusions and Future Perspectives

6.1 Conclusions

The development of surface enhanced Raman scattering (SERS)-based sensing platforms for real world applications will allow for the intrinsic and simultaneous detection of multiple analytes, among other advantages. However, to achieve such a goal, SERS substrates with throughput and reproducibility comparable to currently used optical sensors (e.g., fluorescence sensors) have to be developed. To this end, many strategies have been explored by numerous research groups.¹⁻⁴

Our lab discovered a metal-dielectric multi-layered geometry that permits for the amplification of the SERS signal on its outermost metallic surface (i.e., multi-layer enhancement). Such strategy offers the advantage of not relying on modification of its outer surface to produce the amplification, making it possible to enhance the sensitivity of a previously developed sensor without disrupting its reproducibility. The focus of this thesis was on the optimization and application of these structures, to be able to fabricate substrates with the SERS signal required for real-world applications.

The influence of the spacer layer on the multi-layer enhancement was characterized, allowing for the design of optimal multi-layered structures. The properties of the spacer layer used in multi-layered structures have been previously linked to the enhancement

observed,^{5,6} however, due to the techniques used to fabricate the spacers, it was not possible completely elucidate on the spacer influence. Recently, the use of atomic layer deposition has allowed the precise deposition of dielectric materials of different composition and thickness as spacers in multi-layered structures.

In Chapter 2, the nominal thickness of the spacer was observed to influence the multi-layered enhancement differently, depending on the characteristics of the spacer. The enhancement was observed to increase at thicknesses smaller than a monolayer of material. This behavior was demonstrated to be dependent on an increase surface coverage of the spacer, which caused a larger region of the structure to be of multi-layer nature. For thicknesses below this value the multi-enhancement was observed to exponentially decrease as a function of thickness, due to the loss of interaction between proximal metallic films. The sum of these behaviors generates the complete non-monotonic dependence of these structures.

In Chapter 3, the material used a spacer was also observed to influence the multi-layer enhancement. TiO_2 , HfO_2 , Al_2O_3 and Ag_2O were studied as spacer materials to isolate trends in bulk physical properties (Schottky barrier height, interface potential and dielectric constant), which were hypothesized to influence the multi-layer enhancement. While Schottky barrier height and interface potential showed very low correlation between the trend in physical properties and the expected effect on the multi-layer enhancement, the dielectric constants of the materials were able to predict the trend observed in enhancements of multi-layered structures of different compositions.

The studies over the thickness and material dependence of multi-layered structures allow for the design of optimal structures. From the thickness dependence studies it was found that the spacer that gives the highest enhancement is the thinnest possible coalescent film, while in the material dependence experiments it was found that materials with low dielectric constant are better spacer than high dielectric materials. Thereby, an optimal spacer for multi-layered structures has to simultaneously be coalescent, ultrathin and composed of a low dielectric constant material.

Additionally, the multi-layered structures were applied to diametrical opposite SERS substrates with positive results. The first application was on commercial SERS substrates based on an array geometry in Chapter 4. These single-use substrates were successfully regenerated with a single layer and dual-layered geometry, showing the expected multi-layer enhancement. The multi-layer geometry was also applied to single SERS nanoprobe dispersed in a liquid medium in Chapter 5. These probes were trapped to stabilize the SERS signal, as well as reducing the background signal. Also for this system, multi-layered probes were observed have larger SERS signals with respect to a single layer. Furthermore, trapping of single probes was also observed to increase the maximum number of layers applicable to the multi-layered structures. In conclusions, such structures were shown to successfully amplify SERS in different systems, suggesting the possibility of their use in potentially any SERS sensor.

6.2 Future Perspectives

The studies on spacer layers showed that low dielectric constant materials are optimal spacer for multi-layered structures. SiO₂ is an oxide with a relatively low dielectric constant (i.e., 3.9)⁷ and could be a strong candidate for the fabrication of optimal multi-layered structures. However, the atomic layer deposition of this material is challenging due to the reactivity of its precursors. Chemical deposition of SiO₂ has been extensively studied,⁸⁻¹⁰ however, the requirement of the film to be coalescent could be an issue at the thicknesses commonly employed in multi-layered structures. A possible future effort in the fabrication of optimal multi-layered structures could be on the chemical growth (in a lab setting) of ultrathin and coalescent SiO₂ films. This process would not only allow for the fabrication of optimal highly efficient multi-layered structures but it would also enable the fabrication of multi-layered structures in a scalable manner.

Currently, the hypothesis of mechanism for the multi-layer enhancement has not been completely elucidated. The studies on the spacer thickness and material dependence of this enhancement agree with the current hypothesis, which consists in interacting surface plasmon from proximal metallic films. However, to confirm this hypothesis a combination of experimental and computational studies have to be performed. These studies should focus on understanding which are the interacting elements in these structures (i.e., the whole films or the features composing its nanometric roughness); computationally simulating the identified plasmonic system; and confirming the origin of the observed enhancement by comparing experimental and computational results on multi-layered structures.

Finally, the multi-layered structures could be applied to non-canonical plasmonic materials, to increase their applicability. As an example, aluminum has been previously used as a material to fabricate substrates for UV-SERS.^{11,12} While these structures were predicted theoretically to yield enhancement larger than canonical plasmonic materials, the observed enhancements were orders of magnitude lower than what observed in analogous gold and silver structures.¹² This contrast between theory and experiment was due to the ubiquitous oxide film that cover aluminum surfaces. The use of multi-layered aluminum structures could be used to amplify the enhancement obtained and render such structures useful for sensing purposes, allowing for SERS structures to work in the UV, which is not possible with gold and silver substrate. Furthermore, the oxide film formed on aluminum surfaces could be used as spacer in multi-layered structures, similarly to the fabrication of Ag₂O multi-layered structures.

6.3 References

- (1) Strobbia, P.; Languirand, E.; Cullum, B. M. *Optical Engineering* **2015**, *54*, 100902.
- (2) McNay, G.; Eustace, D.; Smith, W. E.; Faulds, K.; Graham, D. *Applied Spectroscopy* **2011**, *65*, 825.
- (3) Banholzer, M. J.; Millstone, J. E.; Qin, L.; Mirkin, C. A. *Chemical Society Reviews* **2008**, *37*, 885.
- (4) Sharma, B.; Frontiera, R. R.; Henry, A.-I.; Ringe, E.; Van Duyne, R. P. *Materials Today* **2012**, *15*, 16.
- (5) Culha, M.; Cullum, B.; Lavrik, N.; Klutse, C. K. *Journal of Nanotechnology* **2012**, *2012*, 15.
- (6) Li, H.; Baum, C. E.; Sun, J.; Cullum, B. M. *Applied Spectroscopy* **2006**, *60*, 1377.
- (7) Robertson, J. *The European Physical Journal - Applied Physics* **2004**, *28*, 265.
- (8) Oldenburg, S. J.; Averitt, R. D.; Westcott, S. L.; Halas, N. J. *Chemical Physics Letters* **1998**, *288*, 243.
- (9) Prodan, E.; Radloff, C.; Halas, N. J.; Nordlander, P. *Science* **2003**, *302*, 419.
- (10) Liz-Marzán, L. M.; Giersig, M.; Mulvaney, P. *Langmuir* **1996**, *12*, 4329.

- (11) Chan, G. H.; Zhao, J.; Schatz, G. C.; Duyne, R. P. V. *The Journal of Physical Chemistry C* **2008**, *112*, 13958.
- (12) Jha, S. K.; Ahmed, Z.; Agio, M.; Ekinici, Y.; Löffler, J. F. *Journal of the American Chemical Society* **2012**, *134*, 1966.

Appendix A:

Igor Pro Macros

Macro A1

This macro was used to load a series of spectra taken with Winspec32 or SpectraSuite (saved as *.txt files) into a 3D matrix of Igor Pro. The files have to be sequentially numbered to be inputted in the matrix as different layers. Upon initialization, the macro asks for the folder in which the files are found, followed by a dialog window in which have to be inputted the basic name of the files (without the numbers), the initial and final number, the length of the spectrum file, and the basic name for the matrix. Additionally, each layer of the matrix is also saved a single wave and an average spectrum is also outputted. This macro allows for the manipulation of large ensembles of spectra as single matrices, which simplify calculations of average signals and standard deviations.

```

#pragma rtGlobals=3 // Use modern global access method and strict wave access.
Macro Ave_Film2D(inBName,numstart, numend,outBName,numpoints) //takes ASCII files and average them
String inBName //useful for repetitive measurements t
Variable numstart=1
Variable numend=2
Variable numpoints=1
String outBName
Prompt inBName, "Base Name of Input files" //file names (have to be sequential)
Prompt numstart, "Number of First file"
Prompt numend, "Number of Final file" //name of final wave to which will be added the suffix 'ave'
Prompt numpoints, "Number of Points"
Prompt outBName, "Base Name of Output wave"
Variable i=numstart
Variable j=numstart
Variable k=numstart+1
Variable l=0
String Name=""
String Name2=""
Do
Name=InBName+num2istr(i)+".txt" //Check the name and change here
print name
loadwave/P=Film/A/J/K=1 name //load the file
duplicate/o wave1 $(outBName+"_"+num2istr(i)) //duplicate the wave loaded with sequentially
killwaves wave0 wave1 //kill the waves loaded but not useful to clear
i+=1
While (i<=numend)
make/O/N=(numpoints) $(outBName+"ave") wave0 //make a wave called "name"ave and a wave0
wave0 = $(outBName+"_"+num2istr(numstart)) //make the first wave from file be this wave
Do
wave0 = ($(outBName+"_"+num2istr(k)) + wave0
k+=1
While (k<=numend) //sum all the waves in this new wave0
wave0=wave0/(numend-numstart+1) //divide the sum of all the waves by the nu
duplicate/o wave0 $(outBName+"ave") //give to the ave0 a name -> "name"ave
//display $(outBName+"ave") //show you the results
killwaves wave0

Do
make/o/n=(numpoints,numend) $(OutBName) //make a matrix large enough to be occupied by
$OutBName [] [l]= $(outBName+"_"+num2istr(j)) [p] //sequentially fill the matrix with the waves f
l+=1
j+=1
While (j<=numend) //pratically Film2D.ipf
//NewWaterfall $(OutBName) //display the matrix in a pseudo-3D plot
End

```

Macro A2

This macro was used to calculate the average signal and standard deviation from an ensemble of spectra included in a matrix (see macro A.1). Upon initialization, the macro asks for the name for an output wave, the name of the input matrix containing the spectra, value at which the peak in analysis is found, the range of frames to analyze, and the dimension of the boxcar for averaging on the wavelength as well (optional, input 0 to avoid averaging). The macro effectively makes a new wave that corresponds to a slice of the matrix perpendicular to the spectra plotting axis. Although this operation may look easy, the math language on which Igor Pro is based, which is purely designed for plotting purposes, make this operation require multiple steps that can be automated in “while” loops.

```

#pragma rtGlobals=1 // Use modern global access method.
Macro Affettare (outName, inName, boxcar, frames, numpeak) //takes a matrix made with repetitive me:
String inName //and calculates the STDEV of a peak as well as the av
String outName
Variable numpeak=1 //to make this progrm work is needed a matrix with the
Variable frames=2
Variable boxcar=3
Prompt outName, "Output name"
Prompt inName, "Input matrix"
Prompt frames, "Number of frames"
Prompt boxcar, "Boxcar width (each side)" //it doubles the value of this variable to be used as boxcar range
Prompt numpeak, "Peak point"
String name
name= "name"
Variable i=0
Variable k=0
Make/O/N=(frames) slice //makes a new wave to be used to calculate the stdv
If (boxcar== 0) //if you don't want the boxcar you can use a monodimensiona
  Make/O/N=(frames) slice //makes a new wave to be used to calculate the stdv
  slice= $inName [numpeak] [p] //makes this wave sequentially equal to values at a certain p
  Wavestats slice //take some parameters for this wave (including stdv)
  Make/O/N=1 $outName //new wave to print the output in
  $outName=V_sdev //copy the stdv in the new wave
  Print V_sdev //print outcome
  Killwaves slice //w/o boxcar it takes the peaks values and put tem in a wave of which it calculates the s
Else
  Do
  Make/O/N=(2*boxcar+1) $(name+num2istr(i)) //make a wave as large as the 2 times the
  Do
  $(name+num2istr(i)) [k] = $inName [(numpeak+k-boxcar)] [i] //fill this wave with the values
  k+=1
  While (k<= 2*boxcar)
  k=0
  wavestats $(name+num2istr(i)) //take some parameters for this w
  slice [i]= V_avg //copy the average of this boxcar
  Killwaves $(name+num2istr(i)) //kill not useful anymore waves
  i+=1
  While (i<=frames) //it takes the n points around the peak make a wave,
  Wavestats slice //take the average of the wave and make another wave with all the averages for each
  Make/O/N=1 $outName //then it calculates the sdev
  $outName=V_sdev
  Print "average=", V_avg //average result
  Print "STDEV=", V_sdev //stdv result
  Killwaves slice
Endif

```

Macro A3

This macro was used to calculate the average signal-to-noise ratio and standard deviation from an ensemble of spectra (see macro A.1). This macro is a modification from Macro A2 and was used to calculate the signal-to-noise ratio rather than the SERS signal. This modification was required in the Klarite regeneration project, which was in collaboration with the Army Research Lab, as that was the way substrates were characterized by the collaborators in the project. In addition to the previously required input, the macro asks for where to subtract the background from (as the signal-to-noise have to be calculated from the mere peak height), and which region to use to calculate the noise. For each slice of the matrix, the macro duplicates the region selected to calculate the noise and levels it around 0 to calculate the noise, followed by calculating the signal to noise as the ratio of peak height over the calculated noise. To note, the option of boxcar averaging was removed in this macro due to the spectra of the Klarite substrates not requiring it.

```

#pragma rtGlobals=1 // Use modern global access method.
Macro Affettare_Klarite_lev (outName, inName, R1, R2, frames, numpeak, BKGsub) //takes a matrix ma
String inName //and calculates the STDEV of a peak as well as the ave
String outName
Variable numpeak=1 //to make this progrm work is needed a matrix with
// (output procedure film2d.i

Variable frames=2
Variable boxcar=3
Variable R1 = 100
Variable R2 = 200
Variable BKGsub = 4
Prompt outName, "Output name"
Prompt inName, "Input matrix"
Prompt frames, "Number of frames"
Prompt numpeak, "Peak point"
Prompt R1, "Where is the noise calculated?"
Prompt BKGsub, "Where is the BKG subtracted from?"
Prompt R2, " "
Variable i=0
Make/O/N=(frames) slice //makes a new wave to be used to calculate the stdv and ave
Do
make/o/n=3000 wavex
wavex = $inName [p] [i]
Duplicate/o/R = [R1, R2] wavex noise //duplicate the region where the noise is calcul
CurveFit/NTHR=0 line noise /D //fit the region with a line to remove any drift
noise = noise - (W_coef[0]+W_coef[1]*x) //levele the region around 0 to measure only the noise, o
wavestats noise
slice [i] = (wavex [numpeak] - wavex [BKGsub])/V_sdev
//slice [i] = (wavex [numpeak] - V_avg)/V_sdev //variation for subtraction of peak
//is calculated

killwaves noise
i = i+1
While (i<=(frames-1))
Wavestats slice //take statistical parameters for this wave (including stdv)
Duplicate/o slice $OutName
Print "average=", V_avg //average result
Print "STDEV=", V_sdev //stdv result
Killwaves slice

```

Bibliography:

- (1) Klarite™ - Substrates for Surface Enhanced Raman Scattering.
<http://resources.renishaw.com/en/details/klarite-datasheet--26857> (accessed 7/2/2015)
- (2) Albrecht, M. G.; Creighton, J. A. *Journal of the American Chemical Society* 1977, 99, 5215.
- (3) Atwater, H. A. *Scientific American* 2007, 296, 56.
- (4) Auchincloss, C. A. R.; Richardson, P.; McGuinness, C.; Mallikarjun, V.; Donaldson, K.; McNab, H.; Campbell, C. J. *ACS Nano* 2012, 6, 888.
- (5) Banholzer, M. J.; Millstone, J. E.; Qin, L.; Mirkin, C. A. *Chemical Society Reviews* 2008, 37, 885.
- (6) Bao, L.; Mahurin, S. M.; Dai, S. *Analytical Chemistry* 2004, 76, 4531.
- (7) Bao, L.; Mahurin, S. M.; Dai, S. *Analytical Chemistry* 2004, 76, 4531.
- (8) Bardhan, R.; Mukherjee, S.; Mirin, N. A.; Levit, S. D.; Nordlander, P.; Halas, N. J. *The Journal of Physical Chemistry C* 2010, 114, 7378.
- (9) Biener, M. M.; Biener, J.; Wichmann, A.; Wittstock, A.; Baumann, T. F.; Bäumer, M.; Hamza, A. V. *Nano Letters* 2011, 11, 3085.
- (10) Brongersma, M. L.; Halas, N. J.; Nordlander, P. *Nat Nano* 2015, 10, 25.
- (11) Brongersma, M. L.; Hartman, J. W.; Atwater, H. H. *MRS Online Proceedings Library* 1999, 582.
- (12) Brzobohatý, O.; Šiler, M.; Trojek, J.; Chvátal, L.; Karásek, V.; Paták, A.; Pokorná, Z.; Mika, F.; Zemánek, P. *Scientific Reports* 2015, 5, 8106.
- (13) Chae, J.; Lahiri, B.; Kohoutek, J.; Holland, G.; Lezec, H.; Centrone, A. *Optics Express* 2015, 23, 25912.
- (14) Chan, G. H.; Zhao, J.; Schatz, G. C.; Duyne, R. P. V. *The Journal of Physical Chemistry C* 2008, 112, 13958.
- (15) Chaney, S. B.; Shanmukh, S.; Dluhy, R. A.; Zhao, Y. P. *Applied Physics Letters* 2005, 87, 031908/1.
- (16) Clavero, C. *Nature Photonics* 2014, 8, 95.
- (17) Culha, M.; Cullum, B.; Lavrik, N.; Klutse, C. K. *Journal of Nanotechnology* 2012, 2012, 15.
- (18) Cullum, B. M.; Li, H.; Hankus, M. E.; Schiza, M. V. *NanoBiotechnology* 2007, 3, 1.
- (19) Dick, L. A.; McFarland, A. D.; Haynes, C. L.; Van Duyne, R. P. *The Journal of Physical Chemistry B* 2002, 106, 853.
- (20) Ding, T.; Sigle, D. O.; Herrmann, L. O.; Wolverson, D.; Baumberg, J. J. *ACS Applied Materials & Interfaces* 2014, 6, 17358.
- (21) Doering, W. E.; Nie, S. *The Journal of Physical Chemistry B* 2002, 106, 311.
- (22) Driskell, J. D.; Shanmukh, S.; Liu, Y.; Chaney, S. B.; Tang, X. J.; Zhao, Y. P.; Dluhy, R. A. *The Journal of Physical Chemistry C* 2008, 112, 895.
- (23) Elghanian, R.; Storhoff, J. J.; Mucic, R. C.; Letsinger, R. L.; Mirkin, C. A. *Science* 1997, 277, 1078.
- (24) Eustis, S.; El-Sayed, M. A. *Journal of Applied Physics* 2006, 100, 044324.
- (25) Farcu, C.; Astilean, S. *The Journal of Physical Chemistry C* 2010, 114, 11717.
- (26) Ferguson, J. D.; Yoder, A. R.; Weimer, A. W.; George, S. M. *Applied Surface Science* 2004, 226, 393.

- (27) Fleischmann, M.; Hendra, P. J.; McQuillan, A. J. *Chemical Physics Letters* 1974, 26, 163.
- (28) Fraire, J. C.; Pérez, L. A.; Coronado, E. A. *The Journal of Physical Chemistry C* 2013, 117, 23090.
- (29) Gans, R. *Annalen der Physik* 1915, 352, 270.
- (30) Gardiner, D. J. In *Practical Raman Spectroscopy*; Gardiner, D. J., Graves, P. R., Eds.; Springer Berlin Heidelberg: Berlin, Heidelberg, 1989, p 1.
- (31) Gerrard, D. L.; Birnie, J. *Analytical Chemistry* 1990, 62, 140R.
- (32) Gerrard, D. L.; Bowley, H. J. *Analytical Chemistry* 1988, 60, 368R.
- (33) Gersten, J.; Nitzan, A. *Journal of Chemical Physics* 1980, 73, 3023.
- (34) Gersten, J. I. *Journal of Chemical Physics* 1980, 72, 5779.
- (35) Graham, D.; Thompson, D. G.; Smith, W. E.; Faulds, K. *Nature Nanotechnology* 2008, 3, 548.
- (36) Greeneltch, N. G.; Blaber, M. G.; Henry, A.-I.; Schatz, G. C.; Van Duyne, R. P. *Analytical Chemistry* 2013, 85, 2297.
- (37) Groner, M.; George, S. *Interlayer Dielectrics for Semiconductor Technologies* 2003, 1, 327.
- (38) Guicheteau, J. A.; Farrell, M. E.; Christesen, S. D.; Fountain, A. W.; Pellegrino, P. M.; Emmons, E. D.; Tripathi, A.; Wilcox, P.; Emge, D. *Applied Spectroscopy* 2013, 67, 396.
- (39) Gunnarsson, L.; Bjerneld, E. J.; Xu, H.; Petronis, S.; Kasemo, B.; Käll, M. *Applied Physics Letters* 2001, 78, 802.
- (40) Hackley, J. C.; Gougousi, T.; Demaree, J. D. *Journal of Applied Physics* 2007, 102, 034101.
- (41) Hankus, M. E.; Li, H.; Gibson, G. J.; Cullum, B. M. *Analytical Chemistry* 2006, 78, 7535.
- (42) Hao, E.; Schatz, G. C. *The Journal of Chemical Physics* 2004, 120, 357.
- (43) Harper, M. M.; McKeating, K. S.; Faulds, K. *Physical Chemistry Chemical Physics* 2013, 15, 5312.
- (44) Harper, M. M.; McKeating, K. S.; Faulds, K. *Physical Chemistry Chemical Physics* 2013, 15, 5312.
- (45) Haynes, C. L.; Van Duyne, R. P. *The Journal of Physical Chemistry B* 2001, 105, 5599.
- (46) Hölzl, J.; Schulte, F. K. In *Solid Surface Physics*; Hölzl, J., Schulte, F. K., Wagner, H., Eds.; Springer Berlin Heidelberg: Berlin, Heidelberg, 1979, p 1.
- (47) Hu, M.; Ou, F. S.; Wu, W.; Naumov, I.; Li, X.; Bratkovsky, A. M.; Williams, R. S.; Li, Z. *Journal of the American Chemical Society* 2010, 132, 12820.
- (48) Hulteen, J. C.; Treichel, D. A.; Smith, M. T.; Duval, M. L.; Jensen, T. R.; Van Duyne, R. P. *The Journal of Physical Chemistry B* 1999, 103, 3854.
- (49) Ibrahim, A.; Oldham, P. B.; Stokes, D. L.; Vo-Dinh, T. *Journal of Raman Spectroscopy* 1996, 27, 887.
- (50) Ichinose, I.; Senzu, H.; Kunitake, T. *Chemistry of Materials* 1997, 9, 1296.
- (51) Im, H.; Bantz, K. C.; Lee, S. H.; Johnson, T. W.; Haynes, C. L.; Oh, S.-H. *Advanced Materials* 2013, 25, 2678.
- (52) Ingle, J. D.; Crouch, S. R. *Spectrochemical Analysis*; Prentice Hall, 1988.
- (53) Jackson, J. B.; Halas, N. J. *Proceedings of the National Academy of Sciences* 2004,

101, 17930.

(54) Jamieson, L. E.; Jaworska, A.; Jiang, J.; Baranska, M.; Harrison, D. J.; Campbell, C. *J. Analyst* 2015, 140, 2330.

(55) Jeanmaire, D. L.; Van Duyne, R. P. *Journal of Electroanalytical Chemistry and Interfacial Electrochemistry* 1977, 84, 1.

(56) Jha, S. K.; Ahmed, Z.; Agio, M.; Ekinici, Y.; Löffler, J. F. *Journal of the American Chemical Society* 2012, 134, 1966.

(57) Kassu, A.; Robinson, P.; Sharma, A.; Ruffin, P. B.; Brantley, C.; Edwards, E. *Proc. SPIE* 2010, 7764, 77640Q/1.

(58) Kelly, K. L.; Coronado, E.; Zhao, L. L.; Schatz, G. C. *The Journal of Physical Chemistry B* 2003, 107, 668.

(59) Houry, C. G.; Vo-Dinh, T. *The Journal of Physical Chemistry C* 2008, 112, 18849.

(60) Kim, N. H.; Lee, S. J.; Moskovits, M. *Nano Letters* 2010, 10, 4181.

(61) Kim, Y.; Johnson, R. C.; Hupp, J. T. *Nano Letters* 2001, 1, 165.

(62) Kneipp, K.; Haka, A. S.; Kneipp, H.; Badizadegan, K.; Yoshizawa, N.; Boone, C.; Shafer-Peltier, K. E.; Motz, J. T.; Dasari, R. R.; Feld, M. S. *Applied Spectroscopy* 2002, 56, 150.

(63) Kneipp, K.; Kneipp, H. *Applied Spectroscopy* 2006, 60, 322A.

(64) Kneipp, K.; Kneipp, H.; Manoharan, R.; Hanlon, E. B.; Itzkan, I.; Dasari, R. R.; Feld, M. S. *Applied Spectroscopy* 1998, 52, 1493.

(65) Kneipp, K.; Moskovits, M.; Kneipp, H. *Surface-Enhanced Raman Scattering: Physics and Applications*; Springer Berlin Heidelberg, 2006.

(66) Kneipp, K.; Wang, Y.; Kneipp, H.; Perelman, L. T.; Itzkan, I.; Dasari, R. R.; Feld, M. S. *Physical Review Letters* 1997, 78, 1667.

(67) Knight, M. W.; King, N. S.; Liu, L.; Everitt, H. O.; Nordlander, P.; Halas, N. J. *ACS Nano* 2014, 8, 834.

(68) Lal, S.; Grady, N. K.; Goodrich, G. P.; Halas, N. J. *Nano Letters* 2006, 6, 2338.

(69) Le Ru, E. C.; Blackie, E.; Meyer, M.; Etchegoin, P. G. *The Journal of Physical Chemistry C* 2007, 111, 13794.

(70) Le Ru, E. C.; Etchegoin, P. G. In *Principles of Surface-Enhanced Raman Spectroscopy*; Ru, E. C. L., Etchegoin, P. G., Eds.; Elsevier: Amsterdam, 2009, p 121.

(71) Le Ru, E. C.; Etchegoin, P. G. In *Principles of Surface-Enhanced Raman Spectroscopy*; Ru, E. C. L., Etchegoin, P. G., Eds.; Elsevier: Amsterdam, 2009, p 185.

(72) Lee, C. H.; Hankus, M. E.; Tian, L.; Pellegrino, P. M.; Singamaneni, S. *Analytical Chemistry* 2011, 83, 8953.

(73) Leverette, C. L.; Shubert, V. A.; Wade, T. L.; Varazo, K.; Dluhy, R. A. *The Journal of Physical Chemistry B* 2002, 106, 8747.

(74) Li, H.; Baum, C. E.; Sun, J.; Cullum, B. M. *Proc. SPIE* 2006, 6218, 6218041.

(75) Li, H.; Baum, C. E.; Sun, J.; Cullum, B. M. *Applied Spectroscopy* 2006, 60, 1377.

(76) Li, H.; Cullum, B. M. *Applied Spectroscopy* 2005, 59, 410.

(77) Li, H.; Patel, P. H.; Cullum, B. M. *Proc. SPIE* 2004, 5588, 558887.

(78) Li, J. F.; Huang, Y. F.; Ding, Y.; Yang, Z. L.; Li, S. B.; Zhou, X. S.; Fan, F. R.; Zhang, W.; Zhou, Z. Y.; WuDe, Y.; Ren, B.; Wang, Z. L.; Tian, Z. Q. *Nature* 2010, 464, 392.

(79) Li, X.; Hu, H.; Li, D.; Shen, Z.; Xiong, Q.; Li, S.; Fan, H. J. *ACS Applied Materials & Interfaces* 2012, 4, 2180.

(80) Lin, X.-D.; Li, J.-F.; Huang, Y.-F.; Tian, X.-D.; Uzayisenga, V.; Li, S.-B.; Ren, B.;

- Tian, Z.-Q. *Journal of Electroanalytical Chemistry* 2013, 688, 5.
- (81) Liu, Y.; Ashton, J. R.; Moding, E. J.; Yuan, H.; Register, J. K.; Fales, A. M.; Choi, J.; Whitley, M. J.; Zhao, X.; Qi, Y.; Ma, Y.; Vaidyanathan, G.; Zalutsky, M. R.; Kirsch, D. G.; Badea, C. T.; Vo-Dinh, T. *Theranostics* 2015, 5, 946.
- (82) Liz-Marzán, L. M.; Giersig, M.; Mulvaney, P. *Langmuir* 1996, 12, 4329.
- (83) Long, D. A. In *The Raman Effect*; John Wiley & Sons, Ltd: 2002, p 49.
- (84) Long, D. A. In *The Raman Effect*; John Wiley & Sons, Ltd: 2002, p 31.
- (85) Lu, Y.; Liu, G. L.; Kim, J.; Mejia, Y. X.; Lee, L. P. *Nano Letters* 2005, 5, 119.
- (86) Lyon, L. A.; Keating, C. D.; Fox, A. P.; Baker, B. E.; He, L.; Nicewarner, S. R.; Mulvaney, S. P.; Natan, M. J. *Analytical Chemistry* 1998, 70, 341.
- (87) Maier, S. A. *Plasmonics: Fundamentals and Applications*; Springer US: New York USA, 2007.
- (88) Marks, H. L.; Pishko, M. V.; Jackson, G. W.; Coté, G. L. *Analytical Chemistry* 2014, 86, 11614.
- (89) Masango, S. S.; Hackler, R. A.; Henry, A.-I.; McAnally, M. O.; Schatz, G. C.; Stair, P. C.; Van Duyne, R. P. *The Journal of Physical Chemistry C* 2016, 120, 3822.
- (90) McFarland, A. D.; Young, M. A.; Dieringer, J. A.; Van Duyne, R. P. *The Journal of Physical Chemistry B* 2005, 109, 11279.
- (91) McMahan, J. M.; Schatz, G. C.; Gray, S. K. *Physical Chemistry Chemical Physics* 2013, 15, 5415.
- (92) McNay, G.; Docherty, F. T.; Graham, D.; Smith, W. E.; Jordan, P.; Padgett, M.; Leach, J.; Sinclair, G.; Monaghan, P. B.; Cooper, J. M. *Angewandte Chemie International Edition* 2004, 43, 2512.
- (93) McNay, G.; Eustace, D.; Smith, W. E.; Faulds, K.; Graham, D. *Applied Spectroscopy* 2011, 65, 825.
- (94) Michota, A.; Bukowska, J. *Journal of Raman Spectroscopy* 2003, 34, 21.
- (95) Moskovits, M. *The Journal of Chemical Physics* 1978, 69, 4159.
- (96) Moskovits, M. *Reviews of Modern Physics* 1985, 57, 783.
- (97) Moskovits, M. *Journal of Raman Spectroscopy* 2005, 36, 485.
- (98) Moskovits, M. *Notes and Records of the Royal Society* 2012, 66, 195.
- (99) Moskovits, M. *Physical Chemistry Chemical Physics* 2013, 15, 5301.
- (100) Mubeen, S.; Hernandez-Sosa, G.; Moses, D.; Lee, J.; Moskovits, M. *Nano Letters* 2011, 11, 5548.
- (101) Mubeen, S.; Zhang, S.; Kim, N.; Lee, S.; Krämer, S.; Xu, H.; Moskovits, M. *Nano Letters* 2012, 12, 2088.
- (102) Muehlethaler, C.; Leona, M.; Lombardi, J. R. *Analytical Chemistry* 2016, 88, 152.
- (103) Mulvaney, S. P.; Keating, C. D. *Analytical Chemistry* 2000, 72, 145.
- (104) Nanorods. nanocomposix.com (accessed 6/2/2016)
- (105) Ngo, H. T.; Wang, H.-N.; Fales, A. M.; Vo-Dinh, T. *Analytical Chemistry* 2013, 85, 6378.
- (106) Nie, S.; Emory, S. R. *Science* 1997, 275, 1102.
- (107) Oldenburg, S. J.; Averitt, R. D.; Westcott, S. L.; Halas, N. J. *Chemical Physics Letters* 1998, 288, 243.
- (108) Oldenburg, S. J.; Westcott, S. L.; Averitt, R. D.; Halas, N. J. *The Journal of Chemical Physics* 1999, 111, 4729.
- (109) Orendorff, C. J.; Gearheart, L.; Jana, N. R.; Murphy, C. J. *Physical Chemistry*

- Chemical Physics 2006, 8, 165.
- (110) Orendorff, C. J.; Gole, A.; Sau, T. K.; Murphy, C. J. *Analytical Chemistry* 2005, 77, 3261.
- (111) Osberg, K. D.; Rycenga, M.; Harris, N.; Schmucker, A. L.; Langille, M. R.; Schatz, G. C.; Mirkin, C. A. *Nano Letters* 2012, 12, 3828.
- (112) Penn, M. A.; Drake, D. M.; Driskell, J. D. *Analytical Chemistry* 2013, 85, 8609.
- (113) Pham, T.; Jackson, J. B.; Halas, N. J.; Lee, T. R. *Langmuir* 2002, 18, 4915.
- (114) Pilo-Pais, M.; Watson, A.; Demers, S.; LaBean, T. H.; Finkelstein, G. *Nano Letters* 2014, 14, 2099.
- (115) Pozzi, F.; Leona, M. *Journal of Raman Spectroscopy* 2016, 47, 67.
- (116) Prodan, E.; Radloff, C.; Halas, N. J.; Nordlander, P. *Science* 2003, 302, 419.
- (117) Qi, D.; Yan, X.; Wang, L.; Zhang, J. *Chemical Communications* 2015, 51, 8813.
- (118) Qi, J.; Li, Y.; Yang, M.; Wu, Q.; Chen, Z.; Peng, J.; Liu, Y.; Wang, W.; Yu, X.; Sun, Q.; Xu, J. *Nanoscale Res. Lett.* 2013, 8, 495/1.
- (119) Qin, L.; Zou, S.; Xue, C.; Atkinson, A.; Schatz, G. C.; Mirkin, C. A. *Proceedings of the National Academy of Sciences* 2006, 103, 13300.
- (120) Raman, C. V.; Krishnan, K. S. *Indian J. Phys.* 1928, 2, 399.
- (121) Rentería-Tapia, V. M.; Valverde-Aguilar, G.; García-Macedo, J. A. 2007, 6641, 66411W.
- (122) Robertson, J. *Journal of Vacuum Science & Technology B* 2000, 18, 1785.
- (123) Robertson, J. *The European Physical Journal - Applied Physics* 2004, 28, 265.
- (124) Roca, M.; Haes, A. J. *Journal of the American Chemical Society* 2008, 130, 14273.
- (125) Rodríguez-Lorenzo, L.; Fabris, L.; Alvarez-Puebla, R. A. *Analytica Chimica Acta* 2012, 745, 10.
- (126) Ruedas-Rama, M. J.; Walters, J. D.; Orte, A.; Hall, E. A. H. *Analytica Chimica Acta* 2012, 751, 1.
- (127) Sardar, R.; Heap, T. B.; Shumaker-Parry, J. S. *Journal of the American Chemical Society* 2007, 129, 5356.
- (128) Sardar, R.; Shumaker-Parry, J. S. *Nano Letters* 2008, 8, 731.
- (129) Schatz, G. C. *Accounts of Chemical Research* 1984, 17, 370.
- (130) Schultz, Z. D.; Wang, H.; Kwasnieski, D. T.; Marr, J. M. *Proc. SPIE* 2015, 9554, 9554091.
- (131) Sharma, B.; Fernanda Cardinal, M.; Kleinman, S. L.; Greeneltch, N. G.; Frontiera, R. R.; Blaber, M. G.; Schatz, G. C.; Van Duyne, R. P. *MRS Bulletin* 2013, 38, 615.
- (132) Sharma, B.; Frontiera, R. R.; Henry, A.-I.; Ringe, E.; Van Duyne, R. P. *Materials Today* 2012, 15, 16.
- (133) Sharma, B.; Ma, K.; Glucksberg, M. R.; Van Duyne, R. P. *Journal of the American Chemical Society* 2013, 135, 17290.
- (134) Singh, R.; Ulrich, R. K. *Electrochem. Soc. Interface* 1999, 8, 26.
- (135) Sirimuthu, N. M. S.; Syme, C. D.; Cooper, J. M. *Proc. SPIE* 2012, 8234, 82340F.
- (136) Smitha, S. L.; Gopchandran, K. G.; Ravindran, T. R.; Prasad, V. S. *Nanotechnology* 2011, 22, 265705.
- (137) Stender, A. S.; Marchuk, K.; Liu, C.; Sander, S.; Meyer, M. W.; Smith, E. A.; Neupane, B.; Wang, G.; Li, J.; Cheng, J.-X.; Huang, B.; Fang, N. *Chemical Reviews* 2013, 113, 2469.
- (138) Stetciura, I. Y.; Yashchenok, A.; Masic, A.; Lyubin, E. V.; Inozemtseva, O. A.;

- Drozdova, M. G.; Markvichova, E. A.; Khlebtsov, B. N.; Fedyanin, A. A.; Sukhorukov, G. B.; Gorin, D. A.; Volodkin, D. *Analyst* 2015, 140, 4981.
- (139) Stokes, R. J.; Macaskill, A.; Dougan, J. A.; Hargreaves, P. G.; Stanford, H. M.; Smith, W. E.; Faulds, K.; Graham, D. *Chem. Commun. (Cambridge, U. K.)* 2007, 2811.
- (140) Strobbia, P.; Henegar, A.; Gougousi, T.; Cullum, B. M. *Proc. SPIE* 2015, 9487, 94870P.
- (141) Strobbia, P.; Henegar, A. J.; Gougousi, T.; Cullum, B. M. *Applied Spectroscopy* 2016, (in press).
- (142) Strobbia, P.; Languirand, E.; Cullum, B. M. *Optical Engineering* 2015, 54, 100902.
- (143) Sun, J.; Hankus, M. E.; Cullum, B. M. *Proc. SPIE* 2009, 7313, 73130K0.
- (144) Svedberg, F.; Li, Z.; Xu, H.; Käll, M. *Nano Letters* 2006, 6, 2639.
- (145) Talley, C. E.; Jackson, J. B.; Oubre, C.; Grady, N. K.; Hollars, C. W.; Lane, S. M.; Huser, T. R.; Nordlander, P.; Halas, N. J. *Nano Letters* 2005, 5, 1569.
- (146) Tanabe, K. *The Journal of Physical Chemistry C* 2008, 112, 15721.
- (147) Tjeng, L. H.; Meinders, M. B. J.; van Elp, J.; Ghijsen, J.; Sawatzky, G. A.; Johnson, R. L. *Physical Review B* 1990, 41, 3190.
- (148) Tong, L.; Righini, M.; Gonzalez, M. U.; Quidant, R.; Kall, M. *Lab on a Chip* 2009, 9, 193.
- (149) Tripathi, A.; Emmons, E. D.; Fountain, A. W.; Guicheteau, J. A.; Moskovits, M.; Christesen, S. D. *ACS Nano* 2015, 9, 584.
- (150) Van Duyne, R. P.; Hulteen, J. C.; Treichel, D. A. *Journal of Chemical Physics* 1993, 99, 2101.
- (151) Vitol, E. A.; Orynbayeva, Z.; Friedman, G.; Gogotsi, Y. *Journal of Raman Spectroscopy* 2012, 43, 817.
- (152) Vo-Dinh, T.; Hiromoto, M. Y. K.; Begun, G. M.; Moody, R. L. *Analytical Chemistry* 1984, 56, 1667.
- (153) Wang, J.-F.; Li, H.-J.; Zhou, Z.-Y.; Li, X.-Y.; Liu, J.; Yang, H.-Y. *Chin. Phys. B* 2010, 19, 117310/1.
- (154) Wilson, C. A.; Grubbs, R. K.; George, S. M. *Chemistry of Materials* 2005, 17, 5625.
- (155) Wu, H.-Y.; Choi, C. J.; Cunningham, B. T. *Small* 2012, 8, 2878.
- (156) Xu, H.; Aizpurua, J.; Käll, M.; Apell, P. *Physical Review E* 2000, 62, 4318.
- (157) Yuan, H.; Fales, A. M.; Khoury, C. G.; Liu, J.; Vo-Dinh, T. *Journal of Raman Spectroscopy* 2013, 44, 234.
- (158) Yuan, H.; Register, J.; Wang, H.-N.; Fales, A.; Liu, Y.; Vo-Dinh, T. *Analytical and Bioanalytical Chemistry* 2013, 405, 6165.
- (159) Yuen, J. M.; Shah, N. C.; Walsh, J. T.; Glucksberg, M. R.; Van Duyne, R. P. *Analytical Chemistry* 2010, 82, 8382.
- (160) Zhang, X.; Zhao, J.; Whitney, A. V.; Elam, J. W.; Van Duyne, R. P. *Journal of the American Chemical Society* 2006, 128, 10304.
- (161) Zhao, Y.; Sun, L.; Xi, M.; Feng, Q.; Jiang, C.; Fong, H. *ACS Applied Materials & Interfaces* 2014, 6, 5759.

